

Inaugural dissertation

for

obtaining the doctoral degree

of the

Combined Faculty of Mathematics, Engineering and Natural Sciences

of the

Ruprecht - Karls - University

Heidelberg

presented by

M.Sc. Bettina Weigel

born in: Schweinfurt, Germany

oral examination: 10.05.2023

**The role of MYT1L in the aetiology of
neurodevelopmental disorders**

Referees:

Prof. Dr. Ana Martin-Villalba

Dr. Michael Milsom

Abstract

Neurodevelopmental disorders (NDDs) represent a huge global health burden. However, the aetiology of most psychiatric disorders remains enigmatic, making it very difficult to find adequate treatment options. While many transcription factors are associated with mental disorders, MYT1L stands out as one of very few life-long-expressed and neuron-specific transcriptional regulators. *MYT1L* mutations are closely linked to various neurodevelopmental disorders, like autism spectrum disorder and schizophrenia.

In this work, I used embryonic stem cell-derived human neurons and mice to study how MYT1L regulates brain development, whether mutations are sufficient to cause mental disease and, if so, whether there is potential for therapeutic intervention.

I found that MYT1L deficiency caused upregulation of its target genes, including members of the WNT and NOTCH signalling pathways. This resulted in neurodevelopmental delays that could be partially rescued by chemical pathway inhibition. MYT1L-deficient mice also presented with abnormal brain morphology and behavioural deficits. I found that MYT1L loss caused upregulation of non-neuronal genes, including the main cardiac sodium channel *SCN5A*, which might explain the unexpected neuronal network hyperactivity observed in mouse and human neurons. Supporting this hypothesis, I was able to normalise electrophysiological hyperactivity by *Myt1l* overexpression and *Scn5a* knock-down. Excitingly, the FDA-approved sodium channel blocker lamotrigine rescued electrophysiological abnormalities *in vitro* and behavioural deficits *in vivo*.

The findings in this study show an important role of MYT1L as a transcriptional repressor not only during development but also after neurogenesis. Failure to silence non-neuronal gene expression in neurons might represent a novel mechanism that, at least in part, can contribute to NDD aetiology. The rescue of *MYT1L* deficiency-associated phenotypes in post-mitotic cells and adult mice opens up the possibility of therapeutic intervention for patients with MYT1L syndrome, including later in life.

Zusammenfassung

Entwicklungsstörungen des Nervensystems stellen eine große weltweite Belastung dar. Dennoch bleibt die Ursache der meisten psychischen Erkrankungen bisher rätselhaft. Viele Transkriptionsfaktoren werden mit mentalen Störungen in Verbindung gebracht, doch MYT1L ist speziell, da es einer von wenigen Transkriptionsfaktoren ist, die lebenslang und spezifisch in Neuronen exprimiert sind. MYT1L Mutationen stehen im Zusammenhang mit verschiedensten Entwicklungsstörungen des Nervensystems, wie der Autismus-Spektrum-Störung und Schizophrenie.

In diesem Projekt habe ich mit, aus embryonalen Stammzellen erzeugten, menschlichen Neuronen und Mäusen gearbeitet, um zu untersuchen wie MYT1L die Gehirnentwicklung reguliert, ob Mutationen ausreichend sind, um mentale Krankheiten zu verursachen und falls ja, ob es eine Möglichkeit gibt therapeutisch einzugreifen.

Ich habe festgestellt, dass ein Mangel an MYT1L zu einer Hochregulation von Zielgenen, einschließlich Mitgliedern der WNT und NOTCH Signalwege, geführt hat. Dies hatte eine Verzögerung der Entwicklung des Nervensystems zur Folge, was teilweise durch chemische Hemmung der Signalwege normalisiert werden konnte. MYT1L defiziente Mäuse zeigten eine veränderte Morphologie des Gehirns und Verhaltensdefizite. Ich habe außerdem entdeckt, dass der Verlust von MYT1L zu einer Hochregulation nicht neuronaler Gene, einschließlich des primären Natriumkanals des Herzens *SCN5A*, geführt hat. Dies wäre eine mögliche Ursache für die unerwartete Überfunktion des neuronalen Netzwerks, die ich in murinen und menschlichen Neuronen beobachtet habe. Diese Annahme wird dadurch bekräftigt, dass es mir gelungen ist die elektrophysiologische Überfunktion durch Überexpression von *Myt1l* und knockout von *Scn5a* zu normalisieren. Spannenderweise konnten die elektrophysiologischen Auffälligkeiten *in vitro* und die Verhaltensdefizite *in vivo* mit dem, von der FDA zugelassenen, Natriumkanalblocker Lamotrigin behandelt werden.

Die Erkenntnisse aus diesem Projekt zeigen, dass MYT1L eine wichtige repressive Funktion während und nach Beendigung der Entwicklung des Nervensystems hat. Eine Störung darin, die Expression nicht neuronaler Gene in Neuronen zu unterdrücken, könnte einen neuen Mechanismus darstellen, der zumindest teilweise zu der Entstehung von Entwicklungsstörungen des Nervensystems beitragen kann. Die Normalisierung von, durch Mangel an MYT1L verursachten, Phänotypen in postmitotischen Zellen und erwachsenen Mäusen eröffnet die Möglichkeit, dass Patienten mit MYT1L Syndrom auch später im Leben von therapeutischen Eingriffen profitieren können.

CONTENTS

Abstract	iii
Zusammenfassung	iv
Abbreviations	ix
1 Introduction	1
1.1 Cellular differentiation	1
1.2 Transcriptional regulation of cell identity	2
1.3 Neurodevelopment	3
1.4 Neurodevelopmental disorders (NDDs)	7
1.5 The transcription factor MYT1L	9
1.6 Aims of the study	11
2 Results	12
2.1 Characterisation of MYT1L-deficient mice	12
2.1.1 MYT1L is essential for survival	12
2.1.2 Impaired brain development in <i>Myt1l</i> -deficient mice	15
2.1.3 MYT1L depletion causes NDD-associated gene deregulation	18
2.1.4 Transcriptional enrichment of several non-neuronal signatures in <i>Myt1l</i> -deficient mice	19
2.1.5 MYT1L predominantly acts as repressor in mice	21
2.1.6 Hyperactivity and male-specific social deficits upon MYT1L depletion in mice	23
2.2 Effect of MYT1L depletion in human neurons	25
2.2.1 MYT1L predominantly acts as repressor in human neurons	25
2.2.2 Enrichment of non-neuronal terms in <i>MYT1L</i> -deficient neurons	27
2.2.3 Delayed neurogenesis in MYT1L-depleted human induced neurons	28

2.3	Functional assessment of MYT1L-depleted neurons	31
2.3.1	<i>MYT1L</i> -deficient human neurons show network hyperactivity	31
2.3.2	Network hyperactivity upon MYT1L depletion is evolutionarily conserved	33
2.3.3	Synaptic hyperactivity in <i>Myt1l</i> -deficient cultures and brain slices	35
2.4	Towards therapeutic intervention for MYT1L syndrome	38
2.4.1	Post-mitotic MYT1L overexpression normalises spiking frequency of MYT1L-depleted neurons	38
2.4.2	Knockdown of the main cardiac sodium channel <i>SCN5A</i> reduces spiking frequency	39
2.4.3	Pharmacological intervention restores neuronal network activity and behaviour phenotypes	42
3	Discussion	45
4	Conclusion	53
5	Materials and Methods	56
5.1	Materials	56
5.2	Methods	69
5.2.1	Targeting and maintenance of human embryonic stem cells	69
5.2.2	Generation of knockout mice	70
5.2.3	Genotyping	71
5.2.4	Immunoprecipitation	71
5.2.5	LC-MS/MS analysis	71
5.2.6	Cloning	72
5.2.7	Virus production	74
5.2.8	Primary tissue dissection and cell culture	74
5.2.9	Generation of human neurons	74
5.2.10	Immunocytochemistry	75
5.2.11	Immunohistochemistry	75
5.2.12	Brain morphology analysis	76
5.2.13	EdU labelling and embryonic sections	76
5.2.14	Behaviour experiments	76
5.2.15	Transcriptome analysis using RNA-sequencing	78
5.2.16	Chromatin binding using CUT&RUN	80
5.2.17	Brain slice preparation and electrophysiology	81

5.2.18 Multi-electrode array (MEA)	82
5.2.19 Quantitative real time polymerase chain reaction (qRT-PCR)	82
5.2.20 SDS-PAGE and Western blot	83
5.2.21 Statistical analysis	83
References	85
Supplementary figures	106
List of figures	108
Declaration	111
Contributions	112
Acknowledgements	113

ABBREVIATIONS

aa	Amino acid
aRGCs	Apical radial glial cells
ASCL1	Achaete-scute homolog 1
Ara-C	Cytosine β -D-arabinofuranoside
bHLH	Basic helix-loop-helix
BDNF	Brain-derived neurotrophic factor
BSA	Bovine serum albumin
CCS	Cosmic calf serum
CNS	Central nervous system
DAPI	4',6-diamidino-2-phenylindole
DAPT	N-[N-(3,5-difluorophenacetyl)-l-alanyl]-S-phenylglycine t-butyl ester
DMEM	Dulbecco's Modified Eagle's medium
DIV	Day <i>in vitro</i>
DTT	Dithiothreitol
EdU	5-Ethynyl-2'-Desoxyuridin
ESC	Embryonic stem cell
EPM	Elevated plus maze
EPSCs	Excitatory postsynaptic current
FBS	Fetal Bovine Serum

FGF	Fibroblast growth factor
GO	Gene ontology
GSEA	Gene Set Enrichment Analysis
HBSS	Hanks' Buffered Saline Solution
HDAC	Histone deacetylase
IHC	Immunohistochemistry
iNs	Induced neuron
IPSC	Inhibitory postsynaptic current
IPA	Ingenuity pathway analysis
IPC	Intermediate progenitor cell
IZ	Intermediate zone
MEA	Multi-electrode array
MEM	Minimum Essential Medium
MYT1L	Myelin Transcription Factor 1-Like
Myt/NZF	Myelin transcription factor/Neural zinc finger
NDD	Neurodevelopmental disorder
NEAA	Non-Essential Amino Acids
NECs	Neuroepithelial cells
NEUROD1	Neuronal Differentiation 1
NICD	NOTCH intracellular domain
NLS	Nuclear localisation signal
NT3	Neurotrophin-3
OF	Open field
PBS	Phosphate Buffered Saline (PBS)
PEG	Polyethylenglycol

Pen/Strep	Penicillin/ Streptomycin
PFA	Paraformaldehyd
PEI	Polyethyleneimine
PO	Poly-L-ornithine
qRT-PCR	Quantitative real time polymerase chain reaction
RNA-Seq	RNA-Sequencing
REST	Repressor Element 1 Silencing Transcription factor
RT	Room temperature
SCT	Social chamber test
SDS	Sodium dodecyl sulfate
SDS-PAGE	SDS Polyacrylamide Gel Electrophoresis
SHH	Sonic Hedgehog
SVZ	Subventricular zone
TF	Transcription factor
USV	Ultrasonic vocalisation
VZ	Ventricular zone
WT	Wild type
XAV939	Tetrahydro-2-[4-(trifluoromethyl)phenyl]-4H-thiopyrano[4,3-d]pyrimidin
ZF	Zinc finger

1 INTRODUCTION

1.1 Cellular differentiation

The human body consists of hundreds of different cell types [1], which all develop from a single cell: the totipotent zygote. During embryonic development, the zygote undergoes rapid cell division, called cleavage, to form the blastocyst. Within the blastocyst, two main tissue layers form: an inner cell mass and an outer trophectoderm. The inner cell mass further differentiates into the epiblast and primitive endoderm. The trophectoderm and primitive endoderm form extraembryonic tissues that support embryonic development. The epiblast is pluripotent, which means that each cell has the potential to differentiate into any cell type in the human body [2, 3]. Differentiation starts in the embryo with gastrulation, which is the segregation of epiblast cells into the three germ layers: endoderm, mesoderm, and ectoderm. The ectoderm gives rise to the nervous system, epidermis, and neural crest-derived tissues. The endoderm forms the gastrointestinal, respiratory and urinary systems, and many endocrine glands. The mesoderm forms the notochord, axial skeleton, cartilage, connective tissue, trunk muscles, kidneys, and blood [4, 5]. The differentiation of pluripotent cells to more specialised cell types is associated with major transcriptional changes. Underlying these changes in gene expression are changes in the structure and function of chromatin, called epigenetic reprogramming [6].

In 1957, Conrad Waddington used the metaphor of an epigenetic landscape to describe cellular development. Undifferentiated totipotent cells start at the top of a hill and, as they roll downwards, possess a progressively restricted range of developmental outcomes. Depending on the landscape's topography, which represents different epigenetic states, cells end up in different valleys at the bottom of the hill, corresponding to their differentiated states. The unique epigenetic landscape of each cell type determines the gene expression program, which has to be very closely controlled and governs the identity and biological function of each cell [7, 8].

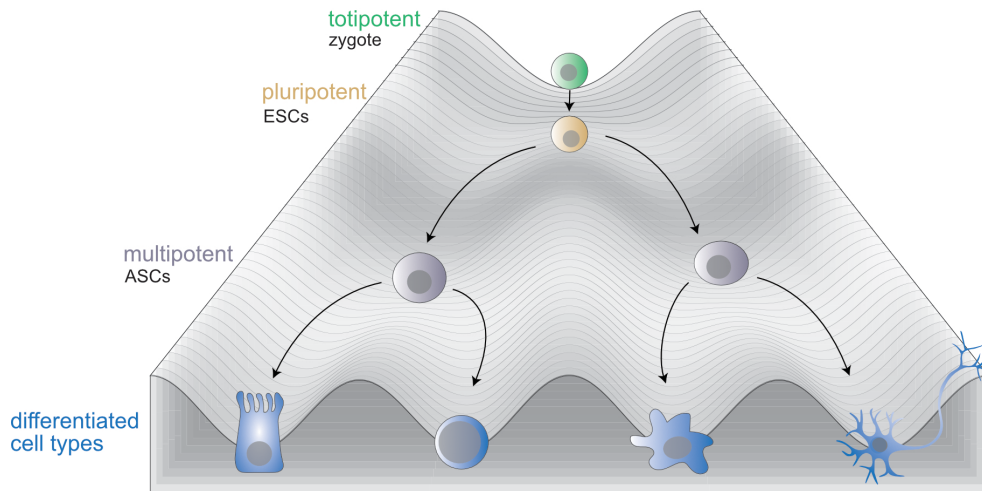


Figure 1.1: Waddington’s epigenetic landscape. Totipotent cells at the top of the hill acquire progressively restricted cell fate potential as they roll down. The different valleys at the bottom of the hill correspond to various differentiated cell states. ESCs: embryonic stem cells, ASCs: adult stem cells.

This developmental process occurs within each cell and is largely orchestrated by the interplay of transcription factors [9].

1.2 Transcriptional regulation of cell identity

Transcription factors (TFs) are proteins that regulate gene expression by binding to a specific DNA sequence, located in enhancers or promoter regions. This binding can either promote (activators) or repress (repressors) gene expression. The gene expression program ultimately defines phenotypic and functional characteristics of a cell, and is very precisely controlled via an interplay between activators and repressors [10–14].

The commonly-held notion in the field is that a small number of TFs with lineage-restricted expression patterns are sufficient to establish gene expression programs that define the identity of a cell [15]. TFs that are required to determine cell identity during early developmental pathways are termed selectors [16]. These TFs often have the ability to bind to inaccessible nucleosomal DNA, open it, and induce gene expression, which gives them the name “pioneer” TFs [17]. For example, the proneuronal TFs *Achaete-scute homolog 1* (ASCL1) and *Neuronal Differentiation 1* (NEUROD1) have each been shown to be sufficient to promote neuronal differentiation [18–22]. Apart from activators, which drive the establishment of different cell identities, transcriptional repression is also essential to shut off unwanted genes during development [23]. The Repressor Element 1 Silencing Transcription factor (REST), for instance, is expressed in most cells of the body, excluding

neurons, to repress neuronal gene expression [24–26].

The initial assumption by Waddington that cells which have acquired a cell type-specific expression program are terminally differentiated, and therefore in an irreversible cellular state, was refuted by somatic cell nuclear transfer experiments [27, 28] and the discovery that differentiated cells can be forced into pluripotency by expression of only a few TFs [29]. This suggests that cell identity is plastic and can be destabilised, which raises the question of whether a cell type-specific expression program not only needs to be established, but also actively maintained throughout the life of a cell. Based on this, Oliver Hobert expanded the concept of selector genes, and proposed the idea of terminal selector genes. While selectors are important during differentiation of cells, terminal selectors act in differentiated cells to regulate the expression of terminal differentiation genes and thereby actively define and maintain the identity of individual cell types [30].

1.3 Neurodevelopment

Most cells within the nervous system derive from the ectoderm, one of the three germ layers that comprise the developing embryo after gastrulation [31]. After neural tube formation, the rostral portion of the tube divides initially into three, then five brain vesicles that generate different parts of the brain [32] (Figure 1.2). In the dorsal telencephalon, the cerebral cortex (also called the neocortex) differentiates [33, 34]. The cerebral cortex constitutes the largest part of the human brain and plays a central role in higher cognitive abilities.

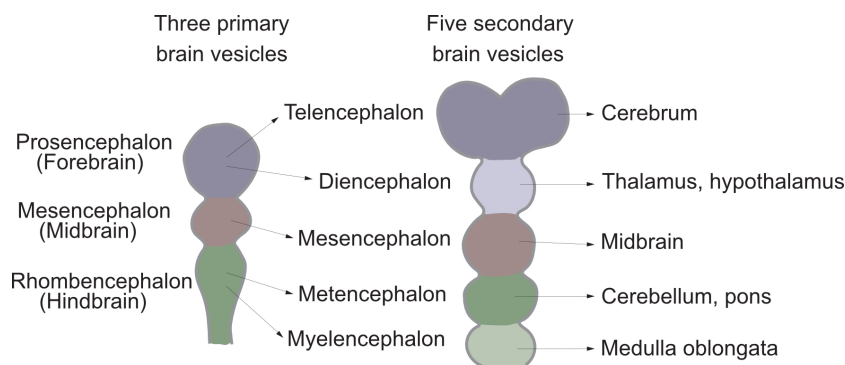


Figure 1.2: A schematic figure of the primary brain vesicles (left) and the secondary brain vesicles (right). Shown are horizontal sections through the neural tube with the rostral part on the top.

Before cortical neurogenesis, the cortex is primarily composed of neuroepithelial cells

(NECs), which are highly polarised along their apical–basal axis and are attached at the ventricular surface and the basal lamina [35–37]. They initially proliferate symmetrically to increase the pool of neural stem cells (NSCs), which results in lateral and radial extension of the neocortex [38]. Mitosis takes place at the ventricular surface after the nucleus migrates through the cytoplasm along the apical–basal axis, a process called interkinetic nuclear migration [39], which plays an essential role in the homeostasis of the neural progenitor pool [40]. At the onset of cortical neurogenesis, NECs switch to asymmetric division to form apical radial glial cells (aRGCs) [41]. These cells continue to display apico–basal polarity and interkinetic nuclear migration, but express astroglial markers [42] and upregulate specific TFs like PAX6 [43, 44]. aRGCs serve as a scaffold for neuronal migration and are able to generate neurons, astrocytes, and oligodendrocytes [45, 46]. During neurogenesis, aRGCs self-renew but primarily divide asymmetrically to produce a new aRGC and either a neuron (direct neurogenesis, which occurs in the ventricular zone (VZ)) or an intermediate progenitor cell (IPC). IPCs are transiently amplifying progenitors characterised by the expression of the transcription factor TBR2 [47] and give rise to neurons (indirect neurogenesis, which occurs in the subventricular zone (SVZ)).

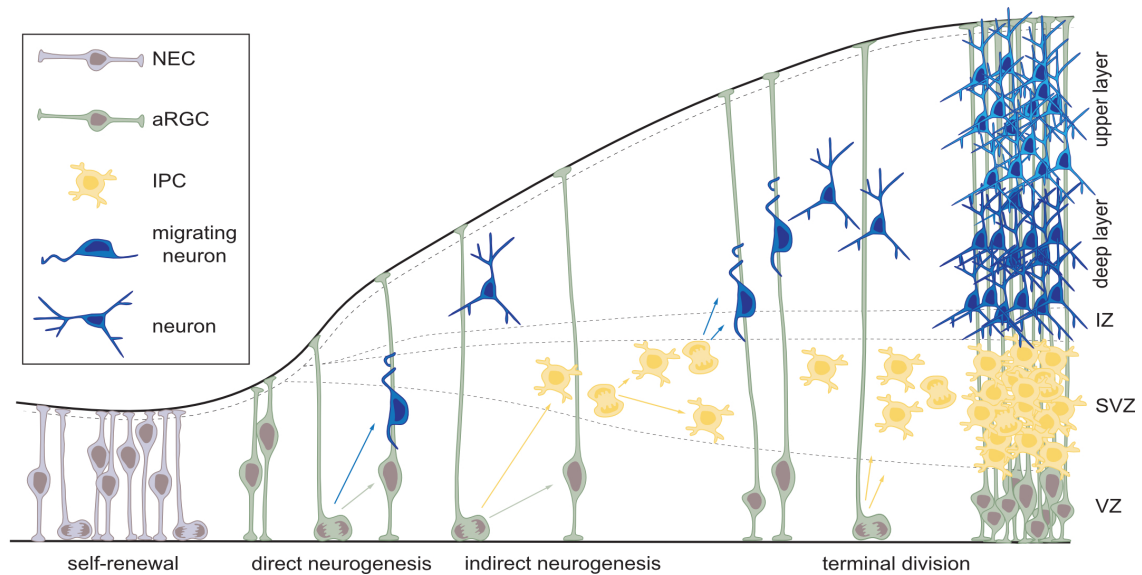


Figure 1.3: Schematic presentation of the steps of cortical neurogenesis in the mouse. Neuroepithelial cells (NECs) undergo interkinetic nuclear migration and symmetric divisions to self-renew, then turn into apical radial glial cells (aRGCs) that give rise to neurons (direct neurogenesis) or to intermediate progenitor cells (IPC, indirect neurogenesis). IPCs populate the sub-ventricular zone (SVZ) and generate cortical layer neurons, which migrate along the basal processes of aRGCs to their destined layer in the cortical plate. At later stages, aRGCs can undergo final symmetric divisions generating two neurons. IZ: intermediate zone, SVZ: subventricular zone, VZ: ventricular zone.

At later stages of cortex development, the aRGC pool becomes depleted by terminal divisions, only producing differentiating progenitors and neurons [48, 49]. Once neurons are born, they migrate along the radial fiber of a radial glial cell (radial migration) to their final destination in the developing cortical plate (CP), which is organised into six layers of neurons [50]. Layers are formed in an inside-out manner, which means that deep cortical layer neurons are produced first, followed by the immediately overlying layer, and so on [51]. This applies primarily to excitatory neurons. Cortical inhibitory interneurons follow a different developmental program, which is not the focus of my thesis but is summarised here [52]. Stem and progenitor cells have a limited proliferation capacity [49, 53], which means that final neuronal output depends on the initial pool of founder progenitors (NECs), the switch from symmetric to neurogenic division, and the duration of neurogenesis.

Onset and progression of neurogenesis is closely regulated by several different factors including TFs (basic helix-loop-helix (bHLH) and homeodomain TFs), epigenetic modifications, post-transcriptional regulation of gene expression, neural progenitor environment, and signalling pathways. Important examples of the latter are NOTCH, fibroblast growth factor (FGF), WNT, and Sonic Hedgehog (SHH) signalling [54].

The NOTCH signalling pathway is crucial for maintenance of neural progenitors. NOTCH signalling is activated by binding of the extracellular domain of the NOTCH ligands DSL (DELTA/SERRATE/LAG-2) on the surface of one cell to the extracellular domain of the NOTCH receptor on an adjacent cell, leading to cleavage and nuclear localisation of the NOTCH intracellular domain (NICD) and subsequent expression of target genes like the bHLH TFs *HES1* and *HES5* [55]. These TFs repress the expression of pro-neuronal genes such as *ASCL1* and *NEUROG1*, resulting in inhibition of neuronal differentiation and thereby maintenance of the neural progenitor pool [56]. NOTCH activity is distributed in gradients along the apicobasal axis of the neuroepithelium. During asymmetric division of aRGCs, unequal distribution of NOTCH pathway components restricts NOTCH activity and self-renewal to the apical daughter cell, while the basal daughter cell differentiates [57]. This process when a cell develops into a specific cell type while inhibiting its neighbours from developing the same way is called lateral inhibition [58]. However, NOTCH signalling sometimes remains active throughout neuronal differentiation, raising the question of how cellular responses to the signalling change during neurogenesis. In this regard, the transcription factor BCL6, which is highly expressed during neurogenesis, has been found to induce epigenetic silencing of *HES5* expression despite NOTCH signalling

by recruitment of the protein deacetylase Sirtuin 1 [59]. Later in development, NOTCH signalling has been reported to promote astrogenesis [60].

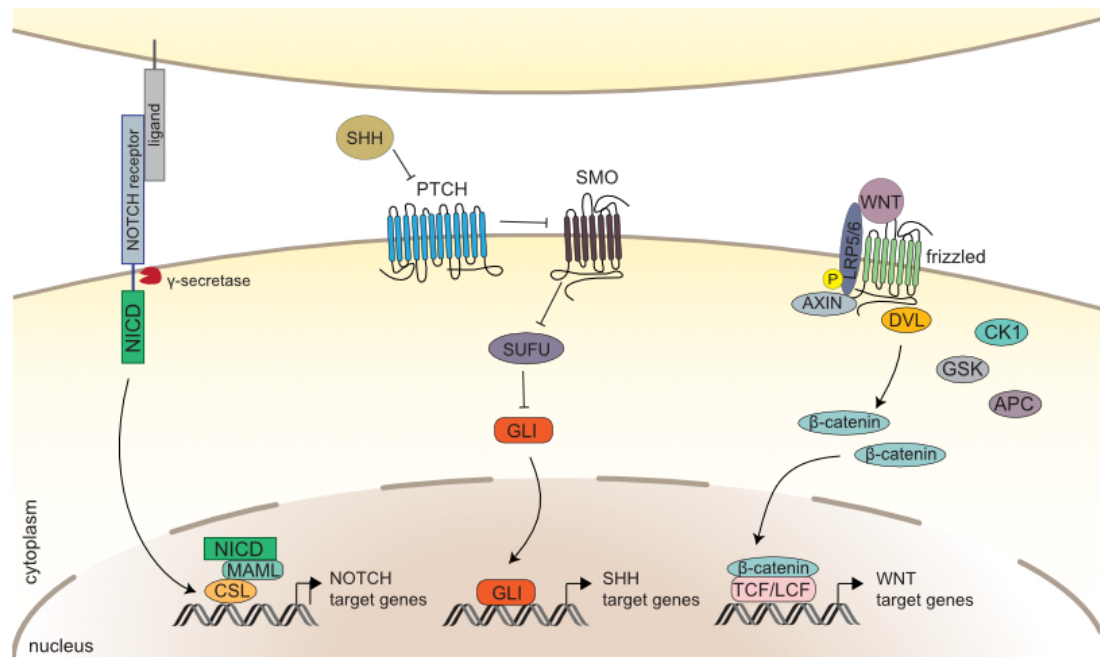


Figure 1.4: Schematic presentation of signalling pathways involved in neurogenesis. NOTCH (left): NOTCH binding promotes proteolytic cleavage by γ -secretase, which releases the NOTCH intracellular domain (NICD) into the nucleus where it cooperates with the DNA-binding protein CSL and its co-activator MAML to promote target gene expression. Sonic hedgehog (SHH, middle): SHH binds to PTCH at the cell membrane. In response to this, PTCH no longer inhibits SMO, which inhibits SUFU, resulting in the activation and translocation of GLI into the nucleus, where it activates target gene expression. WNT (right): WNT signalling through the frizzled receptor and LRP5/6 co-receptor complex induces phosphorylation of LRP5/6 by CK1 and GSK, which allows for the translocation of the AXIN-containing protein complex from the cytosol to the plasma membrane. AXIN binds to phosphorylated LRP5/6. DVL is also recruited to the membrane and binds to frizzled. This complex induces the stabilisation of β -catenin, which translocates into the nucleus, where it mediates target gene expression together with TCF/LCF. Adapted from [61]

A second signalling pathway important for brain development is the WNT pathway. The WNT family of signalling molecules can initiate several signalling cascades through activation of different receptor types and complexes. One of these is the canonical pathway, which leads to the stabilisation and nuclear translocation of β -catenin [62]. Early in neurogenesis, β -catenin promotes proliferative division of neural progenitor cells and delays IPC formation [63, 64], while at later stages, β -catenin-dependent signalling has been shown to promote neuronal differentiation [65–67]. This demonstrates that the functional outcomes of canonical WNT signalling are highly dependent on developmental stage and location.

Another signalling pathway with fundamental roles in central nervous system (CNS) development is the SHH signalling pathway. Activation occurs when SHH binds to its receptor PTCH at the plasma membrane. This binding prevents PTCH inhibition of SMO, which then accumulates at the plasma membrane and initiates activation and translocation of GLI to the nucleus. In the absence of SHH, GLI acts as repressor [68]. SHH signalling has been shown to promote IPC generation and expansion [69–71], while it also plays a role in cortical gliogenesis [72]. Interestingly, SHH activity induces expression of downstream targets of the NOTCH signalling pathway, e.g. *HES1*, emphasising the interplay between different signalling pathways [73]. Such an interplay has also been reported for NOTCH and FGF signalling [74].

Overall, cortical neurogenesis consists of a series of processes, including proliferation and fate transition of progenitors, as well as neuronal migration, specification, and maturation, which all rely on a closely-controlled interplay between signalling molecules and TFs. This complexity renders it sensitive to disruption, which can cause neurodevelopmental deficits.

1.4 Neurodevelopmental disorders (NDDs)

Neurodevelopmental disorders (NDDs) are a group of psychiatric or behavioural conditions caused by the disruption of essential neurodevelopmental processes [75]. NDDs, which include autism spectrum disorder (ASD), intellectual disability (ID), attention deficit hyperactivity disorder (ADHD), epilepsy, and schizophrenia, constitute a huge health burden, affecting more than 3% of children worldwide [76]. The main cause of NDDs are genetic mutations, while environmental factors such as malnutrition, perinatal infections, drug misuse, or pollution may cause epigenetic dysregulation which contributes to the development of such disorders [75]. NDDs have an extreme genetic heterogeneity, and more than one NDD phenotype often occurs in individual patients [77, 78], while severity of clinical symptoms can vary considerably among patients with overlapping mutations [79, 80]. There is evidence that genetic risk factors are shared across key psychiatric disorders [81], suggesting conserved underlying molecular mechanisms.

Tremendous progress in genome and exome sequencing over the past few years has led to the identification of over 400 genes associated with NDDs [82–85], and there is also increasing evidence for the involvement of non-coding regions in disease aetiology [86–88]. However, the biological mechanisms underlying these disorders still remain poorly under-

stood. Previous research has focused on gene alterations linked to neuronal function, such as mutations in ion channels, neurotransmitters, and neurotransmitter receptors, which would alter the function of neuronal circuits and contribute to NDDs [89, 90]. In recent studies, however, it has emerged that gene regulators, including chromatin regulators and TFs, are often mutated and could play a role in the aetiology of NDDs [91]. Indeed, mouse models showed that mutations in chromatin remodelers, such as *Chd8* or TFs, such as *Foxp2*, can induce behavioural phenotypes [92, 93], suggesting a potential causal role in NDDs.

In order to better understand the molecular mechanisms underlying NDDs with the goal of finding adequate treatment options, mutations in several NDD-risk genes have been modelled *in vivo* in animals and *in vitro* in cellular models. These mutations resulted in various phenotypes, including behavioural abnormalities, gene deregulation, and synaptic dysfunction [94–97], and it has become increasingly evident that several risk genes are co-regulated and may converge in regulatory networks associated with NDDs [98–100]. For example, the ASD-risk gene *CHD8* has been shown to directly regulate several other ASD-risk genes [101]. Chromatin-associated genes can influence neuronal activity phenotypes by regulating synaptic genes either directly as target genes or indirectly via control of translation, protein-protein interactions, or signalling pathways. For instance, mutations of the translation regulator FMRP or the chromatin remodelling complex subunit ARID1B resulted in phenotypes associated with synaptic dysfunction [102, 103]. Synaptic phenotypes observed in NDD models are diverse, including increased and decreased activity of the synaptic machinery [104, 105]. On the other hand, it has been reported that mutations of synaptic genes can also influence gene expression. For instance, deficiency of the ASD risk gene *SHANK3*, a scaffolding protein of glutamatergic synapses, resulted in the upregulation of Histone deacetylase 2 (*HDAC2*) [106]. Interestingly, in *Shank3*-deficient mice, increased nuclear translocation of β -catenin, which plays a crucial role in the canonical WNT signalling pathway that is important for proper neurodevelopment, was observed [106].

These examples show that mutations of NDD-risk genes can result in various phenotypes, which are not restricted to specific pathways and often overlap between different risk genes. Unravelling functional links between NDD-risk genes and common pathways might lead to the identification of targets suitable for therapeutic intervention.

1.5 The transcription factor MYT1L

One TF whose mutation is strongly associated with the development of NDDs is Myelin Transcription Factor 1-Like (MYT1L) [107, 108]. MYT1L is a CCHHC zinc finger (ZF) transcription factor which is highly expressed in post-mitotic neurons of the developing nervous system [109]. It is located on chromosome 2 in humans and on chromosome 12 in mice, and is one of three members of the conserved Myelin transcription factor (Myt)/Neural zinc finger (NZF) family. Expression of MYT1L and its family members, MYT1 and ST18, in the mammalian nervous system is spatially and temporally regulated during neuronal differentiation [110].

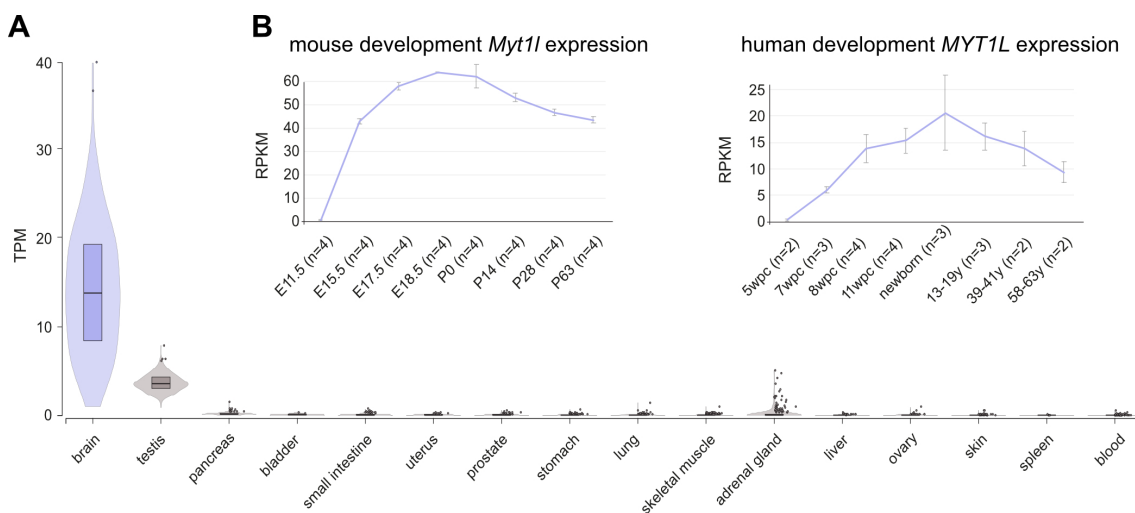


Figure 1.5: Expression of the transcription factor MYT1L. **(A)** Expression of *MYT1L* across different tissues shows that *MYT1L* is almost exclusively expressed in the brain. Tissue expression data from GTEx portal. **(B)** Expression of mouse *Myt1l* and human *MYT1L* over time shows a life-long expression, which slightly decreases during aging. Data from [111].

What makes MYT1L unique is that, in contrast to its family members, it is almost exclusively expressed in neurons in the brain and its expression is maintained throughout life [110–112] (Figure 1.5).

MYT1L has been found to be a strong reprogramming factor that, in combination with the proneural transcription factors ASCL1 and BRN2 (also called POU3F2), is capable of directly reprogramming fibroblasts into functional neurons [113–115]. Such reprogramming studies showed that MYT1L bound the core motif AAGTT and acted mainly as transcriptional repressor during neuronal reprogramming [116]. MYT1L can interact with epigenetic silencers such as SIN3/HDAC, which results in chromatin condensation and

hence transcriptional repression [116–119]. Among the target genes of MYT1L were negative regulators of neurogenesis, like members of the WNT and NOTCH signalling pathway, as well as transcriptional regulators of several non-neuronal lineages [116]. These data indicate that unlike common repressors, which inhibit specific lineages – such as REST, which inhibits neuronal genes – MYT1L appears to block expression of genes associated with many cell identities except for the neuronal one.

In a more physiological setting, Mall and colleagues have reported that *in utero* electroporation of *Myt1l*-shRNA results in impaired neurogenesis, and that MYT1L-depleted primary neurons show upregulation of non-neuronal gene expression and impaired functional properties [116]. This emphasises the important role of MYT1L in neuronal development.

While several *in vitro* studies provide evidence supporting the repressive function of MYT1L [116–118, 120], some studies using *in vitro* and *in vivo* models suggest that MYT1L can function as a transcriptional activator [117, 121–123]. This shows that the transcriptional role of MYT1L might be context-dependent. Further studies are needed to resolve its exact molecular function in physiologically-relevant models.

Given the crucial role of MYT1L in establishing neuronal identity, it can be assumed that *MYT1L* deregulation has severe consequences for proper brain function. Blanchet and colleagues have reported deregulation of NDD-associated TFs in *MYT1L*-knockout cells, indicating that MYT1L expression plays a role in the aetiology of NDDs [124]. Indeed, MYT1L has been strongly implicated in NDDs, including ASD, ID, epilepsy, and schizophrenia, with 98% (50 out of 51) of currently reported cases with heterozygous MYT1L deletion or loss of function mutations being diagnosed with ASD and/or intellectual disability. MYT1L depletion is more frequently associated with ASD and ID, while gene duplication has been observed in patients with schizophrenia [107]. Besides behavioural abnormalities, several MYT1L syndrome patients also present with obesity and brain malformations [82, 108, 124–137].

These studies show that *MYT1L* mutations might play a role in the development of NDDs. However, it is unclear whether they are sufficient to cause neurodevelopmental defects. The mechanisms by which MYT1L mutations contribute to disease phenotypes also remain elusive. During the course of this project, three mouse models have been published which report altered brain development and behavioural abnormalities upon MYT1L mutation [121, 138, 139]. While they begin to address the molecular mechanism following MYT1L

depletion, important questions about disease aetiology remain unanswered. Furthermore, none of these studies present the effect of MYT1L depletion in human neurons or, most importantly, potential therapeutic interventions for MYT1L syndrome patients.

1.6 Aims of the study

NDDs, which constitute a huge health burden all over the world, are not only associated with mutations of genes involved in the synaptic machinery [90] but also with the malfunction of transcriptional regulators [91], suggesting that gene deregulation is a central mechanism in such disorders. The TF MYT1L is one of few NDD-associated transcriptional regulators specifically expressed in neurons and whose expression is maintained throughout life [107, 110, 111]. However, its role in the aetiology of NDDs remains poorly understood.

The aim of this thesis was to investigate

- 1) whether *MYT1L* mutations are sufficient to cause NDD-associated phenotypes,
- 2) what underlying molecular mechanism is important for disease aetiology, and
- 3) whether symptoms caused by *MYT1L* haploinsufficiency can be targeted by therapeutic intervention.

To that end, I used MYT1L-depleted mice and embryonic stem cell (ESC)-derived human induced neurons (iNs) to analyse MYT1L depletion on a transcriptional, behavioural, and functional level in mouse and human models.

2 RESULTS

The results presented here are part of the manuscript entitled "MYT1L haploinsufficiency in human neurons and mice causes autism-associated phenotypes that can be reversed by genetic and pharmacologic intervention", which has been accepted for publication in Molecular Psychiatry. Parts of the text, figures and figure legends have been taken and adapted from the manuscript, originally co-written by myself (more details in the Contributions chapter).

2.1 Characterisation of MYT1L-deficient mice

To investigate whether MYT1L mutations alone can cause different NDD phenotypes observed in patients, I characterised *Myt1l*-mutant mice in terms of brain development, gene expression and behaviour.

2.1.1 MYT1L is essential for survival

Myt1l-mutant mice were generated by electroporation of CRISPR/Cas9 ribonucleoprotein (RNP) into zygotes, targeting exon 6 (first coding exon) of *Myt1l*. Offspring with a 7-bp deletion in exon 6 were used for further breeding (Figure 2.1 A, Figure S1). This mutation results in a frameshift at amino acid (aa) 11 and subsequent premature STOP codon at aa 78, which is similar to a reported patient case with a nonsense mutation at aa 75 in *MYT1L* [128]. *Myt1l*^{+/-} and *Myt1l*^{-/-} mice showed expected reduction in full-length MYT1L protein compared to *Myt1l*^{+/+} control at P0 (Figure 2.1 B) and MYT1L could barely be detected in the cortex of *Myt1l*^{-/-} mice at E15.5 (Figure 2.1 C). Genotypes of *Myt1l*-mutant mice matched Mendel's law of segregation at birth but *Myt1l*^{-/-} mice died within one week after birth (Figure 2.1 D), indicating that MYT1L is essential for survival.

While there was no nuclear cortical MYT1L signal in brain slices of *Myt1l*^{-/-} mice at E15.5, I detected a smaller molecular weight band upon *Myt1l* mutation at E18.5 and P0 in Western blot analysis of brain lysates (Figure 2.2 A). Gene expression analysis confirmed the expected 7-bp deletion in exon 6 of *Myt1l* transcript but showed that there was no nonsense-mediated decay but

rather an increase of mutant *Myt1l* transcript with the 7-bp deletion (Figure 2.2 B, C).

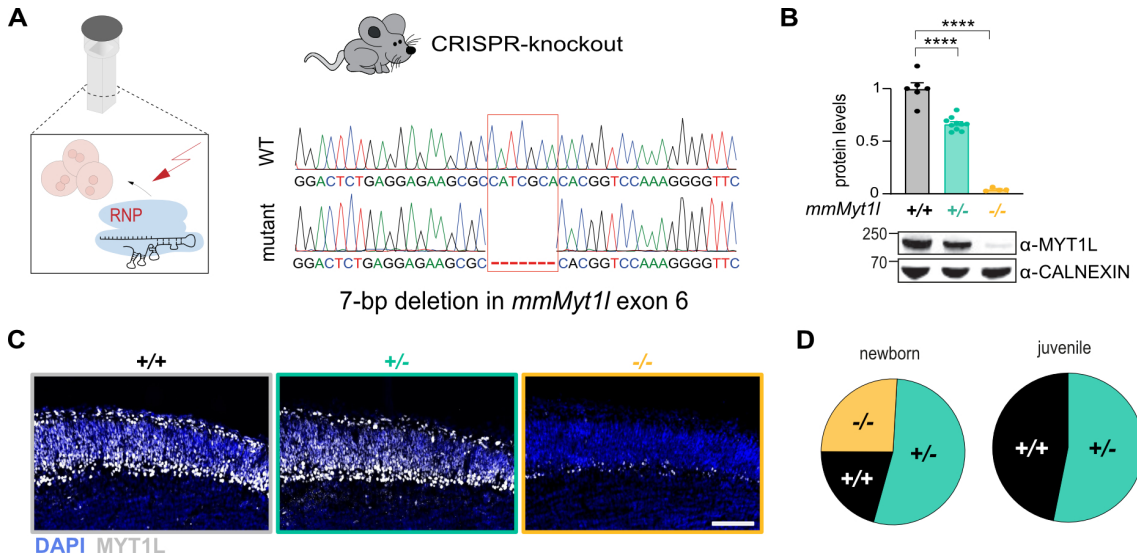


Figure 2.1: Full-length MYT1L protein is crucial for survival. (A) Schematic of introducing a 7-bp frameshift germline mutation in exon 6 (first protein coding exon) of *Myt1l* using CRISPR/Cas9 ribonucleoprotein (RNP) electroporation into zygotes. The depletion was confirmed by Sanger sequencing. (B) Western blot quantification of full-length MYT1L protein levels in mutant mice at P0 normalised to control. Representative Western blot images using indicated antibodies are shown. (C) Representative brain sections of E15.5 mouse cortices from *Myt1l*^{+/+} and *Myt1l*^{-/-} mice show the expected decrease of nuclear MYT1L immunofluorescence signal compared to *Myt1l*^{+/+} controls. Scale bar 100 μ m. (D) Survival pie chart from *Myt1l*^{+/+} x *Myt1l*^{+/+} offspring at P0 (8 litters; n = 12 (*Myt1l*^{+/+}, black), 31 (*Myt1l*^{+/-}, teal), 15 (*Myt1l*^{-/-}, yellow)) and after weaning at P21 (7 litters; n = 15 *Myt1l*^{+/+}, 17 *Myt1l*^{+/-}, 0 *Myt1l*^{-/-}) indicate that homozygous *Myt1l*-mutant mice die after birth. Bar graph shows mean values, data points from individual animals are displayed, error bars = SEM, unpaired t-test **** p < 0.0001. (Weigel et al., 2023)

To further analyse the smaller molecular weight MYT1L protein, I performed immunoprecipitation of endogenous MYT1L from *Myt1l*^{+/+} and *Myt1l*^{-/-} brains at P0, followed by mass spectrometry analysis. I detected *de novo* peptides resulting from the frameshift in *Myt1l*^{-/-} samples but not in *Myt1l*^{+/+} controls. However, I found wild type MYT1L peptides in *Myt1l*^{-/-} samples downstream of the predicted STOP codon at aa 78. This indicates that due to lack of nonsense-mediated decay, an internal methionine at aa 99 was used as alternative START to produce N-terminally-truncated MYT1L protein in *Myt1l*-mutant mice (Figure 2.2 D). To investigate whether this isoform (aa 99 - 1187) could explain the smaller molecular weight band detected in Western blot, I cloned a lentiviral overexpression construct with the N-terminally-truncated *Myt1l* isoform and transduced mouse primary hippocampal cultures with the truncation or full-length *Myt1l* control (Figure 2.2 E).

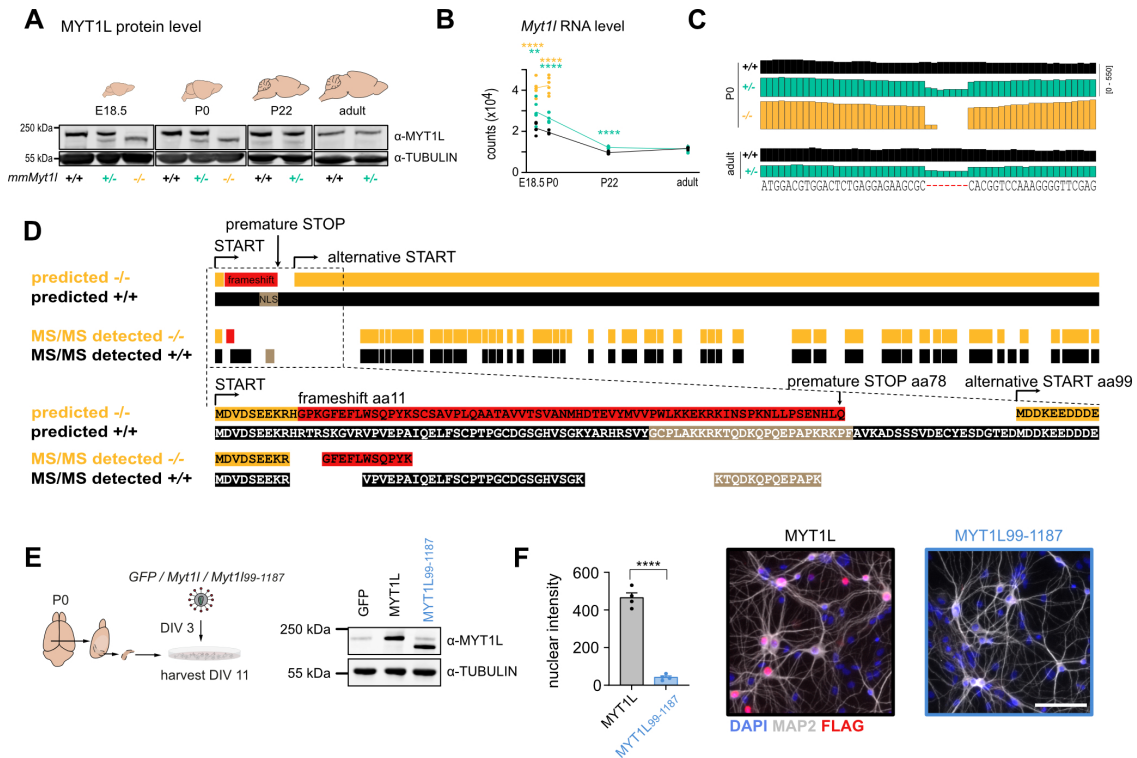


Figure 2.2: N-terminally-truncated MYT1L protein in *Myt1l*-mutant mice. (A) Western blot analysis showed the expected depletion of full-length MYT1L but a smaller molecular weight band was detected in mutants at E18.5 and P0. (B) Normalised read counts of *Myt1l* showed no nonsense-mediated decay in MYT1L-deficient mice. ** p-adj < 0.01, **** p-adj < 0.0001. (C) *Myt1l* transcript tracks confirmed the expected 7-bp deletion in exon 6 of *Myt1l* RNA. For RNA-Seq analysis $n \geq 5$ E18.5, $n \geq 4$ P0 for (*Myt1l*^{+/+}, black), (*Myt1l*^{+/-}, teal) and (*Myt1l*^{-/-}, yellow), respectively; $n = 6$ P22, $n \geq 3$ adult for (*Myt1l*^{+/+}) and (*Myt1l*^{+/-}), respectively. (D) Immunoprecipitation of endogenous MYT1L from *Myt1l*^{-/-} (P0, $n = 3$) and *Myt1l*^{+/+} control (P0, $n = 3$) brains followed by mass spectrometry analysis revealed the expected *de novo* peptides resulting from the frameshift at aa 11 in *Myt1l*^{-/-} but not in *Myt1l*^{+/+} conditions. There are MYT1L peptide fragments starting after aa 181 in *Myt1l*^{-/-}, suggesting that an internal methionine at aa 99 was used to produce N-terminally truncated (aa 99 - 1187) MYT1L. This isoform would explain the lower molecular weight band in Western blot, but would lack the nuclear localisation signal (NLS) aa 54-82. (E) Overexpression of full-length and N-terminally truncated (aa 99 - 1187) MYT1L at day in vitro 3 (DIV 3) in primary hippocampal cultures shown at DIV 11 by representative Western blot. (F) Nuclear intensity of FLAG-tagged truncated MYT1L (aa 99 - 1187) compared to full-length control at DIV 11 after overexpression as in panel E. Representative immunofluorescence images with indicated antibodies are shown, scale bar 100 μ m. Bar graph shows mean values, data points from individual animals are displayed, error bars = SEM, unpaired t-test **** p < 0.0001. (Weigel et al., 2023)

The MYT1L protein band detected upon transduction with the truncated *Myt1l* construct on Western blot matched the size of the smaller molecular weight band in *Myt1l*-mutant mice (Figure

2.2 A). This indicates that the internal methionine at aa 99 is indeed used as alternative START upon *Myt1l* mutation. However, this isoform would lack the predicted nuclear localisation signal (NLS, aa 54 - 82) (Figure 2.2 D).

To analyse whether lack of the NLS prevents entry of truncated MYT1L into the nucleus, I over-expressed FLAG-tagged truncated and full-length MYT1L in primary hippocampal cultures and measured FLAG intensity in the nucleus (Figure 2.2 F). In line with the immunostainings of E15.5 cortex, truncated MYT1L could not be detected in the nucleus of the cells. These data indicate that lack of nonsense-mediated decay of *Myt1l*-mutant transcript results in the production of an N-terminally-truncated MYT1L protein that fails to translocate to the nucleus due to lack of the NLS and is therefore expected to be non-functional.

The findings in this section strongly indicate that the mouse model is suitable as MYT1L loss-of-function model and show that full-length MYT1L is essential for survival, which is in line with the observation that so far only heterozygous *MYT1L* mutations have been reported in patients [108].

2.1.2 Impaired brain development in *Myt1l*-deficient mice

It has been shown that MYT1L can enhance neuronal identity *in vitro* by repressing negative regulators of neurogenesis, such as members of the WNT and NOTCH signalling pathway [116]. I therefore investigated whether lack of MYT1L impairs neurogenesis *in vivo*. Pregnant mice were injected with 5-Ethynyl-2-deoxyuridine (EdU) at E14.5 to mark all proliferating cells and embryos were harvested 20 h later. By co-staining of EdU and the proliferation marker Ki67 in the cortex of E15.5 brains, the fraction of cells exiting the cell cycle over a 20-h period (Q fraction) could be determined. I detected a decrease in Q fraction of 37% in *Myt1l*^{-/-} mice compared to *Myt1l*^{+/+} control, while the number of EdU+ cells was similar between genotypes (Figure 2.3 A). This indicates that a comparable number of cells proliferated in the ventricular zone (VZ) and subventricular zone (SVZ) in *Myt1l*-mutant and control mice between E14.5 and E15.5, but upon MYT1L depletion, cells failed to exit the cell cycle, suggesting impaired neurogenesis.

To investigate the impact of this failure to exit the cell cycle on the cortical stem cell and progenitor pool, I stained brain sections of E15.5 and P0 mice for the neural stem cell marker SOX2 and IPC marker TBR2. At E15.5, SOX2+ and TBR2+ populations were unchanged in *Myt1l*-mutant and control mice (Figure 2.3 B). However, at P0, the SOX2+ neural stem cell pool was significantly increased in *Myt1l*^{+/-} and *Myt1l*^{-/-} mice compared to *Myt1l*^{+/+} control, while the number of TBR2+ cells remained largely unchanged (Figure 2.3 C).

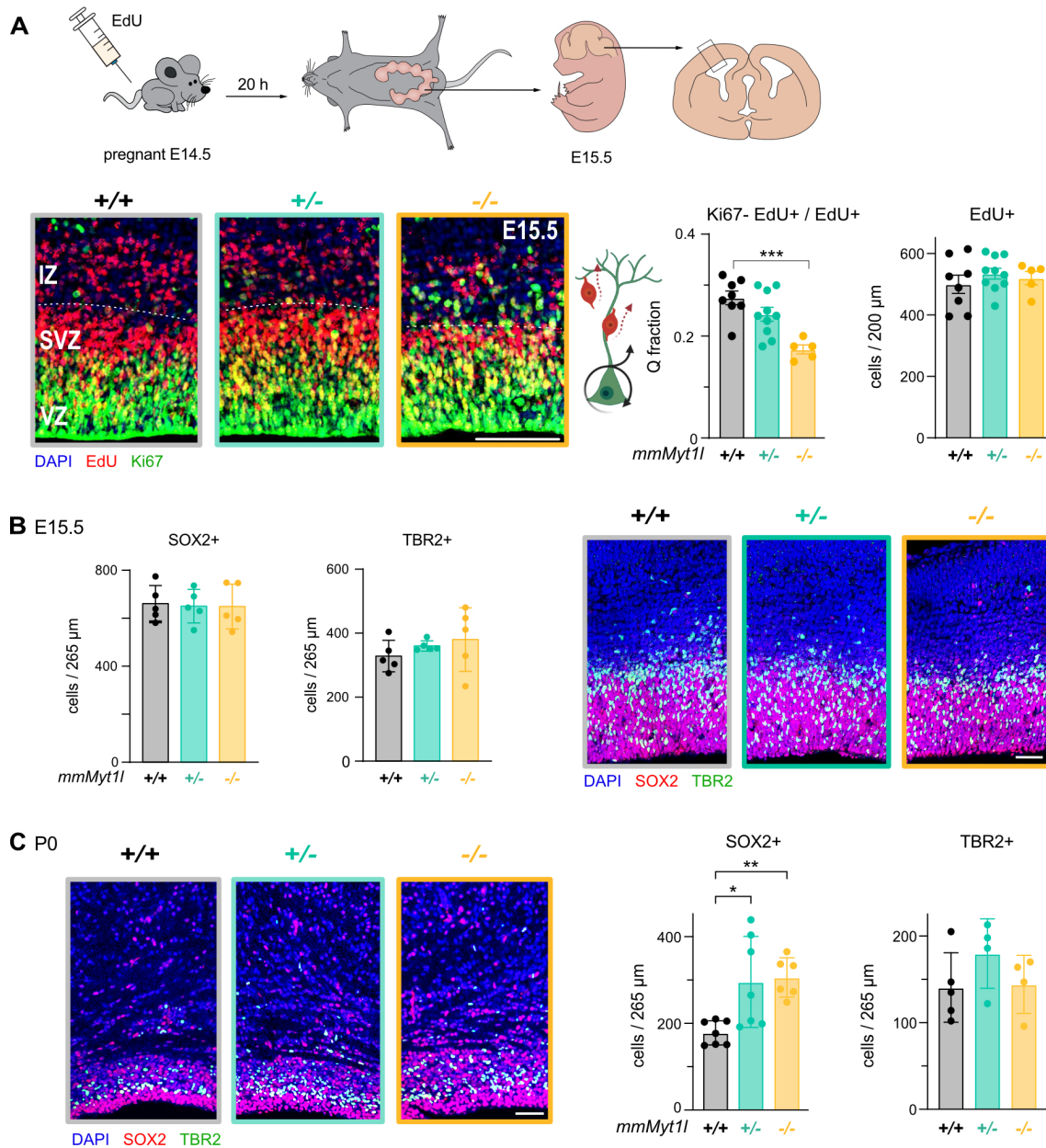


Figure 2.3: MYT1L depletion impairs neurogenesis in mice. (A) Pregnant mice were injected intraperitoneally with EdU at E14.4 and embryos were harvested after 20 h to measure the number of cells that exited cell cycle in the developing cortex between E14.5 and E15.5. Representative images and quantifications of EdU+ cells after the 20-h pulse and Q fraction (ratio of EdU+Ki67- over all EdU+ cells) in the cortical ventricular zone (VZ) and subventricular zone (SVZ) of (*Myt1l*^{+/+}, black), (*Myt1l*^{+/-}, teal) and (*Myt1l*^{-/-}, yellow) E15.5 mice. IZ: intermediate zone, $n \geq 5$, scale bar 100 μ m. (B) Quantification of SOX2+ or TBR2+ cells in the cortex of *Myt1l*^{+/-} and *Myt1l*^{-/-} mice compared to *Myt1l*^{+/+} control at E15.5 across the same area of the entire cortex. Representative images of a ventricular and subventricular zone magnification stained with indicated antibodies are shown. $n = 5$, scale bar 50 μ m. (C) Same analysis as in panel B for *Myt1l*^{+/-} and *Myt1l*^{-/-} mice compared to *Myt1l*^{+/+} control at P0. $n \geq 4$, scale bar 50 μ m. Bar graphs show mean values with data points from individual animals, error bars = SEM, One-way ANOVA * $p < 0.05$, ** $p < 0.01$, *** $p < 0.001$. (Weigel et al., 2023)

This suggests that failure to exit cell cycle in *Myt1l*-mutant mice at E15.5 results in an increased stem cell population in newborn mice.

Since altered neuronal differentiation dynamics might affect brain structure, I next isolated brains from *Myt1l*-mutant and control mice at P0 for anatomical analysis. I detected a significantly decreased NEUN⁺ cortical thickness in *Myt1l*^{+/-} and *Myt1l*^{-/-} sections compared to *Myt1l*^{+/+} control at different anteroposterior positions (Figure 2.4 A). Overall brain size was similar between genotypes (Figure 2.4 B) but the weight of *Myt1l*-mutant mice and their brains was lower at birth (Figure 2.4 C, E), resulting in an increased brain length to weight ratio upon *Myt1l* mutation (Figure 2.4).

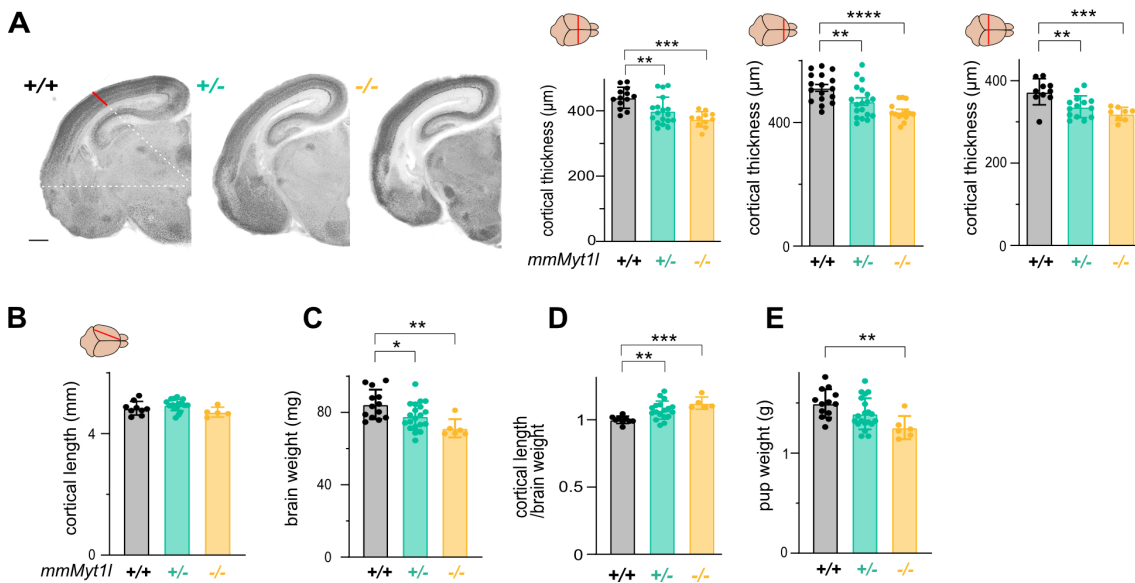


Figure 2.4: *Myt1l*-deficient mice have thinner cortices. (A) Cortical thickness of *Myt1l*^{+/+}, *Myt1l*^{+/-} and *Myt1l*^{-/-} brains at P0. Representative sections of the mid-brain area stained with NeuN and quantification of absolute cortical thickness at three locations in the cortex are shown. sections of $n = 3$, scale bar $500 \mu\text{m}$. (B) Quantification of absolute cortical length of *Myt1l*^{+/+}, *Myt1l*^{+/-} and *Myt1l*^{-/-} brains at P0. $n \geq 5$. (C) *Myt1l*^{+/-} and *Myt1l*^{-/-} brains at P0 weighed less compared to *Myt1l*^{+/+} control. $n \geq 6$. (D) Quantification of cortex length normalised by brain weight for *Myt1l*^{+/+}, *Myt1l*^{+/-} and *Myt1l*^{-/-} brains at P0. $n \geq 5$. (E) Weight of *Myt1l*^{+/+}, *Myt1l*^{+/-} and *Myt1l*^{-/-} mice at birth (P0). $n \geq 6$. Red lines indicate location of measured features. Bar graphs show mean values, data points from individual animals or sections are displayed, error bars = SEM, Mann-Whitney t-test * $p < 0.05$, ** $p < 0.01$, *** $p < 0.001$ **** $p < 0.0001$. (Weigel et al., 2023)

These results suggest that loss of MYT1L results in impaired neurogenesis in mice, which in turn causes structural brain abnormalities. Interestingly, brain malformations have also been described for some MYT1L-syndrome patients [107, 108].

2.1.3 MYT1L depletion causes NDD-associated gene deregulation

I next examined the effects of MYT1L depletion on gene expression across brain development. To this end, I performed bulk RNA-Sequencing (RNA-Seq) of mouse prefrontal cortices at E18.5, P0, P22 and three months (adult). Several hundred genes were significantly deregulated in *Myt1l*-deficient mice compared to controls at all time points, while early (E18.5 and P0) and late (P22 and adult) developmental stages showed similar deregulation patterns, respectively (Figure 2.5 A).

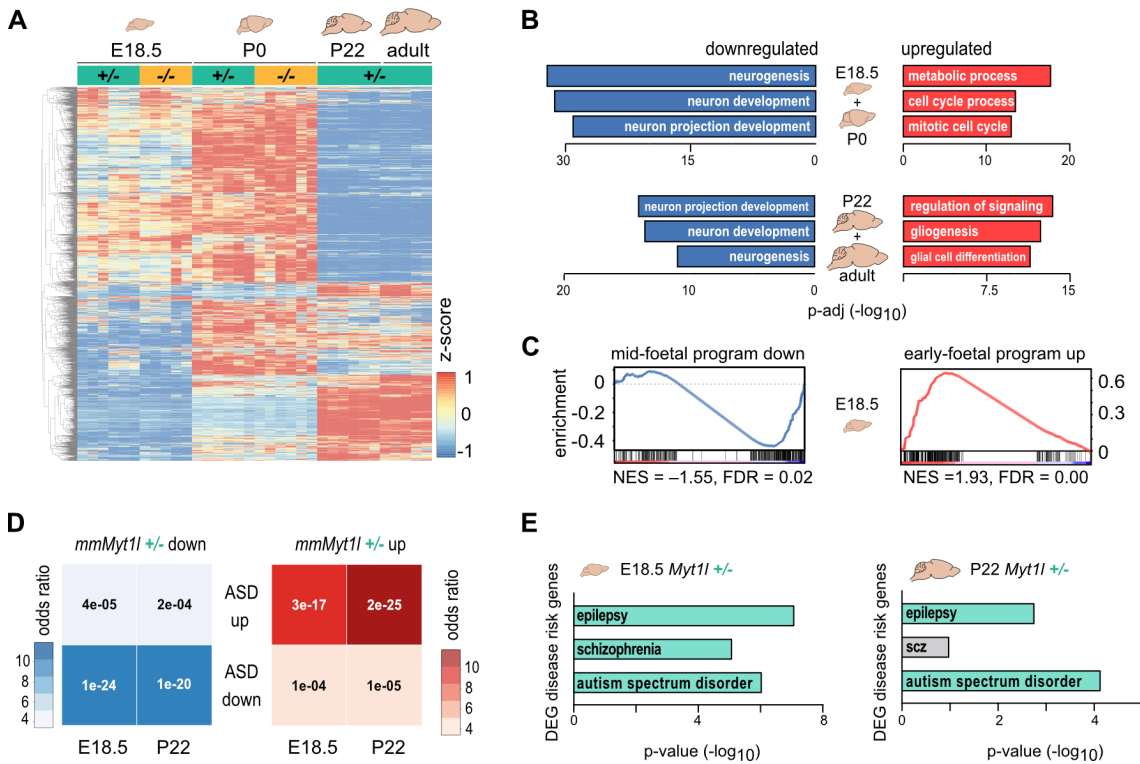


Figure 2.5: *Myt1l*-deficient mice show gene deregulation associated with neurodevelopmental disorders. (A) Row-scaled heatmap of deregulated genes upon *Myt1l* mutation across all replicates and stages. (B) Selected top gene ontology (GO) terms of genes that were down- (blue) or upregulated (red) upon *Myt1l* mutation in the prefrontal cortex of mice compared to control at indicated timepoints during development. (C) Gene set enrichment analysis (GSEA) plots show depletion of mid-foetal (blue) and enrichment of early-foetal (red) neural development-related gene sets among genes deregulated in *Myt1l*-mutant brains at E18.5 [140]. NES, normalised enrichment score; FDR, false discovery rate. (D) Overlap of genes up- or downregulated upon *Myt1l* mutation in mouse cortex at E18.5 and P22 and genes that are up- or downregulated in ASD patient brains determined by GeneOverlap [141]. (E) Deregulated genes in MYT1L-deficient mouse brains at E18.5 and P22 display significant (teal) overlap with genes linked to epilepsy [142], schizophrenia [143], and ASD [144] (score 1, accessed Dec2020) determined by Fisher's exact test. $n \geq 5$ E18.5, $n \geq 4$ P0 for (*Myt1l*^{+/+}, black), (*Myt1l*^{+/-}, teal) and (*Myt1l*^{-/-}, yellow), respectively; $n = 6$ P22, $n \geq 3$ adult for (*Myt1l*^{+/+}) and (*Myt1l*^{+/-}), respectively. (Weigel et al., 2023)

Gene ontology (GO) analysis revealed neurogenesis-associated terms among downregulated and cell division terms among upregulated genes at early stages (Figure 2.5 B), which is in line with the reduced Q-fraction at E15.5 and increased neural stem cell pool at birth (Figure 2.3 A, C). Downregulation of neuronal terms persisted in later stages, while I detected signalling and non-neuronal terms for upregulated genes upon *Myt1l* mutation (Figure 2.5 B). Furthermore, I observed a depletion of late-foetal gene expression signatures and an enrichment of early-foetal signatures in late development in *Myt1l*-mutant mice at E18.5 (Figure 2.5 C) [140]. This has also been reported for other ASD mouse models [92] and indicates that MYT1L depletion causes delays in brain development. I saw an overall enrichment of genes associated with epilepsy [142], schizophrenia [143] and ASD [144] among the deregulated genes upon MYT1L depletion in mice before and after birth (Figure 2.5 E). Additionally, I discovered that genes upregulated in ASD patients were also upregulated in our *Myt1l*-deficient mice, while genes downregulated in *Myt1l*-mutant mice were also downregulated in ASD patients (Figure 2.5 D) [141].

Overall, the data in this section confirm impaired neurogenesis in *Myt1l*-deficient mice and show that MYT1L depletion in mice causes deregulation of gene expression as observed in NDD patients.

2.1.4 Transcriptional enrichment of several non-neuronal signatures in *Myt1l*-deficient mice

It has been reported in several reprogramming studies that MYT1L promotes neuronal fate by repressing non-neuronal gene programs [116, 145, 146].

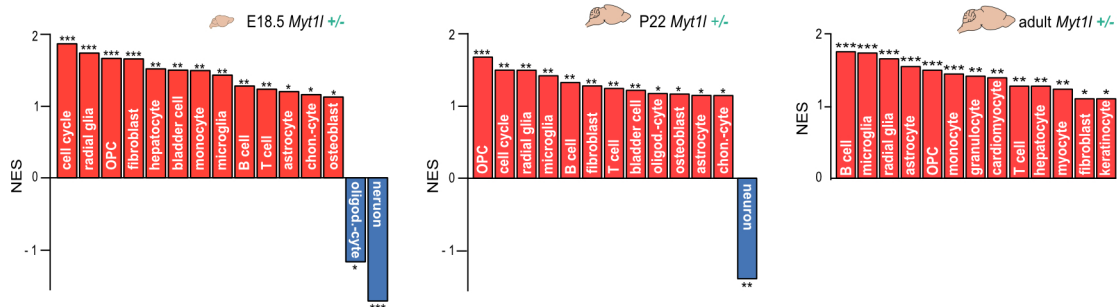


Figure 2.6: Upregulation of non-neuronal signatures in *Myt1l*-deficient mice. Gene set enrichment analysis (GSEA) showed that several non-neuronal gene signatures were increased (red) in MYT1L-mutant brains at E18.5, P22, and 3 months, while neuronal signatures were decreased (blue) at E18.5 and P22. Shown are normalised enrichment scores (NES) of signatures with false discovery rate (FDR) ≤ 0.2 . FDR * < 0.2 , ** < 0.1 , *** < 0.01 . $n \geq 5$ E18.5, $n = 6$ P22, $n \geq 3$ adult for (*Myt1l*^{+/+}) and (*Myt1l*^{+/-}), respectively. (Weigel et al., 2023)

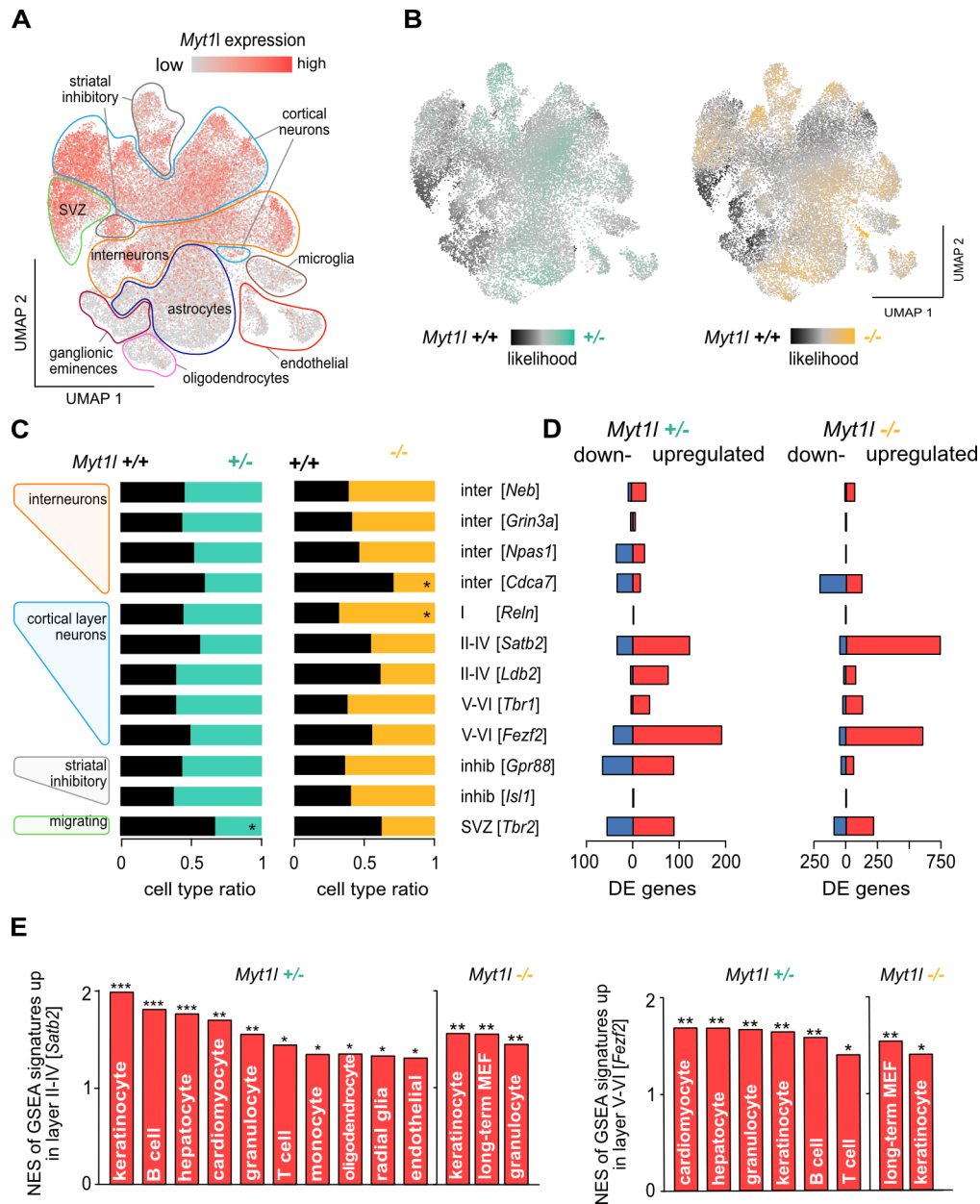


Figure 2.7: No new cell clusters in *Myt1l*-depleted mouse prefrontal cortex. (A) Single cell RNA-Seq of MYT1L-deficient prefrontal cortices at P0 confirms expression of *Myt1l*^{+/+} in neuronal cell populations. Cell type assignment is based on reference data from [147]. (B) Likelihood analysis of observing MYT1L-deficient (*Myt1l*^{+/-}, teal or *Myt1l*^{-/-}, yellow) and control (*Myt1l*^{+/+}, black) cell enrichment in populations of specific cell types using MELD. (C) Ratio of MYT1L-deficient (*Myt1l*^{+/-} or *Myt1l*^{-/-}) and control (*Myt1l*^{+/+}) cells in indicated cell type clusters. * FDR < 0.01 abs(Log2FC) > 1. (D) Number of genes deregulated upon *Myt1l* mutation across indicated cell types and MELD clusters. Shown are genes that are down- (blue) or upregulated (red) upon MYT1L deficiency with absolute log2 fold change > 0.1 and p-adj < 0.05. (E) Several non-neuronal signatures were increased (red) upon MYT1L depletion in layer II-IV (left) and layer V-IV (right) neurons based on Gene set enrichment analysis (GSEA). Shown are normalised enrichment scores (NES) of signatures with false discovery rate (FDR) ≤ 0.25. FDR * < 0.25, ** < 0.1, *** < 0.01. n = 2 for *Myt1l*^{-/-} (10503 cells), *Myt1l*^{+/-} (13688 cells) and *Myt1l*^{+/+} (12072 cells), respectively. (Weigel et al., 2023)

In line with these results, I observed enrichment of several non-neuronal cell fate signatures upon MYT1L depletion in E18.5, P22 and adult mice, while neuronal signatures were depleted at E18.5 and P22 according to Gene set enrichment analysis (GSEA) (Figure 2.6).

Based on these data, I asked myself whether *Myt1l*-deficient brains contain cell types that are usually not expressed in the brain. This question of cell type composition can be addressed using single cell RNA sequencing (scRNA-Seq). I performed scRNA-Seq of the prefrontal cortex of *Myt1l*-mutant and control mice at birth. The expression of *Myt1l* was confirmed in neuronal cell populations and no loss or emergence of cell clusters that would indicate drastic changes in cell type composition could be found upon MYT1L depletion (Figure 2.7 A, B). To identify cell populations that are specifically affected by *Myt1l* mutation, the MELD algorithm was used, which calculates a likelihood estimate of observing each cell for each genotype (Figure 2.7 B) [148]. There were only minor changes in cell type ratios between *Myt1l*-mutant and control mice, e.g. *Cdca7*+ interneurons were slightly reduced, whereas cortical layer I neurons (*Reln*+) were slightly increased in *Myt1l*^{-/-} mice (Figure 2.7 C). Interestingly, deregulated genes in the different cell type clusters were predominantly upregulated upon MYT1L depletion (Figure 2.7 D). In accordance with bulk RNA-Seq results (Figure 2.6), I observed enrichment of several non-neuronal gene signatures, even in cells annotated with cortical layer neuron identity (Figure 2.7 E).

These data show that *Myt1l*-mutant cells fail to silence inappropriate gene expression programs, which does not result in the emergence of non-neuronal cell types in the brain but causes a "confused" transcriptional identity in neurons *in vivo*.

2.1.5 MYT1L predominantly acts as repressor in mice

The scRNA-Seq analysis showed a predominant upregulation of genes upon MYT1L depletion in neuronal cell populations for mouse cortex (Figure 2.7 D), suggesting that MYT1L, as proposed in previous studies [116, 118, 120], plays a role as transcriptional repressor.

To further investigate the transcriptional function of MYT1L *in vivo*, I determined MYT1L target genes by performing CUT&RUN [149] using the cortices of wild type mice at E18.5, P0 and three months (Figure 2.8 A). I found that many MYT1L chromatin binding sites overlapped at different developmental stages and the MYT1L DNA-binding motif (AAAGTT) was significantly enriched throughout development (Figure 2.8 B, C). Checking the MYT1L target genes against the deregulated genes in mouse prefrontal cortex across development showed that many genes did not overlap, suggesting that several changes in the bulk samples are indirect. Inconsistent with the role of MYT1L as repressor, I saw similar numbers of direct target genes up- or downregulated upon MYT1L depletion in heterozygous brain samples (Figure S2). On the other hand, for homozygous samples, 60% of direct MYT1L target genes were upregulated upon *Myt1l* mutation (Figure S2). However, since bulk samples contain several non-neuronal cells that do not express

Myt1l, and effects could thereby be indirect or masked, I used the single cell data to investigate the transcriptional role of MYT1L in neurons.

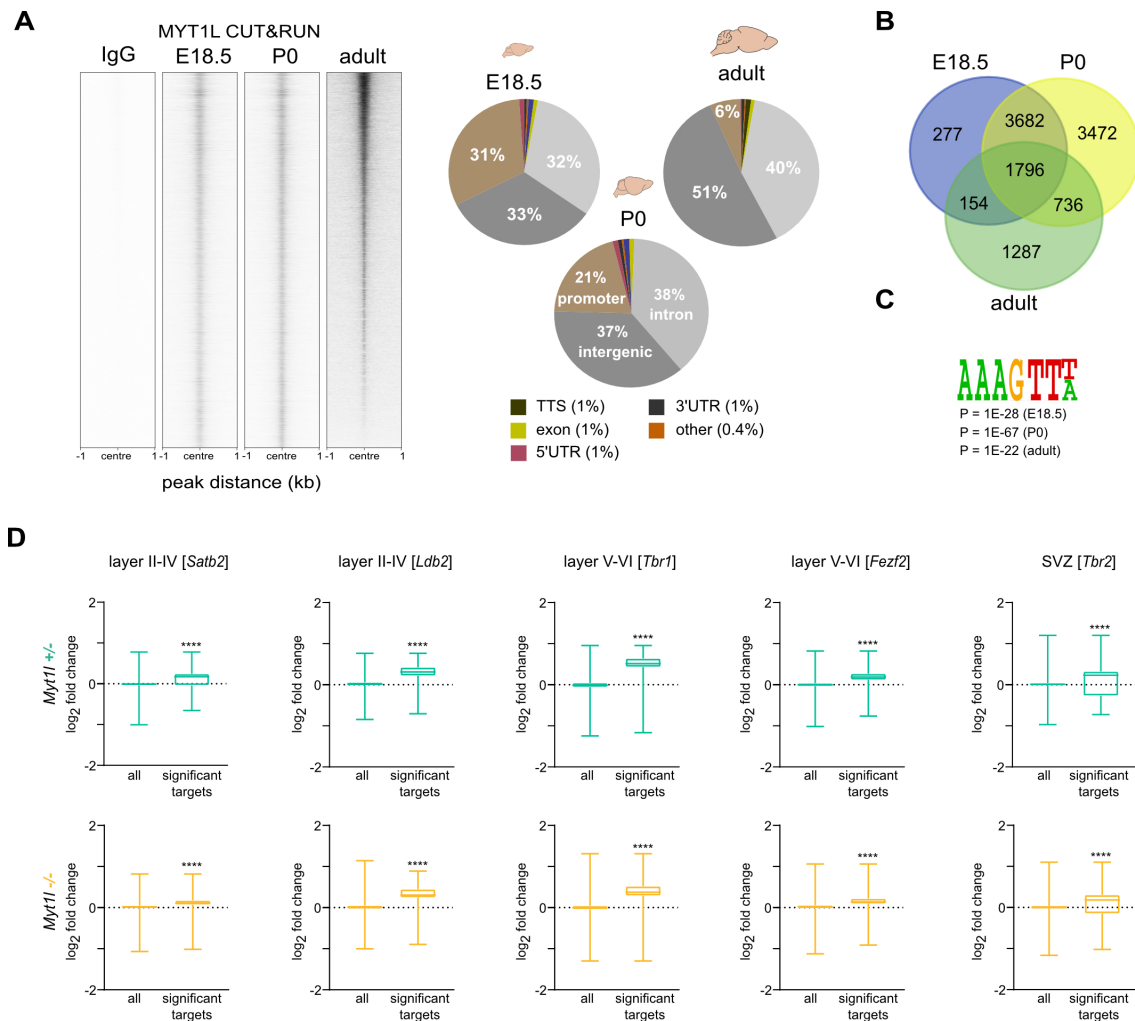


Figure 2.8: Expression changes of MYT1L target genes. **(A)** Genome-wide occupancy profiles of endogenous MYT1L in the prefrontal cortex of wild type mice determined by CUT&RUN at E18.5 ($n = 3$), P0 ($n = 3$) and adult stage ($n = 3$) and pie charts indicating the distribution of detected MYT1L-bound sites at annotated genomic regions. **(B)** Overlap of the MYT1L target genes (peaks called 5 kb from transcription start site) at different time points during development. **(C)** The MYT1L DNA-binding motif (AAAGTT) is significantly enriched at bound sites at all developmental stages. **(D)** Comparison of genome-wide expression changes and expression changes of significantly deregulated MYT1L target genes (P0 MYT1L CUT&RUN peak 5 kb from transcription start site) for indicated single cell populations of *Myt1l*-mutant cortices compared to control at P0. Mann-Whitney test **** $p < 0.0001$. $n = 2$ for *Myt1l*^{-/-} (10503 cells), *Myt1l*^{+/-} (13688 cells) and *Myt1l*^{+/+} (12072 cells), respectively. (Weigel et al., 2023)

To that end, I compared genome-wide expression changes within different neuronal populations from scRNA-Seq analysis at P0 with expression changes at MYT1L chromatin binding sites and saw that direct MYT1L target genes were significantly upregulated upon heterozygous and homozygous MYT1L depletion (Figure 2.8 D).

This suggests that MYT1L predominantly acts as transcriptional repressor in neurons *in vivo*.

2.1.6 Hyperactivity and male-specific social deficits upon MYT1L depletion in mice

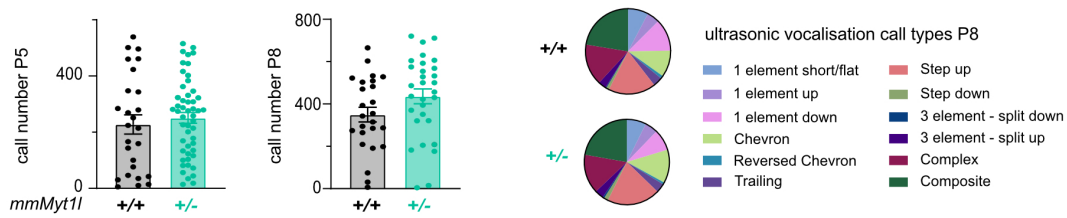
Since *MYT1L* mutations are associated with several behavioural anomalies, including hyperactivity and social deficits [123], I next performed behaviour experiments with *Myt1l*-deficient and control mice. Ultrasonic vocalisation analysis showed a trend towards increased vocalisation in one week-old *Myt1l*-deficient mice, but the number and type of calls were not significantly changed compared to control (Figure 2.9 A). In open field and elevated plus maze tests, I observed that *Myt1l*^{+/-} mice moved a lot more and spent significantly more time in centre regions and open arms, respectively (Figure 2.9 B, C). I also observed increased locomotion and exploratory rearing behaviour of adult *Myt1l*-deficient mice in home cage observations (Figure 2.9 D). In addition, I detected a significant decrease in marble burying and grooming events, which are used to evaluate repetitive behaviours but also represent decreased anxiety-like behaviours (Figure 2.9 D, E).

These results indicate that MYT1L-deficient mice are hyperactive and less anxious compared to controls, which are phenotypes that have previously been described in MYT1L and other NDD mouse models [121, 150, 151].

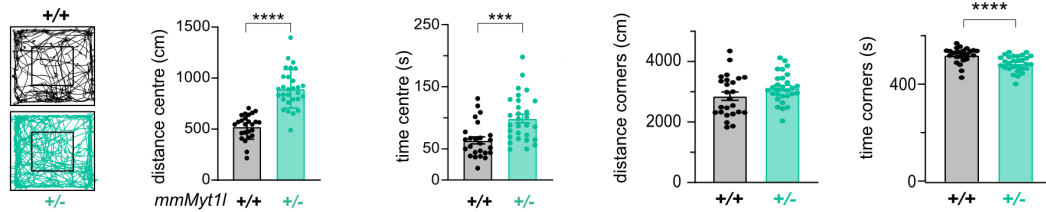
To assess social behaviour of *Myt1l*-mutant mice, I performed the three-chamber test with one month-old animals. In the first trial, all animals displayed the expected preference for investigating the chamber with a familiar littermate as opposed to an empty one (Figure 2.10 A). In the second trial, wild type and female *Myt1l*^{+/-} mice spent more time exploring the chamber with a newly-added unfamiliar mouse compared to the littermate. However, *Myt1l*^{+/-} males did not demonstrate such a preference for social novelty (Figure 2.10 B). Interestingly, a similar phenotype has also been described recently in another MYT1L mouse model [121].

In summary these results show that MYT1L depletion causes NDD-associated behavioural abnormalities, including sex-independent hyperactivity and male-specific social deficits in mice.

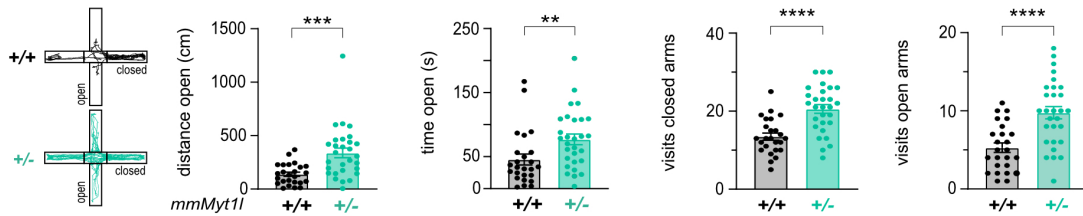
A ultrasonic vocalisation



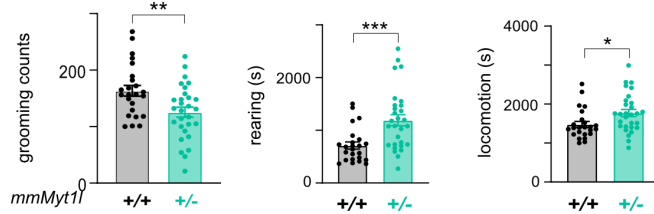
B open field



C elevated plus maze



D home cage observation



E marble burying

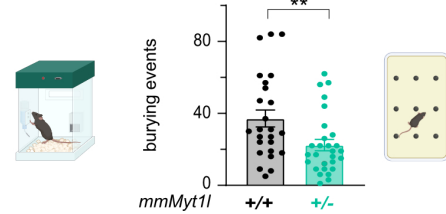


Figure 2.9: MYT1L depletion results in behavioural phenotypes in mice. (A) Number of ultrasonic vocalisations (USVs) in $Myt1l^{+/-}$ compared to $Myt1l^{+/+}$ control mice at P5 and P8. Pie chart comparing indicated call types at P8 between $Myt1l$ -mutant mice and controls. P5: $n = 26$ for $Myt1l^{+/+}$ and $n = 51$ for $Myt1l^{+/-}$, P8: $n = 25$ for $Myt1l^{+/+}$, $n = 30$ for $Myt1l^{+/-}$. (B) Open field test showed that $Myt1l^{+/-}$ mutants covered more distance and spent more time in centre regions compared to control animals at P23. $n = 25$ for $Myt1l^{+/+}$ and $n = 29$ for $Myt1l^{+/-}$. (C) Elevated plus maze observations showed that at P22, $Myt1l^{+/-}$ mice, due to hyperactivity, spent more time and moved more within open arms and visited both closed and open arms more often compared to control animals. $n = 25$ for $Myt1l^{+/+}$ and $n = 29$ for $Myt1l^{+/-}$. (D) LABORAS automated home cage observation of indicated features in two months-old mice. $n = 24$ for $Myt1l^{+/+}$ and $n = 29$ for $Myt1l^{+/-}$. (E) In marble burying experiments, $Myt1l^{+/-}$ mutants exhibited decreased number of burying events compared to controls. $n = 25$ for $Myt1l^{+/+}$ and $n = 28$ for $Myt1l^{+/-}$. Cartoons in panel D and E are taken from BioRender. Behaviour experiments were performed using three independent cohorts. Bar graphs show mean values with data points from individual animals, error bars = SEM, Mann-Whitney test * $p < 0.05$, ** $p < 0.01$, *** $p < 0.001$, **** $p < 0.0001$. (Weigel et al., 2023)

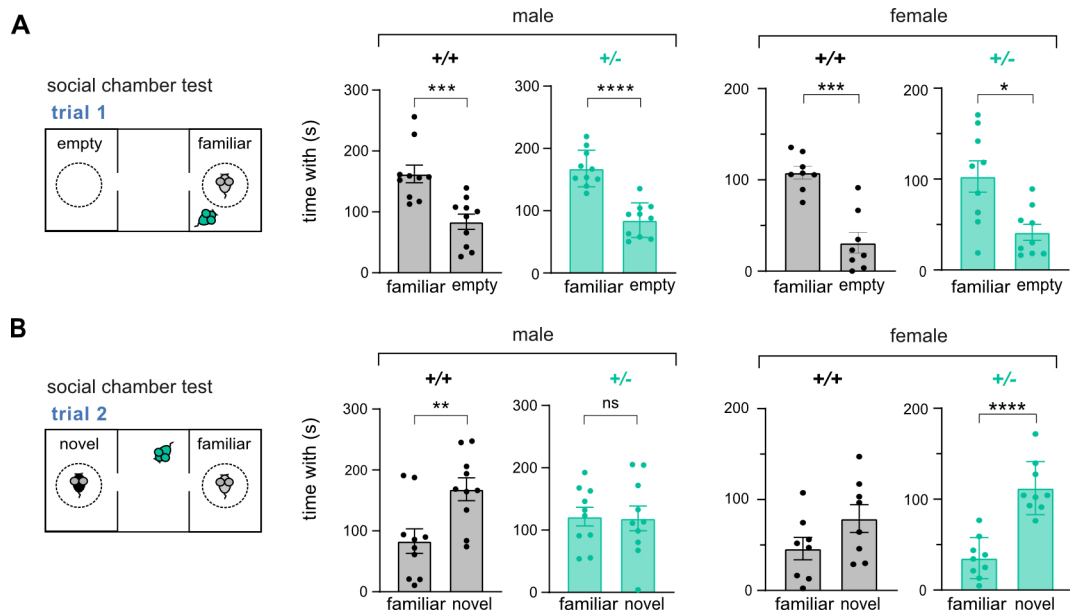


Figure 2.10: Male-specific social deficits in *Myt1l*-deficient mice. (A) Social chamber experiments showed that male and female *Myt1l*^{+/-} mutants, like controls, displayed expected preference for the chamber harbouring a littermate (familiar) compared to the empty one. (B) Male *Myt1l*^{+/-} mutants did not show the expected preference to spent time with novel mice of the same sex compared to familiar littermates. Female *Myt1l*^{+/-} mice did not present with social deficits in this test. Measurements were performed at the age of one month. n = 8 for *Myt1l*^{+/+}, n = 9 for *Myt1l*^{+/-} for females and n = 10 for *Myt1l*^{+/+}, *Myt1l*^{+/-} for males from three independent cohorts. Bar graphs show mean values, data points from individual animals are displayed, error bars = SEM, Mann-Whitney-test * p < 0.05, ** p < 0.01, *** p < 0.001, **** p < 0.0001, ns not significant. (Weigel et al., 2023)

2.2 Effect of MYT1L depletion in human neurons

The use of animal models has been very important to broaden our understanding of the biology of NDDs [96]. However, to capture potential human-specific biology and disease mechanisms, human models are needed.

2.2.1 MYT1L predominantly acts as repressor in human neurons

To investigate the role of MYT1L in human neurons and to study the effect of heterozygous MYT1L loss-of-function mutations, I used engineered human embryonic stem cells (hESCs) with a heterozygous conditional knockout allele of MYT1L exon 7 (*MYT1L*^{+/*fl*}). Human neurons can be generated from *MYT1L*^{+/*fl*} hESCs by overexpression of the proneuronal transcription factor NGN2 [152] and can mature into electrically active neurons upon co-culture with mouse glia cells. By expression of cre-recombinase or inactive, truncated Δcre-recombinase in the cells,

developmental processes as well as neuronal gene expression and physiology upon *MYT1L* depletion can be analysed in a conditional manner without clonal variation (Figure 2.11 A, Figure S3) [153–155].

Cre-mediated *MYT1L*^{+/-} deletion resulted in the expected MYT1L protein reduction compared to *MYT1L*^{+/+} control, mimicking MYT1L haploinsufficiency found in patients [107, 108]. I assessed the transcriptional effects of MYT1L depletion using RNA-Seq early (week 1) and late (week 6) after induced neurogenesis. In line with the *Myt1l*-mutant mouse model, deregulated genes upon MYT1L depletion in human induced neurons were enriched for genes associated with epilepsy, schizophrenia and ASD (Figure 2.11 C).

Importantly, MYT1L depletion did not prevent the reprogramming of hESCs into induced neurons, which, upon MYT1L depletion, show gene deregulation that is linked to disease patterns observed in MYT1L syndrome patients [107, 108]. This suggests that our model is suitable to study MYT1L deficiency in a human system.

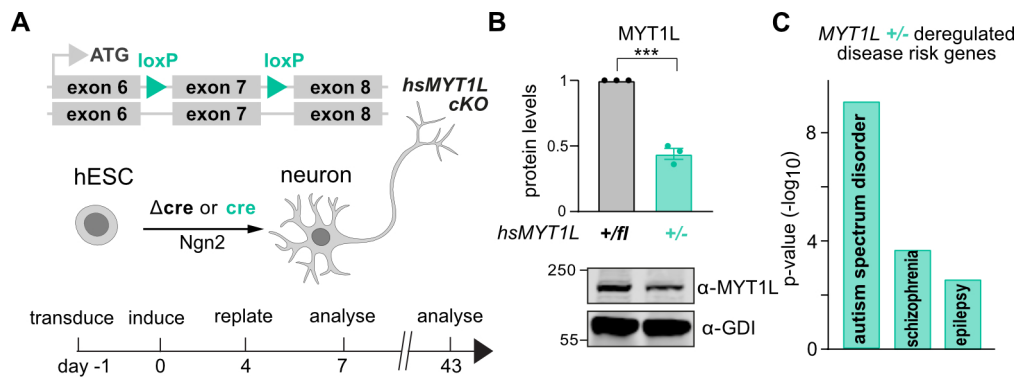


Figure 2.11: Engineered human embryonic stem cells can be used to model *MYT1L* deficiency in a human system. (A) Schematic of conditional heterozygous MYT1L deletion during transcription factor-mediated induced human neurogenesis. (B) Western blot quantification of cells 7 days (1 week) after induction of neurogenesis normalised to control. Representative Western blot images using indicated antibodies are shown. $n = 3$. Bar graph shows mean values with data points from individual biological replicates, error bars = SEM, unpaired t-test *** $p < 0.001$. (C) Deregulated genes in *MYT1L*-mutant neurons 43 days (6 weeks) after induction of neurogenesis exhibited significant overlap with genes linked to epilepsy (high confidence [142]), schizophrenia ([143]), and ASD ([144], score 1, accessed Dec2020) determined by Fisher's exact test. $n = 4$ for *MYT1L*^{+/+} (black) and *MYT1L*^{+/-} (teal), respectively. (Weigel et al., 2023)

As in the mouse model, several hundred genes were deregulated in *MYT1L*-deficient neurons compared to control early (week 1) and late (week 6) after induced neurogenesis. At both time points, but especially at week 6, MYT1L depletion resulted in a stronger up- than downregulation of genes in terms of number and magnitude (Figure 2.12 A, B). Importantly, the MYT1L DNA-binding motif (AAAGTT) was significantly enriched at genes upregulated upon MYT1L depletion one and six weeks after induced neurogenesis (Figure 2.12 C, D).

This suggests that MYT1L predominantly acts as transcriptional repressor in human induced neurons, which is in line with observations from the *Myt1l*-deficient mice (Figure 2.8 D) and the reported repressive role of MYT1L [116, 118, 120]

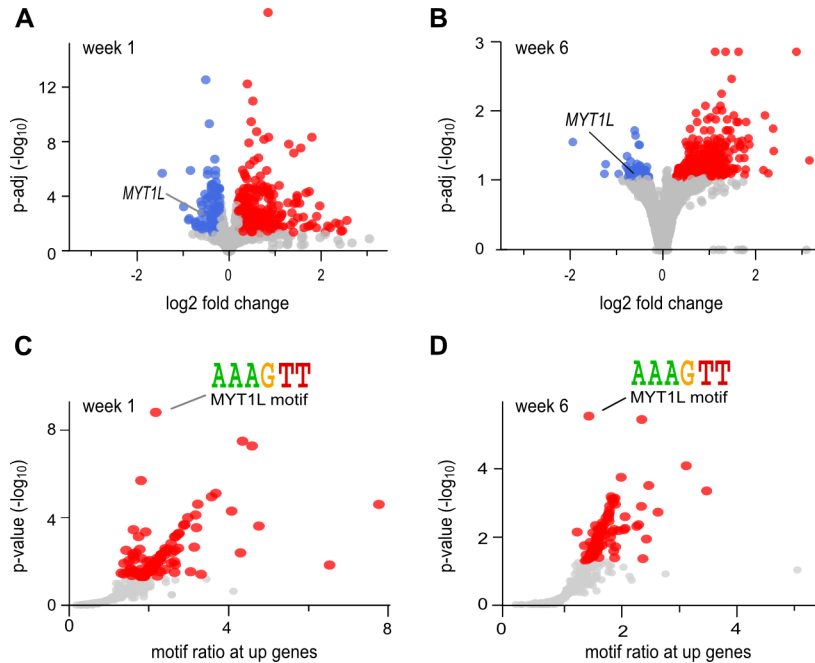


Figure 2.12: Predominant up-regulation of genes in *MYT1L*-deficient human induced neurons. (A, B) Volcano plot of differentially expressed genes in *MYT1L*-depleted human neurons after maturation for one week (A) or six weeks (B) compared to isogenic controls. Highlighted are genes that were down- (blue) or upregulated (red) upon *MYT1L* depletion with absolute \log_2 fold change > 0.2 and $p\text{-adj} < 0.1$. (C, D) The *MYT1L* DNA binding motif AAAGTT was significantly enriched at upregulated genes in panel A and B, respectively. $n = 4$ for *MYT1L*^{+/ β} and *MYT1L*^{+/-} at week 1 and week 6, respectively. (Weigel et al., 2023)

2.2.2 Enrichment of non-neuronal terms in *MYT1L*-deficient neurons

Previous results from *Myt1l*-deficient mice suggested that *Myt1l*-mutant cells fail to silence inappropriate gene expression programs, which results in a "confused" transcriptional identity in neurons *in vivo* (Figure 2.6, Figure 2.7 E).

I next wanted to examine whether this transcriptional "confusion" upon *MYT1L* depletion can also be seen in human neurons, which have been forced into a population of excitatory neurons by transcription factor-mediated induced neurogenesis. Ingenuity Pathway Analysis (IPA) showed that inappropriate developmental programs, such as myogenesis and cardiogenesis, were activated upon *MYT1L* depletion one and six weeks after induced neurogenesis for two independently-engineered *MYT1L*^{+/ β} clones (Figure 2.13 A). In line with data from the mouse model, GSEA revealed en-

richment of non-neuronal gene expression programs in *MYT1L*-deficient neurons early and late after induced neurogenesis (Figure 2.13 B).

These data demonstrate that *MYT1L* is important to repress non-neuronal gene expression programs, also in human induced neurons. Upregulation of these programs at early and late stages after induced neurogenesis suggests that they might usually be continuously repressed by *MYT1L*.

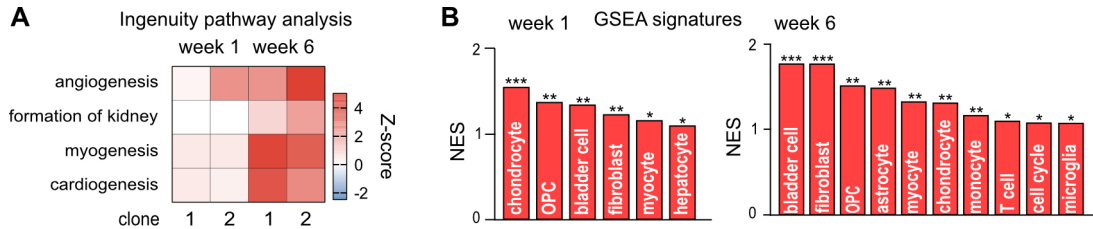


Figure 2.13: Upregulation of non-neuronal signatures upon *MYT1L* depletion in human induced neurons. **(A)** Ingenuity Pathway Analysis (IPA) of differentially-expressed genes in *MYT1L*-depleted human induced neurons showed activation of non-neuronal terms early (week 1) and late (week 6) after transcription factor-mediated induced human neurogenesis. The state of activation (red) or inhibition (blue) of a biological process is represented by a z-score (right-tailed Fisher’s exact test). Results are displayed for two independent clones. **(B)** Several non-neuronal signatures were increased (red) upon *MYT1L* depletion after transcription factor-mediated human neurogenesis after one and six weeks of differentiation based on Gene set enrichment analysis (GSEA). Shown are normalised enrichment scores (NES) of signatures with false discovery rate (FDR) ≤ 0.2 . FDR * < 0.2 , ** < 0.1 , *** < 0.01 . Panel B displays data for clone 1. Clone 1 $n = 4$ for week 1 and 6, clone 2 $n = 5$ for week 1 and 6 for *MYT1L*^{+/fl} and *MYT1L*^{-/-}, respectively. (Weigel et al., 2023)

2.2.3 Delayed neurogenesis in *MYT1L*-depleted human induced neurons

Apart from repressing non-neuronal gene expression programs, *MYT1L* has been reported to enhance direct reprogramming from mouse embryonic fibroblasts (MEF) into neurons by repressing direct target genes, such as members of the WNT and NOTCH signalling pathway [116]. I therefore checked the expression of such regulators upon *MYT1L* depletion in human induced neurons. I found that several negative regulators of neurogenesis were upregulated early (week 1) and late (week 6) after induced neurogenesis in *MYT1L*^{+/-} neurons from two independently-engineered clones (Figure 2.14 A). Interestingly, IPA for both clones showed that neuronal programs were decreased early but increased late after induced neurogenesis in *MYT1L*-depleted neurons compared to control (Figure 2.14 B), which indicates delayed neurogenesis upon *MYT1L* depletion. Indeed, I identified several pro-neuronal transcription factors that normally peak early during induced neurogenesis [156], which were downregulated in *MYT1L*-mutant neurons at week one, but upregulated at week six (Figure 2.14 C). These data suggest that due to failure to repress negative regulators of neurogenesis upon *MYT1L* depletion, induced neurogenesis is delayed in *MYT1L*-deficient human

neurons, which is in line with impaired neurogenesis, I observed in *Myt1l*-deficient mice.

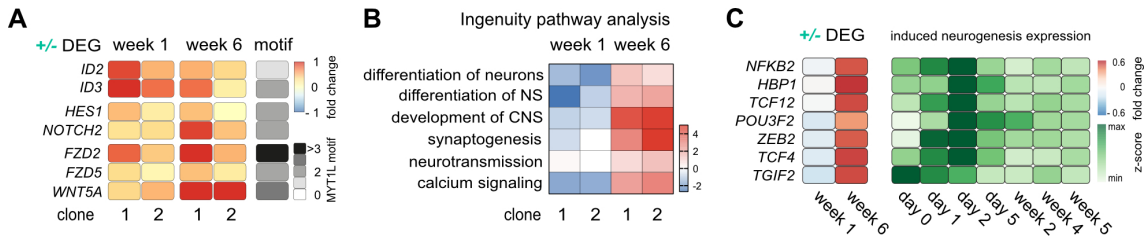


Figure 2.14: Gene upregulation and delayed neurogenesis in MYT1L-depleted human induced neurons. (A) Selected deregulated genes upon MYT1L depletion are displayed as fold change down- (blue) or upregulated (red) compared to isogenic control and number of MYT1L motifs in respective promoters is shown. Several negative regulators of neurogenesis are upregulated upon MYT1L depletion early (week 1) and late (week 6) after transcription factor-mediated induced human neurogenesis for two independent clones. (B) Ingenuity Pathway Analysis (IPA) shows early (week 1) inhibition but later (week 6) activation of neuronal terms in MYT1L-deficient human induced neurons compared to control. The state of activation (red) or inhibition (blue) of a biological function is represented by a z-score (right-tailed Fisher’s exact test). Results are displayed for two independent clones. (C) Examples of transcription factors that peak in expression early during induced neurogenesis based on published transcriptome data [156] displayed as z-score are initially (week 1) down and later (week 6) significantly upregulated during induced neurogenesis in MYT1L-mutant neurons, indicating delayed neurogenesis. Deregulation of gene expression based on RNA-Seq is displayed as fold change compared to control. Data in panel C is shown for clone 1. $n = 4$ (clone 1) or $n = 5$ (clone 2) for *MYT1L*^{+/*fl*} and *MYT1L*^{+/-}, respectively. (Weigel et al., 2023)

I next investigated whether chemical inhibition of the WNT and NOTCH signalling pathway could rescue transcriptional changes caused by MYT1L depletion and thereby normalise neuronal differentiation. To this end, human induced neurons were treated with NOTCH inhibitor (DAPT), WNT inhibitor (XAV939), or both for three days during induced neurogenesis and analysed after one week (Figure 2.15 A). Indeed, chemical pathway inhibition partially normalised gene expression changes in *MYT1L*-deficient neurons based on RNA-Seq analysis, particularly by decreasing expression of genes that are upregulated upon MYT1L depletion (Figure 2.15 B). I found that genes involved in WNT and NOTCH signalling, which were upregulated in *MYT1L*-deficient neurons, were downregulated upon chemical pathway inhibition (e.g. *NOTCH2* and *c-MYC*), while the opposite was the case for proneuronal factors (e.g. *NEUROD1*) (Figure 2.15 C).

Importantly, expression of the pro-neuronal transcription factors that normally peak early during induced neurogenesis and that were downregulated in *MYT1L*-mutant neurons at week one, but upregulated at week six (Figure 2.14 C) could be increased in MYT1L-deficient neurons by WNT and NOTCH inhibition early during induced neurogenesis (figure 2.15 D). This supports the hypothesis that these proneuronal factors are expressed later upon MYT1L loss due to higher

WNT and NOTCH signalling, causing impaired neurogenesis. Excitingly, combined application of chemical inhibitors targeting the WNT and NOTCH pathways even restored protein levels of the neuronal marker TUJ1, which was reduced in *MYT1L*-deficient neurons compared to control (Figure 2.15 E).

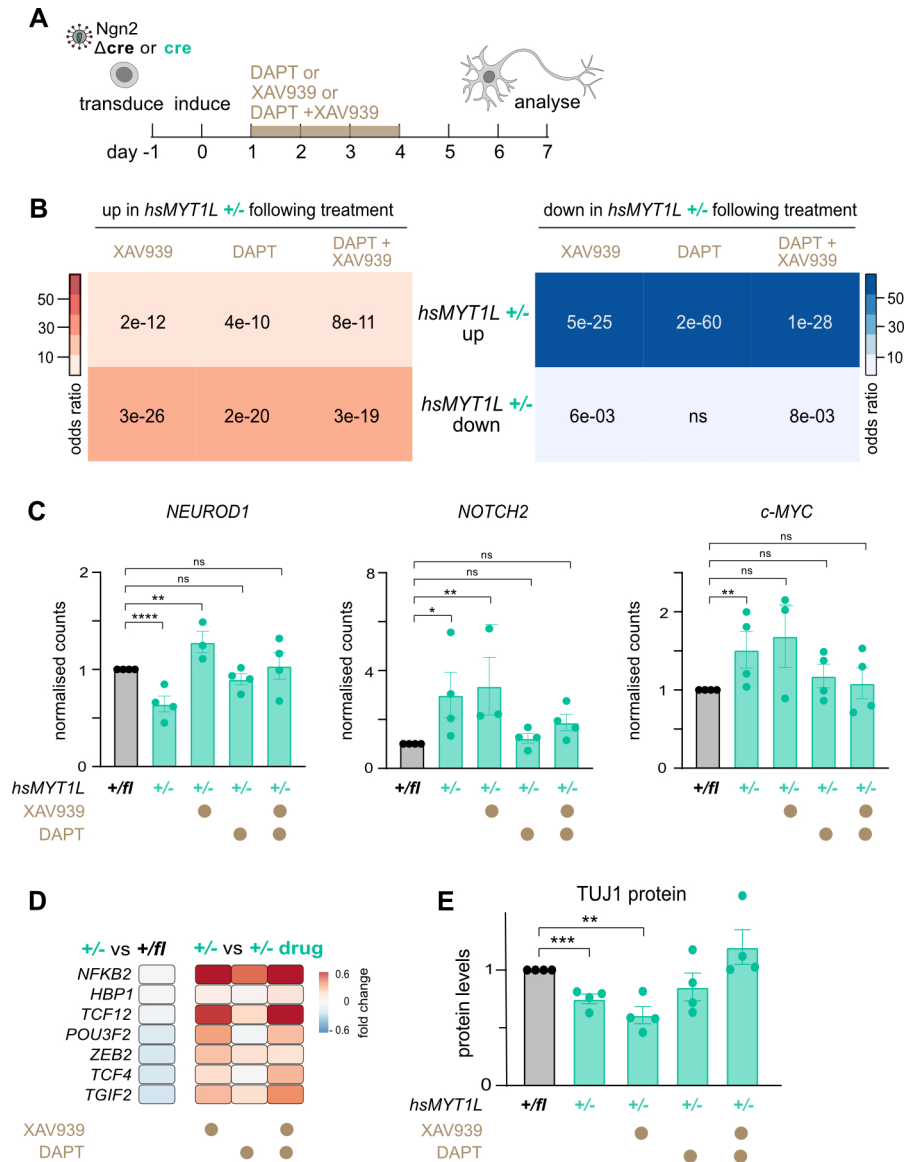


Figure 2.15: Partial rescue of transcriptional changes caused upon *MYT1L* depletion in human induced neurons by chemical inhibition of the WNT and NOTCH signalling pathway. **A**) Human neurons were treated with inhibitors of the WNT (XAV939) and NOTCH (DAPT) signalling pathway for three days during transcription factor-mediated induced human neurogenesis. (*Legend continued on next page*)

(B) Overlap of genes up- or downregulated upon MYT1L mutation in human induced neurons at day 7 with genes that are up- or downregulated in MYT1L-depleted neurons upon WNT and NOTCH inhibition via XAV939 and DAPT based on RNA-Seq and determined by GeneOverlap. $n = 8$ for $MYT1L^{+/fl}$ and $MYT1L^{+/-}$, respectively, $n = 4$ for $MYT1L^{+/-}$ + each inhibitor treatment, respectively. (C) Example genes with increased or reduced expression in MYT1L-depleted induced human neurons at day 7 that could be restored by inhibitor treatment. $n = 4$ for $MYT1L^{+/fl}$ and all $MYT1L^{+/-}$ samples. DESeq2 analysis * $p < 0.05$, ** $p < 0.01$, **** $p < 0.0001$, ns = not significant. (D) Transcription factors, which are down-regulated in $MYT1L^{+/-}$ neurons compared to $MYT1L^{+/fl}$ control early during development were upregulated upon WNT and NOTCH inhibition via XAV939 and DAPT. Deregulation of gene expression based on RNA-Seq is displayed as fold change compared to control. $n = 8$ for $MYT1L^{+/fl}$ and $MYT1L^{+/-}$, respectively, $n = 4$ for $MYT1L^{+/-}$ + each inhibitor treatment, respectively. (E) Reduced TUJ1 protein levels in MYT1L-depleted induced human neurons at day 7 can be restored by WNT and NOTCH inhibition via XAV939 and DAPT. $n = 4$. Bar graphs show mean values, data points from individual biological replicates are displayed, error bars = SEM, unpaired t-test in panel E, ** $p < 0.01$, *** $p < 0.001$. All data is from clone 1. (Weigel et al., 2023)

Together these data indicate that heterozygous deletion of MYT1L during human induced neurogenesis causes a delay in neurogenesis, which can, to some extent, be rescued by chemical inhibition of the WNT and NOTCH signalling pathway. This shows that impaired neurogenesis is, at least in part, mediated by increased expression of negative regulators of neurogenesis, such as WNT and NOTCH pathway members.

2.3 Functional assessment of MYT1L-depleted neurons

I have shown that MYT1L depletion causes gene deregulation resulting in several neurodevelopmental phenotypes in a mouse and human system. Since synaptic defects have been observed following mutation of gene regulators [102, 103], I next investigated whether and how the function of mature neurons is affected by MYT1L depletion. This is particularly interesting since MYT1L is expressed life-long and, in addition to its role during development, might also be continuously needed to ensure proper neuronal function.

2.3.1 MYT1L-deficient human neurons show network hyperactivity

For the multi-electrode array (MEA) technique, cells are seeded on culture dishes that have electrodes embedded in the culture surface. This technique enables detection of changes in the extracellular field potential and thereby measurement of network activity of electrically-active cells [157]. I used a multi-well MEA [158] to monitor the electrophysiological network activity of MYT1L-depleted and control neuronal cultures over time.

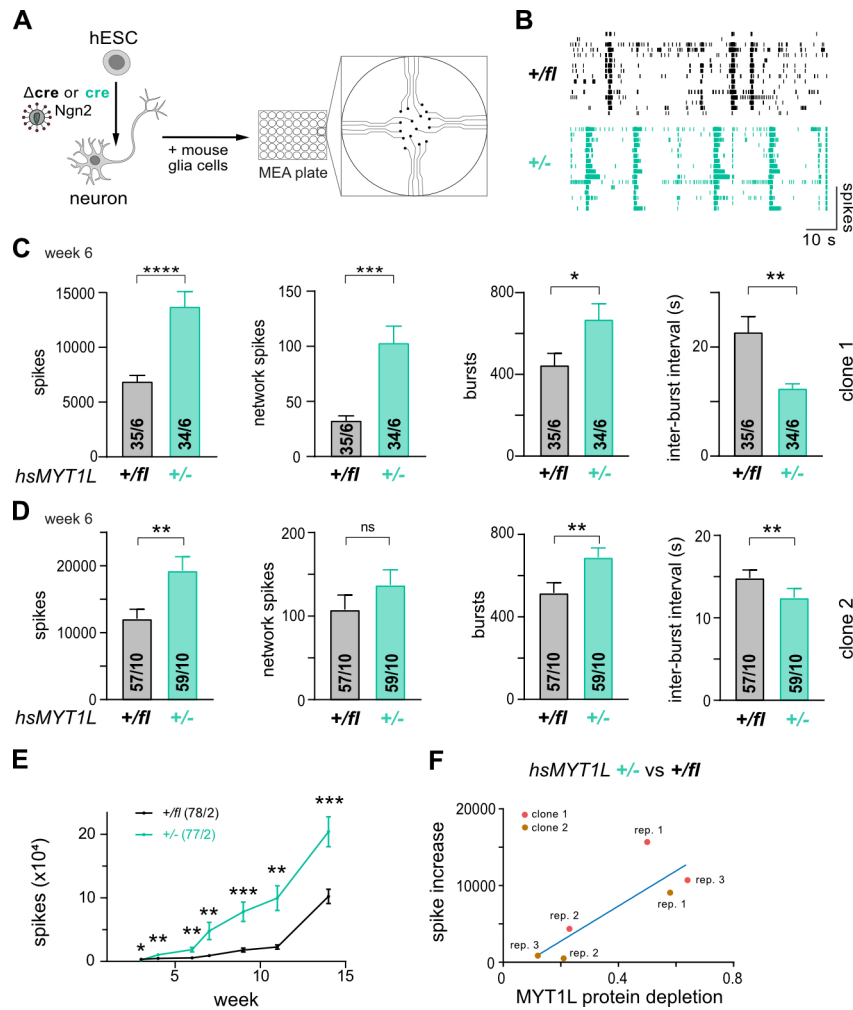


Figure 2.16: Electrophysiological network hyperactivity of MYT1L-deficient human induced neurons. (A) Human neurons were generated from embryonic stem cells by transcription factor-mediated induced neurogenesis and seeded with primary mouse glia cells on multi-electrode array (MEA) plates to monitor electrophysiological activity. (B) Representative MEA raster plots of $MYT1L^{+/fl}$ (black) and $MYT1L^{+/-}$ (teal) human induced neurons six weeks after induced neurogenesis. (C) Increased spontaneous neuronal network activity measured by MEA in $MYT1L^{+/-}$ neurons compared to $MYT1L^{+/+}$ control 6 weeks after induced neurogenesis. (D) Network hyperactivity on MEA could be reproduced with an independent clone 2. (E) Increased spike frequency of $MYT1L^{+/-}$ human induced neurons compared to control on MEA developed early during induced neurogenesis and did not normalise over time. Data from clone 1. (F) Inverse correlation of MYT1L protein levels and MEA hyperactivity. MYT1L depletion compared to control was determined by Western blot and plotted against the increase in spikes between depleted and isogenic control neurons for both clone 1 and 2. Effective heterozygous MYT1L depletion ($> 50\%$) caused by efficient cre-virus transduction resulted in increased number of spikes compared to less efficient transduction that resulted in incomplete ($< 50\%$) depletion. Bar graphs display mean values with number of MEA wells from indicated biological replicates, error bars = SEM, Mann-Whitney-test * $p < 0.05$, ** $p < 0.01$, *** $p < 0.001$, **** $p < 0.0001$, ns = not significant. (Weigel et al., 2023)

To this end, mutant and control human neurons were seeded together with mouse glia cells on MEA plates (Figure 2.16 A). Induced neurons matured on the plate and became electrically active (2.16 B). Unexpectedly, I observed a significantly higher network activity in *MYT1L*-deficient cultures compared to control six weeks after induced neurogenesis for two independently-engineered clones (Figure 2.16 B - D). This hyperactivity phenotype occurred approximately three weeks after induced neurogenesis and persisted over several weeks (Figure 2.16 E). Interestingly, activity of *MYT1L*-depleted neurons directly correlated with MYT1L protein depletion (Figure 2.16 F). These data show that MYT1L is important for normal function of human induced neurons.

2.3.2 Network hyperactivity upon MYT1L depletion is evolutionarily conserved

To investigate whether the functional phenotype in *MYT1L*-depleted human induced neurons can also be seen in primary mouse neurons, I prepared primary hippocampal cultures from *Myt1l*-deficient and control mice and seeded them on MEA plates (Figure 2.17 A). In line with the human phenotype, I observed significantly higher spike firing activity of *Myt1l*^{+/-} and *Myt1l*^{-/-} neurons compared to control (Figure 2.17 B, C). Also consistent with the human findings, the hyperactivity persisted over several weeks and scaled with the level of MYT1L protein depletion, with up to five-fold or seven-fold increased spiking frequency for *Myt1l*^{+/-} or *Myt1l*^{-/-} cultures, respectively (Figure 2.17 D). I could also reproduce the electrophysiological hyperactivity phenotype with primary neurons derived from cortices of *Myt1l*-deficient mice (Figure 2.17 E). This indicates that the defects are not restricted to neurons from specific brain regions, which is in accordance with the observation that MYT1L is expressed in virtually all neurons. However, since cortical cultures needed more time before they matured and showed synchronous electrophysiological activity and I saw more cell death in these cultures, I decided to proceed with primary hippocampal cultures for further analyses.

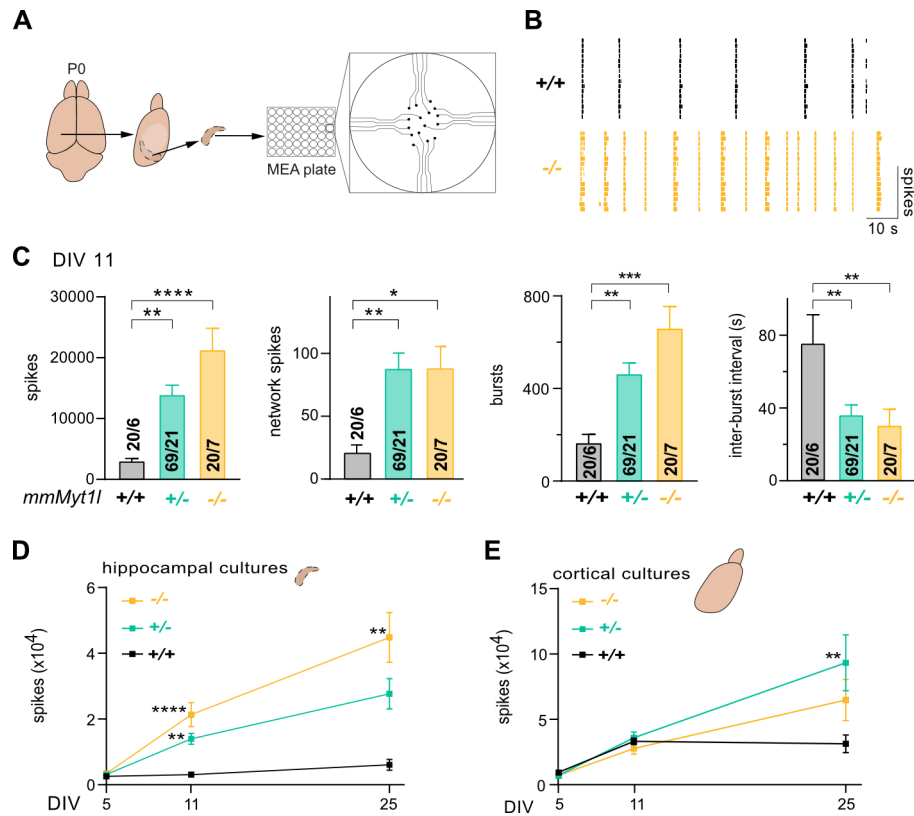


Figure 2.17: Electrophysiological network hyperactivity of MYT1L-depleted mouse primary cultures. (A) Primary hippocampal cultures from P0 mice were seeded on multi-electrode array (MEA) plates to monitor electrophysiological activity. (B) Representative MEA raster plots of *Myt1l*^{+/+} (black) and *Myt1l*^{-/-} (yellow) mouse primary hippocampal cultures on Day *in vitro* (DIV) 11. (C) Network hyperactivity measured by MEA for control *Myt1l*^{+/+} and mutant *Myt1l*^{+/-} (teal) and *Myt1l*^{-/-} hippocampal neurons in culture at DIV 11. (D) MEA-based functional analysis of cultured neurons over time showed that Compared to control, *Myt1l*^{+/-} and *Myt1l*^{-/-} neurons exhibited significantly increased spikes over several weeks *in vitro*. (E) Time-resolved MEA analysis of cortex-derived primary cultures recapitulated the network hyperactivity seen for *Myt1l*-mutant hippocampal cultures. Bar graphs display mean values with number of MEA wells from indicated biological replicates, error bars = SEM, One way ANOVA * p < 0.05, ** p < 0.01, *** p < 0.001, **** p < 0.0001. (Weigel et al., 2023)

We know that the *Myt1l* mutation in our mouse model results in production of an N-terminally-truncated MYT1L protein, which, based on overexpression experiments and immunostaining, did not enter the nucleus due to lack of the NLS and is thereby not expected to be functional (Figure 2.2). To rule out that the truncated cytoplasmic protein has a dominant negative effect on the functional properties of the mutant cells, I overexpressed the truncated isoform (aa 99 - 1187) or GFP control in primary hippocampal cultures from wild type mice. I confirmed overexpression by qRT-PCR (Figure 2.18 A). Importantly, I did not observe altered electrophysiological activity of cultures expressing the N-terminally-truncated protein compared to control (Figure 2.18 B).

This indicates that the truncated MYT1L isoform has no dominant negative effect, which further confirms that the *Myt1l*-mutant mouse is a suitable loss-of-function model.

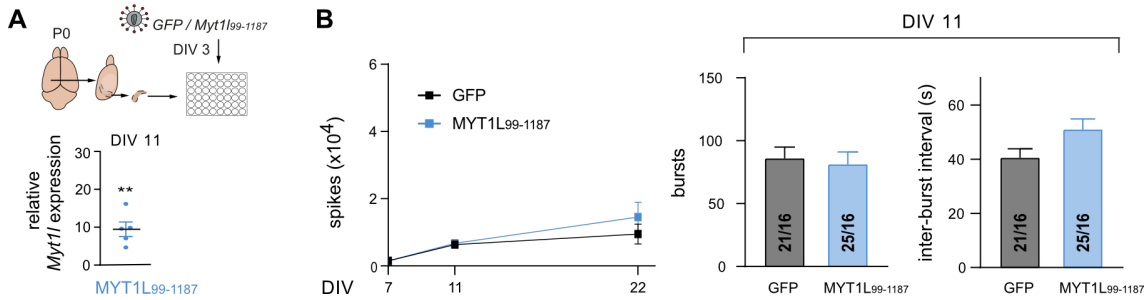


Figure 2.18: The N-terminally-truncated MYT1L protein does not have a dominant negative functional effect. (A) overexpression of N-terminally truncated (aa 99 - 1187) MYT1L at day in vitro 3 (DIV 3) in primary hippocampal cultures shown at DIV 11 by qRT-PCR as expression relative to GFP overexpression control. Scatter plot of biological replicates with the median is displayed. (B) Overexpression of N-terminally truncated (aa 99 - 1187) *Myt1l* (blue) did not result in electrophysiological hyperactivity on multi-electrode array (MEA) compared to control (black), indicating no dominant negative effect of the truncated protein. Bar graphs display mean values with number of MEA wells from indicated biological replicates, error bars = SEM, Mann-Whitney test ** $p < 0.01$. (Weigel et al., 2023)

The network activity measurements demonstrate that MYT1L depletion results in an unexpected network hyperactivity phenotype, which is similar in human induced and primary mouse neurons, suggesting a conserved functional role of MYT1L.

2.3.3 Synaptic hyperactivity in *Myt1l*-deficient cultures and brain slices

To correlate the observed network hyperactivity with synaptic activity of single cells, patch clamp recordings of cultured primary neurons, derived from the hippocampus of newborn mice, were performed (Figure 2.19 A). In accordance with the observed network hyperactivity on MEA, amplitude and frequency of spontaneous excitatory postsynaptic currents (sEPSCs) were higher in *Myt1l*-mutant neurons compared to control, indicating increased synaptic activity in *Myt1l*-mutant cultures (Figure 2.19 B). This trend persisted for miniature excitatory postsynaptic currents (mEPSCs) after adding tetrodotoxin (TTX) to the cultures but significance could only be reached for the frequency in *Myt1l*^{+/-} cultures (Figure 2.19 C).

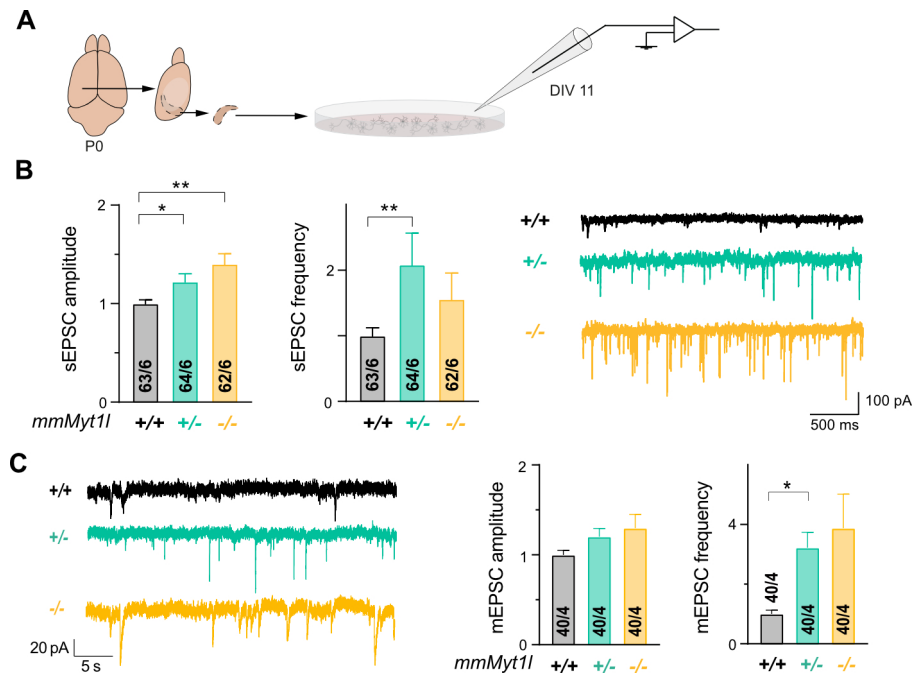


Figure 2.19: Increased synaptic activity of MYT1L-depleted primary hippocampal cultures. (A) Primary hippocampal cultures from P0 mice were prepared to use for patch clamp analysis at Day *in vitro* 11 (DIV 11). (B) Spontaneous excitatory postsynaptic currents (sEPSCs) were recorded at a holding potential of -70 mV for *Myt1l*^{+/+} control (black) and *Myt1l*^{+/-} (teal) and *Myt1l*^{-/-} (yellow) mutant neurons at DIV 11. Representative sEPSC traces and quantification of mean amplitude and frequency normalised to control are shown. (C) Miniature excitatory postsynaptic currents (mEPSCs) of primary hippocampal neurons were recorded at a holding potential of -70 mV in the presence of tetrodotoxin (TTX) for *Myt1l*^{+/+} control, *Myt1l*^{+/-} and *Myt1l*^{-/-} cells. Representative traces and quantification of mean amplitude and frequency normalised to control are shown. Bar graphs display mean values with number of cells from indicated biological replicates, error bars = SEM, One way ANOVA * $p < 0.05$, ** $p < 0.01$. (Weigel et al., 2023)

To validate these findings in a more physiological setting, electrophysiological brain slice recordings from pyramidal neurons located in the hippocampal CA1 region of one month-old *Myt1l*^{+/-} and control mice were performed (Figure 2.20 A). Consistent with the data from primary cultures, I observed an increased sEPSC frequency in *Myt1l*-deficient slices compared to control (Figure 2.20 B). Interestingly, the frequency of spontaneous inhibitory postsynaptic currents (sIPSCs) was also increased in *Myt1l*-deficient pyramidal neurons but the amplitude was slightly decreased (Figure (2.20 C). While the effect of MYT1L depletion on functional properties of inhibitory neurons needs further investigation, this data at least indicates that increased electrophysiological activity observed upon MYT1L depletion does not result from an increased excitation-inhibition ratio. Intrinsic functional properties, such as resting membrane potential and evoked action potential features, appeared unchanged between controls and mutants (Figure 2.20 D).

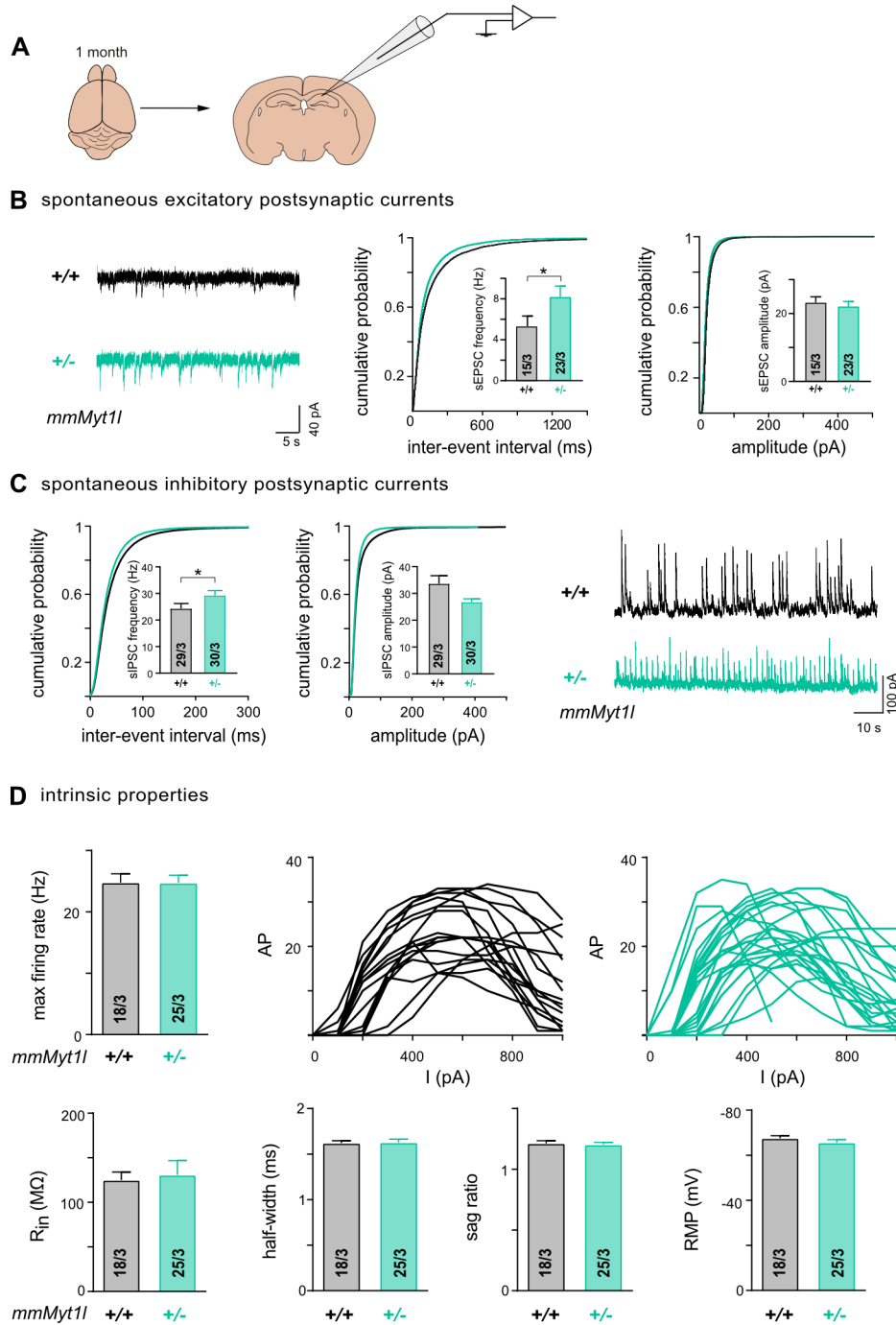


Figure 2.20: Increased synaptic activity in brain slices from *Myt1l*-deficient mice. **(A)** Acute brain slices from one-month old mice were prepared for patch clamp analysis of CA1 pyramidal neurons. **(B)** Increased spontaneous excitatory postsynaptic currents (sEPSCs) of *Myt1l*^{+/-} (teal) CA1 pyramidal neurons in acute mouse brain slices compared to *Myt1l*^{+/+} control (black). Representative traces, quantification and cumulative distributions are shown. **(C)** Increased spontaneous inhibitory postsynaptic current (sIPSC) frequency of *Myt1l*^{+/-} CA1 pyramidal neurons in acute mouse brain slices compared to *Myt1l*^{+/+} control. Representative traces, quantification and cumulative distributions are shown. **(D)** Electrophysiological characterisation of CA1 neurons in brain slices derived from one month-old *Myt1l*^{+/+} and *Myt1l*^{+/-} mice showed no difference in measured intrinsic properties of the cells (action potential (AP) firing upon current injection, input resistance (R_{in}), half-width, sag ratio and resting membrane potential (RMP)). bar graphs display mean values with number of patched cells from indicated biological replicates, error bars = SEM, Mann-Whitney-test * $p < 0.05$. (Weigel et al., 2023)

Taken together, functional analyses show that MYT1L depletion impairs neuronal function and results in an unexpected electrophysiological hyperactivity phenotype in human and mouse neurons in culture as well as in acute mouse brain slices, which indicates a conserved underlying molecular mechanism that may contribute to NDD-associated phenotypes observed in MYT1L syndrome patients [107, 108].

2.4 Towards therapeutic intervention for MYT1L syndrome

We know that MYT1L is expressed throughout life [110, 111] and I have presented data that suggests that MYT1L plays a role in the repression of non-neuronal gene expression programs in neurons. I therefore asked myself whether lack of non-neuronal gene repression upon MYT1L depletion causes the functional defects observed in MYT1L-depleted neurons and whether these defects can still be targeted after neurodevelopment is complete.

2.4.1 Post-mitotic MYT1L overexpression normalises spiking frequency of MYT1L-depleted neurons

I first investigated whether electrophysiological hyperactivity of *Myt1l*-deficient cultures can be normalised by overexpression of MYT1L in post-mitotic neurons. To this end, I prepared primary hippocampal cultures from *Myt1l*-depleted and control mice and transduced them with a *Myt1l* overexpression construct or GFP control at day in vitro (DIV) 3 (Figure 2.21 A). I confirmed MYT1L expression at DIV 11 using Western blot and qRT-PCR (Figure 2.21 B, C). Interestingly, expression of the neuronal marker *Tuj1* was also significantly increased upon *Myt1l* overexpression compared to GFP control (Figure 2.21 C). Strikingly, spiking frequency of *Myt1l*^{+/-} and *Myt1l*^{-/-} neurons could be reduced towards control by overexpression of *Myt1l* in these cells (Figure 2.21 D). These results demonstrate that transcriptional regulation of MYT1L is continuously needed to ensure normal neuronal function, which can even be restored by introducing MYT1L after neurodevelopment is complete in post-mitotic neurons.

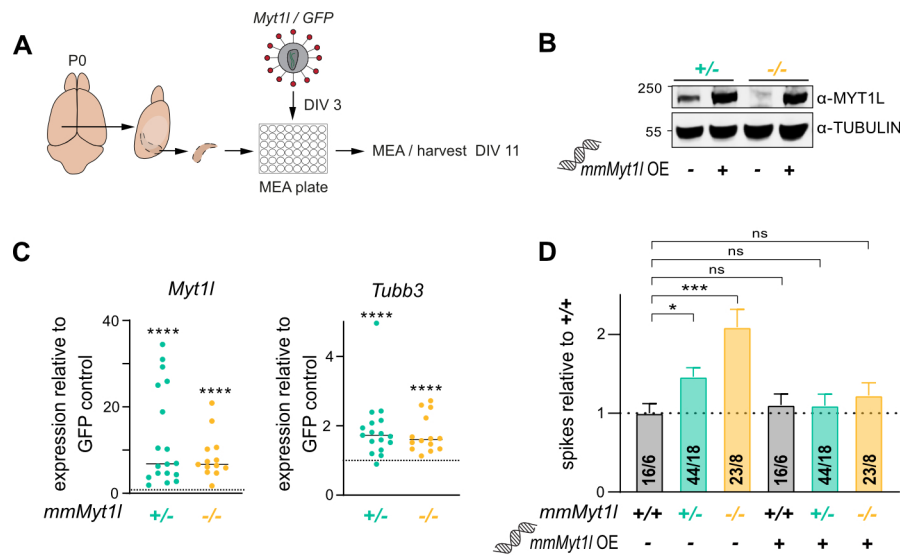


Figure 2.21: Post-mitotic MYT1L overexpression in *Myt1l*-depleted primary mouse cultures rescues electrophysiological hyperactivity. **(A)** Primary hippocampal cultures from P0 mice were prepared and transduced with a *Myt1l* or *GFP* overexpression construct at Day *in vitro* (DIV) 3 to monitor the effect of MYT1L in post-mitotic *Myt1l*-mutant and control neurons. **(B)** Representative Western blot images using indicated antibodies show overexpression of MYT1L in primary hippocampal *Myt1l*^{+/-} and *Myt1l*^{-/-} cultures at DIV 11 upon transduction as shown in panel A. **(C)** Overexpression of *Myt1l* in primary hippocampal cultures as shown in panel A resulted in up-regulation of *Tubb3* at DIV 11 determined by qRT-PCR as expression relative to GFP overexpression control. Graphs show scatter plots with the median displayed; $n \geq 13$. **(D)** Network hyperactivity of *Myt1l*^{+/-} (teal) and *Myt1l*^{-/-} (yellow) mouse primary neurons compared to control (black) can be rescued at DIV 11 by overexpression of MYT1L in post-mitotic neurons at DIV 3. Bar graphs display mean values with number of MEA wells from indicated biological replicates, error bars = SEM, Mann-Whitney test in panel C, Two-way ANOVA in panel D, * $p < 0.05$, *** $p < 0.001$, **** $p < 0.0001$, ns = not significant. (Weigel et al., 2023)

2.4.2 Knockdown of the main cardiac sodium channel *SCN5A* reduces spiking frequency

I next wanted to identify potential non-neuronal MYT1L targets that are deregulated upon MYT1L depletion and could explain the network hyperactivity phenotypes observed in MYT1L-depleted primary mouse and stem cell-derived human induced neurons.

To this end, I performed RNA-Seq for primary mouse (DIV 11) and human induced (week 6) cultures and created a list of genes that i) were bound by MYT1L *in vivo* based on CUT&RUN experiments (Figure 2.8 A - C); ii) were deregulated in primary mouse or human induced neurons upon heterozygous MYT1L deletion; iii) contributed to the activation of non-neuronal terms based on IPA (Figure 2.22 A); and iv) were lowly expressed on average (TPM < 2) in the brain compared to other tissues, based on public expression datasets (GTEx) [159]. Strikingly, 30 out of 38 of these

non-neuronal targets were upregulated upon MYT1L depletion in mouse and human neurons and among the top 10 upregulated genes, I found the main cardiac sodium channel *SCN5A* (Figure 2.22A). Deregulation of channels could alter electrophysiological properties in neurons and might thereby contribute to the observed phenotypes in MYT1L-deficient neurons.

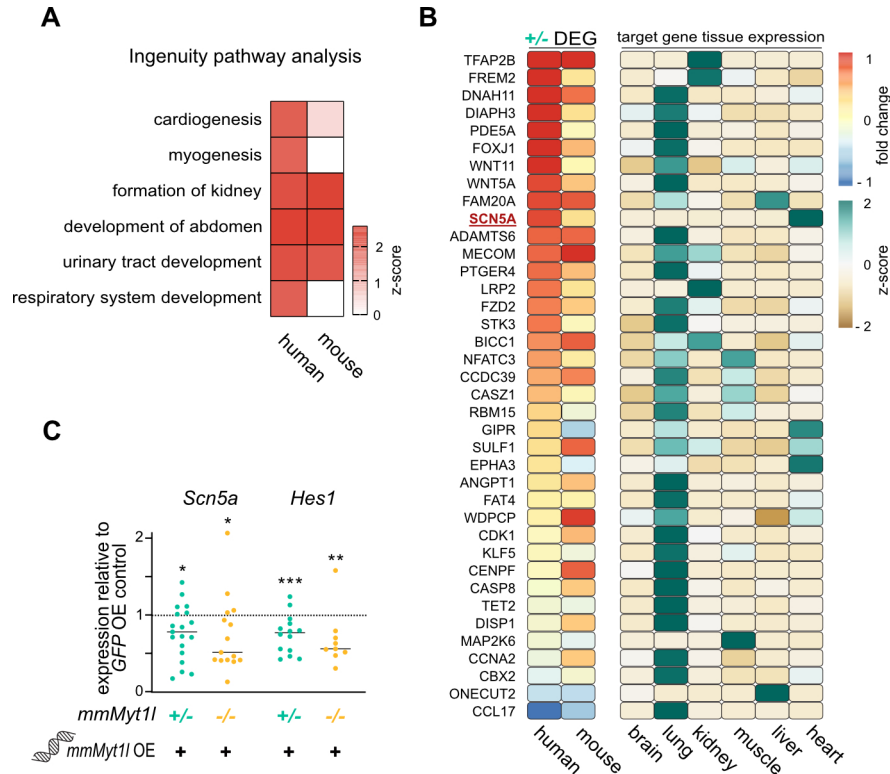


Figure 2.22: Up-regulated non-neuronal MYT1L target genes in human and mouse cultures include the main cardiac sodium channel *SCN5A*. (A) Ingenuity Pathway Analysis (IPA) of differentially-expressed genes in MYT1L-depleted human induced and mouse primary neurons showed overlapping activation of non-neuronal terms. The state of activation (red) or inhibition (blue) of a biological process is represented by a z-score (right-tailed Fisher's exact test). (B) Deregulated non-neuronal MYT1L target genes in MYT1L-deficient human neurons (week 6) and primary mouse neurons at day in vitro 11 (DIV 11) include the cardiac sodium channel *SCN5A*. Deregulation of gene expression based on RNA-Seq is displayed as fold change compared to control, $n = 4$ (human) for *MYT1L*^{+/fl} and *MYT1L*^{+/-}, $n = 3$ (mouse) for *Myt1l*^{+/+} and *Myt1l*^{+/-}, respectively. Tissue expression data from GTEx portal is displayed as z-score. (C) Significant downregulation of MYT1L target genes *Scn5a* and *Hes1* in MYT1L-deficient mouse primary hippocampal cultures at DIV 11 upon MYT1L overexpression at DIV 3 as shown in Figure 2.21A relative to GFP control determined by qRT-PCR. Graphs show column scatter plots with the median displayed; $n \geq 8$. Mann-Whitney test * $p < 0.05$, ** $p < 0.01$, *** $p < 0.001$. (Weigel et al., 2023)

Scn5a expression and other target genes (e.g. *Hes1*) that were upregulated in MYT1L-mutant neurons, could be reduced by overexpression of *Myt1l* in post-mitotic primary mouse neurons

(Figure 2.22 C). Since *Myt1l* overexpression also reduced the spiking frequency in *Myt1l*-deficient neurons (Figure 2.21 D), it is possible that upregulation of *Scn5a* upon MYT1L depletion, at least in part, contributes to the electrophysiological hyperactivity observed in MYT1L-depleted cultures.

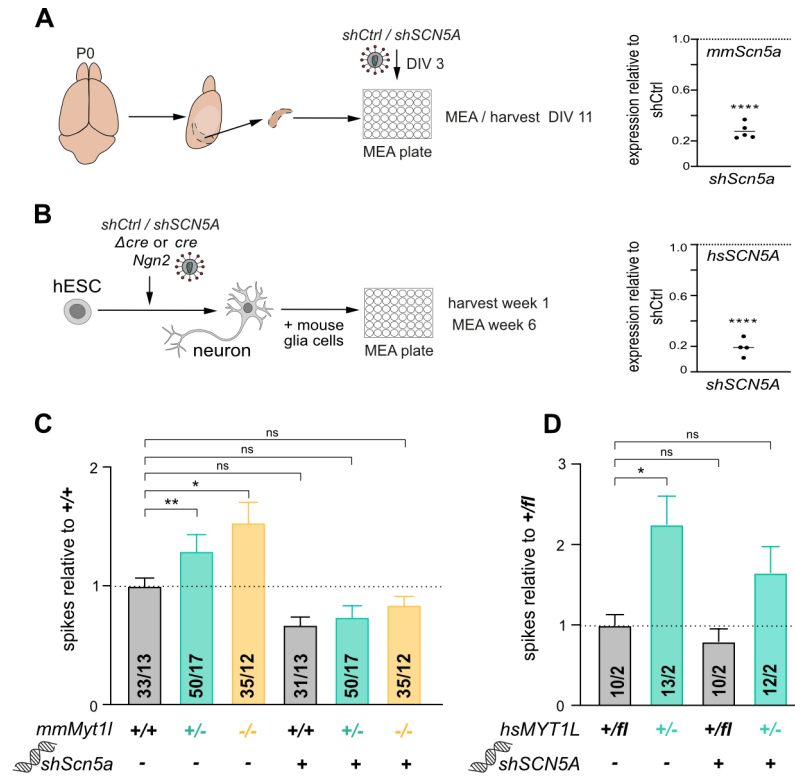


Figure 2.23: *SCN5A* knockdown rescues the hyperactivity phenotype in MYT1L-deficient mouse and human cultures. (A) Primary hippocampal cultures from P0 mice were seeded on multi-electrode array (MEA) plates and transduced with an shRNA construct targeting *Scn5a* or a non-targeting control at Day *in vitro* (DIV) 3 to monitor the effect of *Scn5a* knockdown in post-mitotic *Myt1l*-mutant and control neurons. *Scn5a* knockdown could be confirmed in primary hippocampal cultures at DIV 11 by qRT-PCR. (B) Human neurons were generated from embryonic stem cells by transcription factor-mediated induced neurogenesis. They were additionally transduced with an shRNA construct targeting *SCN5A* or a non-targeting control and seeded with primary mouse glia cells on MEA plates to monitor the effect of *SCN5A* knockdown in *MYT1L*^{+/fl} and *MYT1L*^{+/-} neurons. *SCN5A* knockdown could be confirmed in human induced neurons 6 weeks after induced neurogenesis by qRT-PCR. (C) Knockdown of *Scn5a* by shRNA expression in post-mitotic neurons at DIV 3 reduced spiking frequency of *Myt1l*^{+/-} (teal) and *Myt1l*^{-/-} (yellow) neurons towards control (black). (D) *SCN5A* knockdown with shRNA in human induced neurons resulted in reduced spiking frequency of *MYT1L*^{+/-} neurons. Bar graphs display mean values with number of MEA wells from indicated biological replicates, error bars = SEM, for qRT-PCR column scatter plots with the median are displayed, Mann-Whitney test in panel A-B, Two-way ANOVA in panel C-D, * p < 0.05, ** p < 0.01, **** p < 0.0001, ns not significant. (Weigel et al., 2023)

To test this hypothesis, I cloned shRNA constructs that reduced *SCN5A* RNA in primary mouse and human induced neurons (Figure 2.23 A, B). Strikingly, *Scn5a* knockdown normalised electrophysiological hyperactivity of *MYT1L*-depleted primary mouse neurons (Figure 2.23 C) and spiking frequency of *MYT1L*-depleted human induced neurons could also be reduced upon *SCN5A* knockdown (Figure 2.23 D).

These findings confirm the hypothesis that *MYT1L* is crucial to continuously repress non-neuronal genes, including the cardiac sodium channel *SCN5A*, which upon deregulation, at least in part, contributes to electrophysiological defects observed in *MYT1L*-depleted cultures.

2.4.3 Pharmacological intervention restores neuronal network activity and behaviour phenotypes

Based on the assumption that *MYT1L* depletion results in upregulation of the sodium channel *SCN5A*, which in turn causes electrophysiological defects, I decided to test whether application of lamotrigine, a sodium channel blocker and FDA-approved antiepileptic drug [160], could rescue *MYT1L* deficiency-induced phenotypes. I added 10 μ M lamotrigine to the culture medium of mouse and human cultures at DIV 11 and week 6, respectively, and measured electrophysiological activity on MEA before and 2 h after application of the drug (Figure 2.24 A). Similar to *Myt1l* overexpression (Figure 2.21 D) and *Scn5a* knockdown (Figure 2.23 C), lamotrigine treatment reduced spiking frequency of *Myt1l*-deficient primary mouse cultures towards control level (Figure 2.24 B). Application of lamotrigine to human induced neurons also normalised the network hyperactivity phenotype of *MYT1L*-depleted cultures (Figure 2.24 C).

This demonstrates that the use-dependent sodium channel blocker lamotrigine can rescue electrophysiological defects caused by *MYT1L* depletion in mouse and human neurons *in vitro*.

Next, I asked myself whether neuronal network hyperactivity upon *MYT1L* depletion contributes to the behavioural deficits observed in *Myt1l*-deficient mice and whether these can then also be treated with lamotrigine *in vivo*. To investigate this, I performed behavioural analysis one hour after I injected mice intraperitoneally with 20 mg/kg lamotrigine (Figure 2.24 D). Excitingly, I found that acute lamotrigine treatment of *Myt1l*-deficient mice normalised hyperactivity behaviour in the open field test and reduced locomotion and rearing in home cage observations (Figure 2.24 E, F).

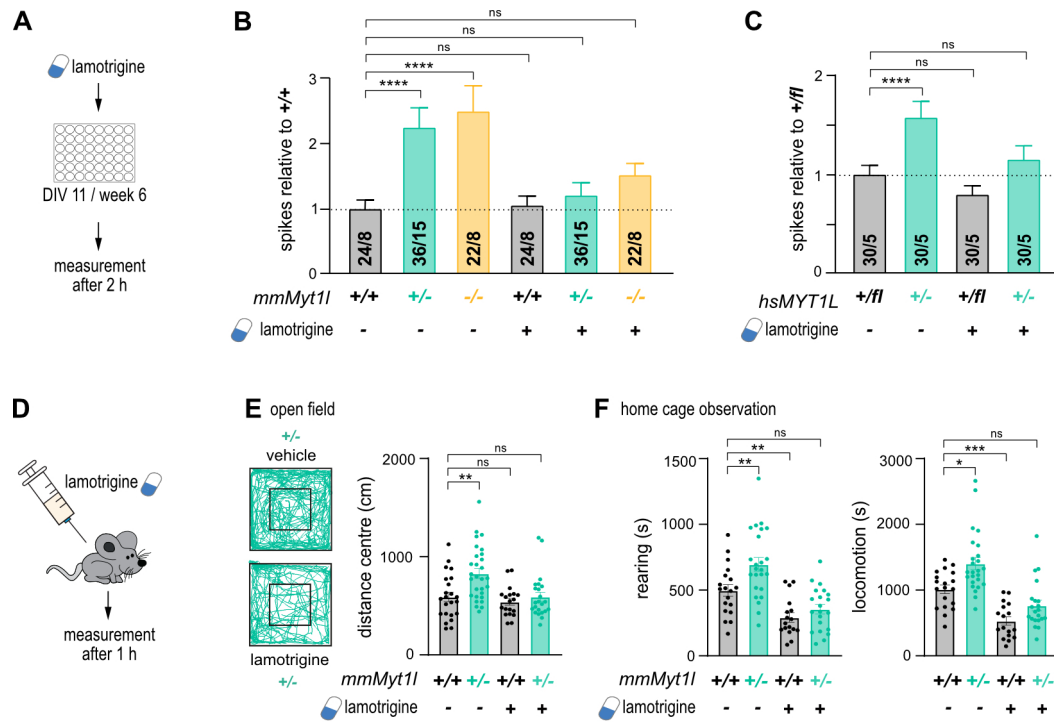


Figure 2.24: Application of the sodium channel blocker lamotrigine normalises electrophysiological activity of mouse and human neurons *in vitro* as well as mouse behaviour phenotypes *in vivo*. (A) Mouse primary hippocampal cultures and human induced neurons were seeded on multi-electrode array (MEA) plates and treated with the sodium channel blocker lamotrigine on Day in vitro (DIV) 11 (mouse) or week 6 (human). Electrophysiological activity was measured before and 2 h after treatment. (B) Network hyperactivity of *Myt1l*-deficient mouse primary neurons can be rescued by acute application of 10 μ M lamotrigine at DIV 11. (C) Increased spike firing upon MYT1L mutation was also normalised towards control by acute application of 10 μ M lamotrigine in induced human neurons six weeks after induced neurogenesis. (D) *Myt1l*-deficient and control mice were injected intraperitoneally with 20 mg/kg lamotrigine. Behaviour testing was performed 1 h after injection. (E) Open field tests showed that *Myt1l*^{+/-} mutants covered more distance in centre regions compared to *Myt1l*^{+/+} control animals at P23 and acute application of 20 mg/kg lamotrigine can normalise these hyperactivity phenotypes. Vehicle: n = 23 for *Myt1l*^{+/+} and n = 29 for *Myt1l*^{+/-}, lamotrigine: n = 19 for *Myt1l*^{+/+} and n = 23 for *Myt1l*^{+/-} with data from three independent cohorts. (F) LABORAS home cage observation showed significant increase in rearing and locomotion in *Myt1l*-mutant mice compared to control littermates. Acute application of 20 mg/kg lamotrigine can normalise this phenotype towards untreated control levels, while lamotrigine treated wild type mice also display decreased rearing and locomotion; vehicle: n = 19 for *Myt1l*^{+/+} and n = 25 for *Myt1l*^{+/-}, lamotrigine: n = 17 for *Myt1l*^{+/+} and n = 21 for *Myt1l*^{+/-} with data from three independent cohorts. Bar graphs display mean values with number of MEA wells from indicated biological replicates or data points from individual animals, error bars = SEM, Two-way ANOVA * p < 0.05, ** p < 0.01, *** p < 0.001, **** p < 0.0001, ns = not significant. (Weigel et al., 2023)

Overall, these results demonstrate that, besides neurodevelopmental defects, MYT1L depletion causes upregulation of non-neuronal genes and network hyperactivity in mouse and human neurons. Acute lamotrigine treatment rescued electrophysiological network hyperactivity in post-mitotic mouse and human neurons and behaviour phenotypes in mice, indicating that electrophysiological effects contribute, at least in part, to altered behaviour in mice. This suggests that targeted treatments may also benefit patients at later stages of development.

3 DISCUSSION

Researchers have spent decades gathering information that help us to better understand the complexity of our brain and the consequences of its malfunction. However, despite tremendous progress, the aetiology of most neuropsychiatric disorders remains enigmatic, making it very difficult to find targeted treatment options. It has long been thought that such disorders are mainly caused by mutations in genes involved in neuronal signal transmission [89, 90], but recent large genetic studies have revealed that transcriptional regulators are also frequently mutated in patients suffering from mental disorders [91], suggesting that gene deregulation is a central disease-causing mechanism. One of these regulators is the transcription factor MYT1L. *MYT1L* mutations are highly penetrant and, unlike most other candidates, it is specifically expressed in virtually all neurons and remains expressed throughout life [107, 110, 111]. The goal of this study was to examine how MYT1L mutations cause neurodevelopmental disorders, and to identify potential therapeutic treatment options.

I used stem cell-derived human neurons and mice, both harbouring engineered frameshift mutations, which are predicted to result in a premature STOP codon at aa 78 for mouse and aa 69 for human MYT1L, similar to a reported patient case with a nonsense mutation at aa 75 [128]. While I observed the expected reduction in MYT1L transcript and protein for *MYT1L*-mutant human induced neurons, the mutant mice showed no nonsense-mediated decay, but expressed two truncated isoforms, a C-terminally-truncated MYT1L protein terminating at the expected STOP codon at aa 78, and an N-terminally-truncated MYT1L protein, which was most likely produced from an internal methionine at aa 99. This observation emphasises the possible molecular differences between different mutations, human and mouse, as well as *in vitro* and *in vivo* models. Importantly, the N-terminally-truncated protein did not localise to the nucleus and hence did not exhibit detectable functions. Together with my observation that both models showed similar gene deregulation and functional defects, this suggests that, although the mutations in mouse and human triggered distinct molecular mechanisms in terms of mRNA surveillance and translation, they both ultimately resulted in a loss of function with overlapping phenotypes.

In both the mouse and human models, MYT1L deficiency caused significant deregulation of genes associated with disorders like epilepsy, schizophrenia, and ASD, NDDs which have all been diagnosed in patients carrying MYT1L mutations [107, 108]. I found a large overlap between genes found to be up- or downregulated in *Myt1l*-deficient mouse brains and ASD patients, which shows that MYT1L depletion might partially emulate ASD-associated transcriptional profiles. This deregulation of other NDD-risk genes has already been described, for example for the ASD-associated chromatin remodeler CHD8 [101], and supports the assumption that transcriptional regulation is important for the control of several risk genes, which might converge in regulatory networks associated with NDDs.

Previous *in vitro* mouse reprogramming studies have reported that MYT1L enhances neuronal cell fate by repressing negative regulators of neurogenesis, such as WNT and NOTCH pathway members, as well as non-neuronal gene programs [116, 145, 146]. However, other studies suggested that MYT1L can function as a transcriptional activator [117, 122]. This raises the question of whether the transcriptional activity of MYT1L might be context-dependent, which needs to be addressed in physiologically-relevant models. In this study, I evaluated the transcriptional role of MYT1L in mouse and human neurons *in vivo* and *in vitro*. I saw extensive transcriptional changes upon MYT1L depletion in mouse prefrontal cortex and human induced neurons, many of which seemed to be indirect since they did not overlap with MYT1L target genes determined by CUT&RUN. However, even though the cortex contains several non-neuronal cells that do not express *Myt1l*, the majority of differentially-expressed MYT1L targets were upregulated in bulk samples from the prefrontal cortex of homozygous *Myt1l*-depleted mice. Gene upregulation upon MYT1L depletion was even more pronounced in single-cell populations of neurons in the mouse cortex and pure populations of human induced neurons, supporting the idea that MYT1L predominantly acts as a transcriptional repressor in neurons.

Loss of the repressive activity of MYT1L resulted in the activation of various non-neuronal expression programs in mice and human induced neurons. I did not observe the emergence of unwanted cell types in the mouse brain, but I did find a "confused" transcriptional identity of neurons throughout development in mice and induced human neurons. This shows that MYT1L is important for silencing of inappropriate gene expression programs, which is in line with the previous description of MYT1L as a neuronal safeguard repressor [116].

Phenotypes observed in MYT1L syndrome patients include neurodevelopmental delays and altered brain anatomy. In line with this, I observed altered differentiation dynamics upon MYT1L depletion in human neurons and mice. Transcriptomic analysis revealed that, late in development,

expression of early developmental factors was increased in *MYT1L*-deficient human neurons upon transcription factor-mediated differentiation *in vitro* and in the prefrontal cortex of *Myt1l*-mutant mice *in vivo*. This indicates a delay in neurodevelopment, which has also been described in previous NDD models, e.g mouse models of ASD [92] and human iN models of schizophrenia [161] or lissencephaly [162]. Supporting these transcriptional changes and previous studies reporting impaired neurogenesis after shRNA-mediated *Myt1l* knockdown *in utero* [116], I saw impaired cell cycle exit of neural progenitors during cortex development, accompanied by an increased pool of SOX2+ neural stem cells and a thinner cortex comprised of NEUN+ cells at birth. Interestingly, these findings resemble the phenotypes observed in mice that overexpress the NOTCH target gene *Hes1* [163].

Importantly, I also observed upregulation of signalling pathway members, like WNT and NOTCH, that play a crucial role during neurogenesis. Deregulation of these instrumental pathways might explain the neurodevelopmental delays I observed in the mouse and human model. Indeed, chemical inhibition of WNT and NOTCH signalling pathways partially restored early expression of neurogenesis factors and induction of the neuronal marker protein TUJ1 in human induced neurons.

These findings show that MYT1L depletion results in destabilisation of neuronal cell identity, which manifests in NDD-associated gene expression changes and neurogenesis delays in mouse and human neurons. Given that MYT1L is expressed throughout life, it is tempting to speculate that MYT1L is important to continuously repress non-neuronal genes and thereby maintain neuronal cell identity. This is similar to the idea of terminal selectors, which continuously induce cell type-specific terminal differentiation genes [30]. Provided that MYT1L has a role as a life-long neuronal safeguard, it will be very interesting to investigate what happens if MYT1L was expressed in other cell types, or to study the effects of late MYT1L depletion in post-mitotic neurons. Indeed, reduced MYT1L expression and loss of neuronal cell identity has recently been suggested to play a role in Alzheimer's disease models [164, 165]. Together with the observation that *MYT1L* expression decreases during ageing [111], this suggests that life-long repression of non-neuronal genes in neurons could also play a role in the aetiology of neurodegenerative diseases.

Importantly, MYT1L depletion in mice resulted in behaviour phenotypes, such as hyperactivity, decreased anxiety and social deficits, which have been described in NDD patients and mouse models [107, 108, 150, 151]. While NDDs are often associated with repetitive behaviours [166], I observed a significant decrease in marble burying and grooming events, which model repetitive behaviour in mice. However, both marble burying and self-grooming are also considered to repre-

sent anxiety-like behaviours [167, 168], therefore making my observations consistent with decreased anxiety observed in other tests. Interestingly, all behavioural phenotypes could be observed independent of the sex of the mice, except for the social deficit phenotype, which was only found in males. Though no difference in sex distribution for patients carrying *MYT1L* mutations has been reported, ASD is noticeably more prevalent in males than in females [169] and various ASD mouse models describe male-specific behavioural deficits [170–174]. However, while theoretical models, such as the extreme male brain theory, begin to provide potential explanations [174–177], more experimental studies have to be performed in order to understand the causes of sex differences in NDDs. All in all, the behavioural data demonstrate that *Myt1l* depletion is sufficient to cause NDD-associated behaviours in mouse models.

A recent report from Wöhr and colleagues described developmental and behavioural phenotypes of mice with the same 7-bp *Myt1l* mutation in exon 6 [139]. In line with my findings, they did not see differences in the number of SOX2+ neural stem cells in the cortex of E15.5 *Myt1l*-mutant mice. However, they did not analyse newborn mice. While I saw significantly thinner cortices upon MYT1L depletion in newborn mice, they detected a trend in E18.5 mice, which pointed into the same direction. Behavioural phenotypes largely overlapped with my results, including increased ultrasonic vocalisation of pups, reduced anxiety and increased activity. They did not observe any social deficits in *Myt1l*-mutant mice. However, the social novelty test, which revealed male-specific deficits in my study, was not performed.

Two recently-published reports describe additional *Myt1l* mouse models with a frameshift mutation in exon 15 [121], by Chen and colleagues, or excision of exon 9 [138], by Kim and colleagues, respectively. Their behavioural studies contain different assays and developmental stages, but phenotypes in our model largely overlapped with their findings, including hyperactivity and male-specific social deficits. They also confirmed that MYT1L deletion results in post-natal death of homozygous *Myt1l* knockout mice and altered brain morphology, emphasising the crucial role of MYT1L in normal brain development. However, the three mouse models vary considerably in terms of gene expression and neurodevelopmental defects upon MYT1L depletion. While my data shows a decreased Q fraction at E15.5, no difference in the progenitor proliferation rate and an increased pool of neural stem cells at birth, Chen and colleagues report an increased Q fraction, slower proliferation rate, and fewer SOX2+ neural stem cells in *Myt1l*-deficient mice at E14.5. They suggest that increased neuron production early during development leads to progenitor pool exhaustion, resulting in thinner cortices. Additionally, they described a role for MYT1L as a transcriptional activator during early brain development, in contrast to my findings that MYT1L predominantly acts as a repressor throughout development. However, in a recent preprint, the same authors in-

licated that MYT1L represses genes involved in early neuronal developmental programs in adult mice [178], which is in line with my observation of increased expression of early neurodevelopmental gene signatures later in development in our *Myt1l*-deficient mice. Neither Chen nor Kim and colleagues confirmed the activation of non-neuronal signatures, which I observed in mice and human induced neurons upon MYT1L depletion. Notably, even though there was little overlap regarding gene deregulation in the different mouse models, all studies report a significant overlap of deregulated genes with NDD gene sets. Hence, while the differences between these *Myt1l* mouse models might reflect the distinct nature of mutations, genetic mouse background, and experimental conditions, all three models emphasise the important role of MYT1L in neurodevelopment and demonstrate that MYT1L loss can cause NDD-associated phenotypes. Excitingly, my study is the first to confirm these findings in human neurons.

In all models, the reported *Myt1l* mutations resulted in a loss-of-function phenotype. However, *MYT1L* syndrome patients have also been reported to carry *de novo* missense variants, and genomic duplications or deletions encompassing MYT1L [107, 108]. Since MYT1L patients display diverse phenotypes, including both macro- and microcephaly, and are diagnosed with different NDDs like ASD and schizophrenia, future studies will be needed to clarify how specific mutations or genetic backgrounds affect disease phenotypes.

Alongside gene expression changes and neurogenesis delays, I observed striking electrophysiological phenotypes in neurons upon MYT1L depletion. I used a multi-electrode array (MEA) system to monitor electrophysiological network activity of neuronal cultures over time. Despite deficits in neurodevelopment and a transcriptionally-destabilised neuronal identity upon MYT1L depletion, MYT1L-deficient primary mouse and human induced neurons showed an unexpected network hyperactivity on MEA. This phenotype persisted over time and was more severe in cultures with lower MYT1L protein levels. Network hyperactivity could be explained by multiple factors, such as changes in the number of synapses, an increased excitation-inhibition ratio, or general mechanisms regulating action potential firing and neurotransmitter release. Of note, *in vitro* models of several NDD risk genes, which are not directly involved in synaptic signal transmission, have shown changes in neuronal network activity, including hypo- [179] and hyperactivity [105, 180–183]. Interestingly, network hyperactivity was also observed in a human *in vitro* model of Alzheimer's disease [184].

In accordance with my MEA measurements, patch clamp analysis revealed an increased synaptic activity of *Myt1l*-deficient cells. In *Myt1l*-deficient primary mouse cultures, I saw an increased sEPSC amplitude and frequency, and an increased mEPSC frequency. The differences in frequency

were not significant for homozygous cultures, which could be due to the high cell to cell variability. However, the observation of the same trend towards higher activity for sEPSCs and mEPSCs upon MYT1L depletion points towards defects in synaptic transmission, either due to TTX-insensitive factors or due to changes at the post-synapse. The higher sEPSC frequency could be reproduced in a more physiological setting with CA1 pyramidal neurons in one month-old *Myt1l*-deficient mouse brain slices. I also observed an increased sIPSC frequency in these neurons, albeit with a slightly reduced amplitude, which might indicate only a slight increase or even unchanged overall inhibitory activity upon MYT1L depletion. Using three week-old *Myt1l*-deficient mice, Kim and colleagues also reported increased mEPSC frequency in pyramidal neurons of the medial prefrontal cortex, while Chen and colleagues only detected a trend towards increased mEPSC amplitude in layer 2/3 pyramidal neurons in the primary visual cortex. The latter also reported that the distribution of charge carried by individual postsynaptic current events shifted slightly toward increased excitation and decreased inhibition upon MYT1L depletion, resulting in an increased excitation-inhibition ratio, as often described in ASD models [185]. The discrepancy between this finding and my data might reflect differences in *Myt1l* mutations, experimental setup, and cell types used for patch clamp analysis.

In single cell RNA-seq experiments, I observed a slight increase in the fraction of cortical layer I neurons along with a decreased *Cdca7+* interneuron population in *Myt1l*^{-/-} mice, which might indicate an imbalance in excitatory and inhibitory signalling, and could be one potential cause for the post-natal death observed upon homozygous MYT1L deletion. However, patch clamp analysis of pyramidal neurons from *Myt1l*^{+/-} mouse brain slices revealed an increase in excitatory postsynaptic currents and no decrease in inhibitory postsynaptic currents. Since I observed striking network hyperactivity in *Myt1l*-deficient cultures of both genotypes, impaired inhibitory signalling due to an imbalance of cell type ratios is not likely to be the cause for increased network activity upon MYT1L depletion. This is supported by the observation that network hyperactivity was also detected for *NGN2*-induced neuronal cultures, which should mainly consist of excitatory neurons [152]. In any case, due to its pan-neuronal expression, it is likely that MYT1L is crucial for the function of both excitatory and inhibitory neurons. However, the effect of MYT1L mutations specifically on inhibitory neurons remains elusive and requires future studies.

Electrophysiological phenotypes might be a direct consequence of impaired neurogenesis and gene deregulation upon MYT1L depletion, or caused by compensatory effects upon continuous MYT1L depletion, since transcriptomic analysis showed initial down- and later upregulation of genes involved in synaptic transmission. Excitingly, MYT1L overexpression in post-mitotic *Myt1l*-deficient mouse neurons reduced spiking frequency on MEA, which indicates that neurodevelopmental de-

fects upon MYT1L depletion are most likely not the decisive factor causing electrophysiological phenotypes. However, after preparation of neuronal cultures from the hippocampus of mice, primary neurons start to develop axonal and dendritic structures *in vitro* [186], a process which is not completed after three days, when I overexpressed *Myt1l*. Hence, I cannot exclude that MYT1L depletion impairs neuronal maturation *in vitro*, which might in turn result in electrophysiological hyperactivity. Of note, Jana Tegethoff from our lab assessed neuronal morphology of cultured primary mouse and human induced neurons and did not observe any morphological defects upon MYT1L depletion. It will still be very interesting to investigate whether MYT1L can rescue electrophysiological phenotypes when overexpressed in mature neurons at later time points.

I saw striking overlapping phenotypes in mouse and human cultures, including upregulation of genes associated with non-neuronal cell fate signatures and electrophysiological hyperactivity. This suggests that expression of non-neuronal genes in neurons might be involved in the development of electrophysiological phenotypes. I identified several non-neuronal MYT1L target genes that were deregulated in MYT1L-depleted primary mouse and stem cell-derived human induced neurons. Among these mostly-upregulated genes, I found *SCN5A*, which encodes the alpha subunit of the main cardiac voltage-gated sodium channel $\text{Na}_v1.5$, showing an almost two-fold expression increase upon MYT1L depletion. Importantly, *Scn5a* expression was reduced in post-mitotic primary mouse cultures upon *Myt1l* overexpression, indicating that expression of this sodium channel indeed needs to be continuously repressed by MYT1L in neurons.

SCN5A is primarily expressed in cardiac muscle and plays a crucial role in regulating fast inward sodium currents, which are important for cardiac electrophysiological function [187, 188]. Mutations are associated with heart disease, such as long QT syndrome [189] or Brugada syndrome [190]. Recent studies have reported that, although at much lower levels compared to heart, different *SCN5A* splice isoforms are also expressed and have functional roles in the brain [191–198]. While the assessment of specific splice variants in MYT1L-deficient neurons requires further investigation, this shows that *SCN5A* expression changes functional properties of neurons, and misexpression, as observed in MYT1L-deficient mouse and human neurons, might cause electrophysiological deficits.

Excitingly, shRNA-mediated knockdown of *SCN5A* *in vitro* reduced spiking frequency of MYT1L primary mouse and human induced neurons, confirming that upregulation of this main cardiac sodium channel upon MYT1L depletion in neurons contributes, at least in part, to electrophysiological phenotypes. The increased mEPSC frequency observed upon MYT1L depletion in primary mouse cultures is in accordance with this hypothesis, since *SCN5A*, as a TTX-resistant sodium channel, is not blocked by low TTX concentrations, such as 0.5 μM . If upregulation of a voltage-

gated sodium channel was the reason for electrophysiological hyperactivity, I found it puzzling that intrinsic properties of MYT1L-depleted neurons seemed to be unchanged. However, Frenz and colleagues reported a unique physiological function of $\text{Na}_v1.5$ in olfactory receptor neurons, where it is localised to the dendritic endings, unlike other voltage-gated sodium channels, such as $\text{Na}_v1.7$, which is mainly distributed in the soma and axons. They found that most $\text{Na}_v1.5$ channels are unresponsive to activation at the resting membrane potential of the cell, and that they are not involved in upstroke and propagation of action potentials. However, they also showed that a small number of $\text{Na}_v1.5$ channels, which are not inactivated, can spontaneously open at a more negative membrane potential compared to other sodium channels and that these $\text{Na}_v1.5$ channels have a significant role in generating spontaneous activity [192]. These characteristics might explain the observations of spontaneous hyperactivity, but unchanged intrinsic properties upon *SCN5A* upregulation in MYT1L-depleted neurons. Despite this, the specific roles of $\text{Na}_v1.5$ in different mouse and human neuron subtypes and its significance in abnormal electrophysiological activities needs further investigation.

These observations open up the possibility of finding targeted treatment options for MYT1L syndrome patients, even though the disease is only diagnosed after neurodevelopmental defects have already occurred. I decided to test whether addition of the FDA-approved, use-dependent sodium channel blocker lamotrigine can normalise network hyperactivity in MYT1L-depleted cultures. Lamotrigine is already approved by the FDA for the treatment of epilepsy and other neurological disorders, including bipolar disorder [160, 199], which would ease the process of introducing it as potential treatment option for MYT1L syndrome patients. Indeed, acute application of lamotrigine normalised the spiking frequency of MYT1L-depleted primary mouse and human induced neurons. Finally, I injected mice with lamotrigine to test whether behavioural deficits observed in *Myt1l*-deficient mice could also be treated. Excitingly, lamotrigine treatment did normalise the less-anxious and hyperactive behaviour of *Myt1l*-depleted mice in open field and home cage tests, indicating that neuronal hyperactivity, at least in part, contributes to the behavioural phenotypes observed upon MYT1L depletion, and that these phenotypes can be treated at later stages of development *in vivo*.

4 CONCLUSION

In this study, I present evidence that MYT1L depletion is sufficient to cause phenotypes associated with neurodevelopmental disorders in a mouse and human model. I show that MYT1L acts as repressor of several non-neuronal genes in neurons and its depletion results in a "transcriptionally-confused" neuronal identity. Hence, failure to silence non-neuronal gene expression in neurons represents a novel mechanism, which might contribute to the aetiology of neurodevelopmental disorders.

Transcriptional deregulation results in neurodevelopmental defects and post-natal phenotypes, including electrophysiological hyperactivity of neurons and behaviour deficits in mice. MYT1L deficiency-associated phenotypes can be rescued in post-mitotic cells and adult mice, which emphasises the important role of MYT1L not only during development but also after neurogenesis. This makes MYT1L to stand out from many other NDD-associated gene regulators, which mainly act during neurodevelopment [200] and opens the possibility that therapeutic intervention can benefit patients with MYT1L syndrome even later in life.

One limitation of this study is that I only investigated the effect of MYT1L depletion on the aetiology of neurodevelopmental disorders. While several patients present with loss-of-function variants of MYT1L, also missense variants and duplications have been reported [107], which, given the broad range of phenotypes in *MYT1L* syndrome patients, could disrupt neuronal function in different ways. With modern technologies, we can engineer stem cells to carry patient-specific mutations or generate patient-derived neurons from induced pluripotent stem cells, which allows us to study how specific mutations or genetic backgrounds affect disease aetiology.

Another limitation of the human neuron model is that NGN2-mediated differentiation mainly results in the development of excitatory neurons. The phenotypes I observed in these cells resembled the ones from the mouse model but since MYT1L is expressed in all neurons, I cannot exclude that MYT1L depletion has different effects in other human neuron subtypes or that I missed important functions of human MYT1L by not studying the interplay of different brain cell types. In addition,

transcription factor-mediated differentiation does not fully reflect the physiological differentiation process, which might prevent us from capturing all differentiation defects upon MYT1L depletion. To investigate the differentiation process in the human system in more detail and analyse the interplay between different cell types, the dual-SMAD inhibition protocol, or even 3D brain organoids can be used.

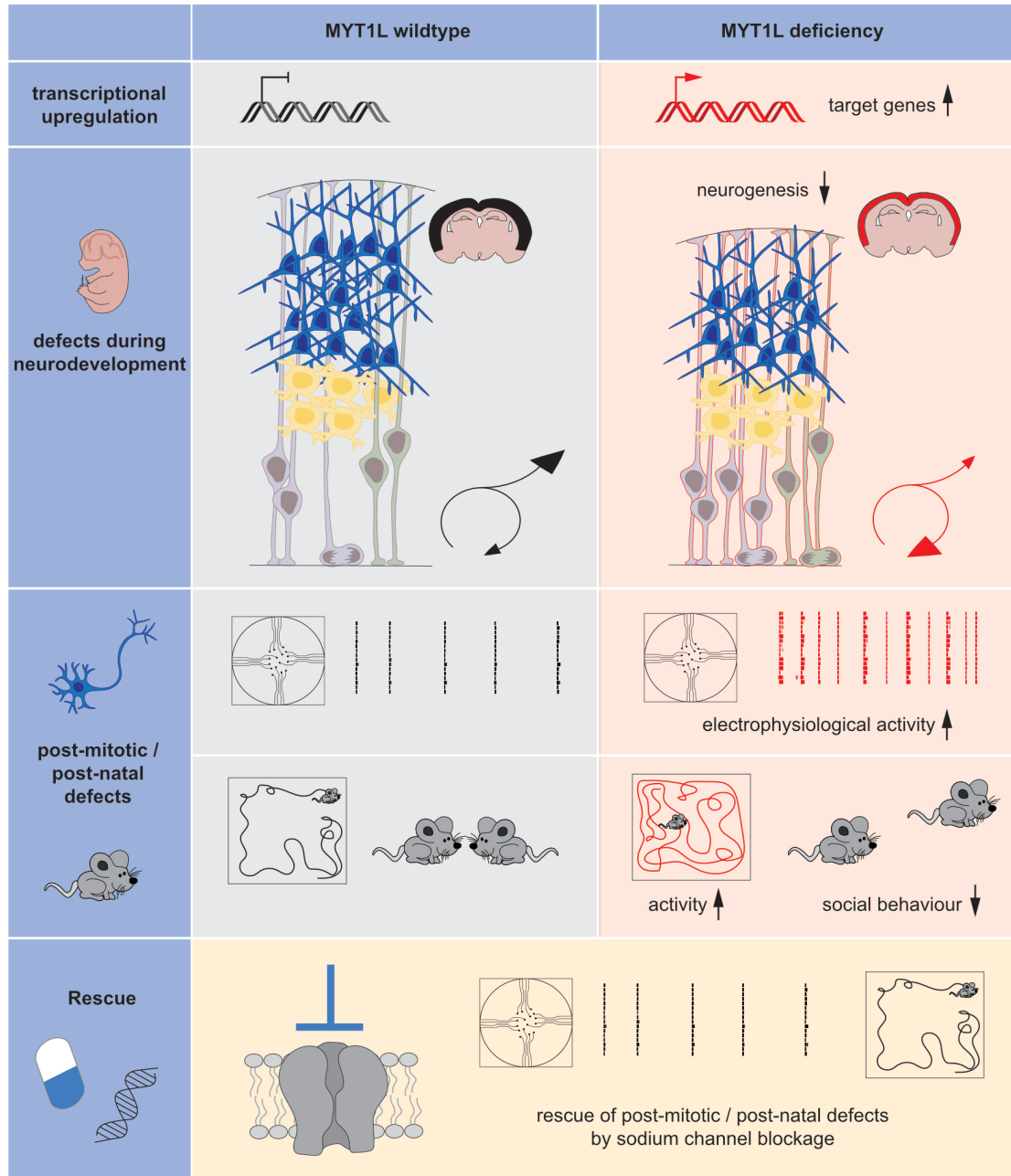


Figure 4.1: Graphical abstract of the main findings in this thesis. Transcriptional upregulation, developmental delays, electrophysiological hyperactivity and the respective rescue could be shown for mouse and human models.

The discovery of MYT1L as life-long safeguard of neuronal identity and its crucial role in preventing disease raises new questions that will be worth following up on in the future. For example, the question what happens if MYT1L was removed after completion of neurodevelopment in post-mitotic neurons, which will be very interesting in terms of aetiology of neurodegenerative disorders. It will also be exciting to see whether MYT1L has any effects when expressed in non-neuronal cell types. Lastly, it might be possible that transcription factors with similar safeguarding functions exist in other cells types and that this concept of silencing all-but-one cell fate signatures is a general mechanism often disrupted in disease.

5 MATERIALS AND METHODS

5.1 Materials

Cells

Cells	Origin	Culture medium
Human embryonic stem cells (ESCs), H1	WiCell (Madison, USA)	mTesR medium
HEK-293T cells	ATCC (Manassas, USA)	MEF medium
Primary mouse neurons	Prepped from P0 mice	Plating medium, Growth medium
SNL feeder cells	Merck (Darmstadt, Germany)	hES medium
Mouse glia cells	Prepped from P0 mice	MEF medium
Human iNs	Differentiation from ESCs	N2, B27, 2AraC medium

Cell culture reagents

Reagent	Supplier
Accutase	Thermo Fisher Scientific (Carlsbad, USA)
B-27 supplement	Thermo Fisher Scientific (Carlsbad, USA)
β -mercaptoethanol	Thermo Fisher Scientific (Carlsbad, USA)
Brain-derived neurotrophic factor (BDNF)	PeptoTech (Rocky Hill, USA)

Reagent	Supplier
bFGF	Thermo Fisher Scientific (Carlsbad, USA)
Cosmic calf serum (CCS)	Thermo Fisher Scientific (Carlsbad, USA)
Cytosine β -D-arabinofuranoside (Ara-C)	Merck (Darmstadt, Germany)
DAPT	Merck (Darmstadt, Germany)
Doxycycline	Merck (Darmstadt, Germany)
D-Glucose	Merck (Darmstadt, Germany)
EDTA (Ultra pure, 0.5M, pH 8.0)	Thermo Fisher Scientific (Carlsbad, USA)
Fetal Bovine Serum (FBS)	Merck (Darmstadt, Germany)
FuGENE	Promega (Madison, USA)
Geltrex	Thermo Fisher Scientific (Carlsbad, USA)
GlutaMAX	Thermo Fisher Scientific (Carlsbad, USA)
Hanks' Buffered Saline Solution (HBSS)	Thermo Fisher Scientific (Carlsbad, USA)
Knockout Serum	Thermo Fisher Scientific (Carlsbad, USA)
Lamotrigine	TargetMol (Massachusetts, USA)
Laminin mouse protein	Thermo Fisher Scientific (Carlsbad, USA)
L-Glutamine	Thermo Fisher Scientific (Carlsbad, USA)
Matrigel	Corning (New York, USA)
MEM-NEAA	Thermo Fisher Scientific (Carlsbad, USA)
Neomycin	Merck (Darmstadt, Germany)
N-2 supplement	Thermo Fisher Scientific (Carlsbad, USA)
Neurotrophin-3 (NT3)	PeptoTech (Rocky Hill, USA)
Papain	Merck (Darmstadt, Germany)
Phosphate Buffered Saline (PBS) (PBS)	Thermo Fisher Scientific (Carlsbad, USA)
Penicillin/ Streptomycin (Pen/Strep)	Thermo Fisher Scientific (Carlsbad, USA)
Polyethyleneimine (PEI)	Polysciences (Warrington, USA)
Poly-L-ornithine (PO)	Merck (Darmstadt, Germany)
Puromycin	Merck (Darmstadt, Germany)
Sodium pyruvate	Thermo Fisher Scientific (Carlsbad, USA)
Transferrin	Merck (Darmstadt, Germany)
Triton X-100Merck (Darmstadt, Germany)	
Trypan blue	Thermo Fisher Scientific (Carlsbad, USA)
Trypsin-EDTA, 0.25%	Thermo Fisher Scientific (Carlsbad, USA)
XAV939	Santa Cruz (Dallas, Texas)
Y27632 (ROCK inhibitor)	Axon MEDCHEM (Groningen, Netherlands)

Commercially available cell culture medium

Medium	Supplier
Dulbecco's Modified Eagle's medium (DMEM)	Thermo Fisher Scientific (Carlsbad, USA)
DMEM/F12 (L-Glutamine)	Thermo Fisher Scientific (Carlsbad, USA)
Minimum Essential Medium (MEM)	Thermo Fisher Scientific (Carlsbad, USA)
mTeSR medium	StemCell Technologies (Vancouver, Canada)
Neurobasal-A medium	Thermo Fisher Scientific (Carlsbad, USA)
Opti-MEM	Thermo Fisher Scientific (Carlsbad, USA)

Homemade cell culture medium

Medium	Composition
2-AraC medium	MEM supplemented with glucose (5 g/L), NaHCO ₃ (0.2 g/L), transferrin (100 mg/L), FBS (5%), B27 Supplement (1x), 0.5 mM L-glutamine, 2 μ M Ara-C
B27 medium	Neurobasal-A medium supplemented with GlutaMAX (1x), B27 Supplement (1x), BDNF (10 ng/mL), NT3 (10 ng/mL), mouse laminin (200 ng/mL)
Growth medium	Neurobasal-A medium supplemented with 5% FBS, B27 supplement (1x), 2 mM L-Glutamine
hES medium	DMEM-F12 supplemented with Knockout Serum (20% v/v), GlutaMAX (1x), penicillin-streptomycin (1x), MEM-NEAA (1x), sodium pyruvate (1 mM), β -mercaptoethanol (0.11 mM), bFGF (3 μ g/ μ L)
MEF medium	DMEM supplemented with GlutaMAX (1x), Pen/Strep(1x), MEM-NEAA (1x), sodium pyruvate (1mM), β -mercaptoethanol (0.1 mM)
N2 medium	DMEM-F12 supplemented with N2 supplement (1x), MEM-NEAA (1x), BDNF (10 ng/mL), mouse laminin (200 ng/mL), NT3 (10 ng/mL)
Plating medium	MEM supplemented with FBS (5%), B27 supplement (1x), glucose (0.4%), L-Glutamine (2 mM)

Molecular biology reagents

Reagent	Supplier
1 kb plus DNA ladder	Thermo Fisher Scientific (Carlsbad, USA)
Acetic acid	Honeywell (Charlotte, USA)
Agarose	Carl Roth (Karlsruhe, Germany)
Ampicillin	Merck (Darmstadt, Germany)
Antarctic Phosphatase	New England Biolabs (Ipswich, USA)
Antarctic Phosphatase Buffer	New England Biolabs (Ipswich, USA)
Antigen Retrieval Citra Plus Solution	BioGenex (Fremont, USA)
Benzonase	Merck (Darmstadt, Germany)
Bovine serum albumin (BSA)	Merck (Darmstadt, Germany)
Bromophenol blue sodium salt	Merck (Darmstadt, Germany)
Calcium chloride (CaCl ₂)	Carl Roth (Karlsruhe, Germany)
Concanavalin-A beads	Polysciences (Pennsylvania, USA)
CUTANA E. coli Spike-in DNA	Biocat (Heidelberg, Germany)
Cytocalasin B	Merck (Darmstadt, Germany)
DAPI	Thermo Fisher Scientific (Carlsbad, USA)
Digitonin	Merck (Darmstadt, Germany)
Dithiothreitol (DTT)	Merck (Darmstadt, Germany)
dNTP mix, 10 mM	Thermo Fisher Scientific (Carlsbad, USA)
EDTA	GERBU Biotechnik (Heidelberg, Germany)
EGTA	Merck (Darmstadt, Germany)
Ethanol absolute	VWR International (Radnor, USA)
Gel Loading Dye, Purple (6X)	New England Biolabs (Ipswich, USA)
Glacial Acetic Acid	Thermo Fisher Scientific (Carlsbad, USA)
Glycerol	Merck (Darmstadt, Germany)
Glycogen	Merck (Darmstadt, Germany)
HEPES, pH 7.2	Rockland (Pennsylvania, USA)
Hydrochloric acid (HCl)	Thermo Fisher Scientific (Carlsbad, USA)
Isopropanol	Merck (Darmstadt, Germany)
JM109 competent cells	Promega (Madison, USA)
LB Broth	Merck (Darmstadt, Germany)
LB-Agar Amp	Carl Roth (Karlsruhe, Germany)
LunaScript RT SuperMix	New England Biolabs (Ipswich, USA)

Reagent	Supplier
Methanol	VWR International (Radnor, USA)
Mangan(II)-chlorid (MnCl ₂)	Honeywell (Charlotte, USA)
NaF	Merck (Darmstadt, Germany)
NP-40/IGEPAL CA 630	Merck (Darmstadt, Germany)
Nuclease-free water	Qiagen (Hilden, Germany)
NuPAGE MOPS buffer (20x)	Thermo Fisher Scientific (Carlsbad, USA)
NuPAGE Transfer buffer (20x)	Thermo Fisher Scientific (Carlsbad, USA)
pAG-MNase	Protein Expression and Purification Core Facility EMBL (Heidelberg, Germany)
Restriction enzymes	New England Biolabs (Ipswich, USA))
PageRuler Plus Pre-stained Protein Ladder	Thermo Fisher Scientific (Carlsbad, USA)
Paraformaldehyd (PFA), 4%	Boster Biological Technology (Pleasanton, USA)
PBS pellets	Th. Geyer GmbH & Co. KG (Renningen, Germany)
PMSF	Merck (Darmstadt, Germany)
Potassium chloride (KCl)	Merck (Darmstadt, Germany)
Potassium hydroxide (KOH)	Merck (Darmstadt, Germany)
Power SYBR Green PCR Master Mix	Thermo Fisher Scientific (Carlsbad, USA)
Protease inhibitor	Merck (Darmstadt, Germany)
Protein A-coupled beads	Thermo Fisher Scientific (Carlsbad, USA)
QuickExtract DNA Extraction Solution	Lucigen (Middleton, USA)
Revert-700 total protein stain	LI-COR Biosciences (Lincoln, USA)
RNase A	Thermo Fisher Scientific (Carlsbad, USA)
Roti®-GelStain Red	Carl Roth (Karlsruhe, Germany)
Sodium dodecyl sulfat (SDS)	GERBU Biotechnik (Heidelberg, Germany)
Spermidine	MP Biomedicals (Eschwege, Germany)
Sodium bicarbonate (NaHCO ₃)	Santa Cruz Biotechnology (Dallas, USA)
Sodium chloride (NaCl)	Merck (Darmstadt, Germany)
Sodium hydroxide solution (NaOH)	Thermo Fisher Scientific (Carlsbad, USA)
Trisma base (Tris base)	Honeywell (Charlotte, USA)
Triton X-100	Merck (Darmstadt, Germany)
TRIzol	Thermo Fisher Scientific (Carlsbad, USA)

Reagent	Supplier
Tween-20	Merck (Darmstadt, Germany)
T4 DNA Ligase	New England Biolabs (Ipswich, USA))
T4 DNA Ligase Reaction Buffer	New England Biolabs (Ipswich, USA))
Vectashield mounting medium	Vectorlabs (Burlingame, USA)

In vivo substances

Substance	Supplier
EdU	Thermo Fisher Scientific (Carlsbad, USA)
Lamotrigine	Thermo Fisher Scientific (Carlsbad, USA)
Polyethylenglycol (PEG) 400	Thermo Fisher Scientific (Carlsbad, USA)

Buffer

Buffer	Composition
Antibody buffer (Cut&Run)	2 mM EDTA in Digitonin wash buffer
Binding buffer (Cut&Run)	20 mM HEPES-KOH pH 7.5, 10 mM KCl, 1 mM CaCl ₂ , 1 mM MnCl ₂ in water
Digitonin wash buffer (Cut&Run)	0.05% Digitonin (50mg/mL) in wash buffer
PBS-T	0.1% Tween-20 in PBS
RIPA buffer	150 mM NaCl, 50 mM Tris pH7.4, 1% Triton X-100, 0.5% DOC, 0.1% SDS, 1mM EDTA in deionized water
5xSDS sample buffer	250 mM tris pH 6.8, 50% (v/v) glycerol, 20% (w/v) SDS, 250 mM DTT, 0.1% (w/v) bromophenol blue in water
2xSTOP buffer (Cut&Run)	340 mM NaCl, 20 mM EDTA, 4 mM EGTA, 0.05% Digitonin, 0.5% RNase A (10mg/mL), 0.25% Glycogen (20 mg/mL), 1% CUTANA E.coli spike-in DNA in water
50xTAE buffer	2 M tris base, 50 mM EDTA pH 8.0, 5.75% (v/v) pure acetic acid in water

Buffer	Composition
Lysis buffer (IP)	0.5% Tween-20, 50 mM Tris pH 7.5, 2 mM EDTA, 1 mM DTT, 1 mM PMSF, 5 mM NaF, complete protease inhibitor in water
NP40 Lysis buffer (IP)	0.5% NP-40, 50 mM Tris pH 8, 150 mM NaCl, 2 mM EDTA, 1 mM DTT, 1 mM PMSF, 5 mM NaF, 5 µg/mL cytochalasin B, complete protease inhibitor, benzonase in water
Transfer buffer	20% methanol in 1x NuPAGE transfer buffer
Total protein stain reversal solution	0.1 M sodium hydroxide, 30% (v/v) methanol in water
Total protein stain wash solution	6.7% (v/v) glacial acetic acid, 30% (v/v) methanol in deionized water
Wash buffer (Cut&Run)	20 mM HEPES-KOH pH 7.5, 150 mM NaCl, 0.5 mM Spermidine, one tablet protease inhibitor in water

Antibodies

Primary antibody (host)	Supplier, catalogue number	Dilution
Alpha Tubulin (mouse)	Merck (Darmstadt, Germany), #T6074	1:10000 (WB)
Calnexin (rabbit)	Abcam (Cambridge, UK), ab133615	1:1000 (WB)
FLAG M2 (mouse)	Merck (Darmstadt, Germany), SLCJ4124	1:1000 (ICC)
GDI (rabbit)	Synaptic System (Goettingen, Germany), #130 011	1:1000 (WB)
KI67 (rabbit)	Abcam (Cambridge, UK), ab15580	1:500 (IHC)
MAP2 (rabbit)	Millipore (Massachusetts, USA), AB5622	1:1000 (ICC)
MYT1L (rabbit)	Millipore (Massachusetts, USA), #ABE2915, [116]	1:1000 (WB, IHC)
NeuN (guinea pig)	Synaptic System (Goettingen, Germany), #266 004	1:1000 IHC
SOX2 (mouse)	Santa Cruz Biotechnology (Dallas, USA), sc-365964	1:500 IHC
TBR2 (rabbit)	Abcam (Cambridge, UK), ab23345	1:500 IHC
TUJ1 (mouse)	BioLegends (San Diego, USA), #801202	1:1000 (WB)

Secondary antibody	Supplier	Dilution
Alexa Fluor 488 Goat anti-guinea pig	Thermo Fisher Scientific (Carlsbad, USA)	1:400 (IHC)
Alexa Fluor 555 Donkey anti-rabbit	Thermo Fisher Scientific (Carlsbad, USA)	1:400 (IHC), 1:2000 (ICC)
Alexa Fluor 488 Donkey anti-mouse	Thermo Fisher Scientific (Carlsbad, USA)	1:400 (IHC), 1:2000 (ICC)
IRDye anti-rabbit-800CW (donkey)	LI-COR Biosciences (Lincoln, USA)	1:10000 (WB)
IRDye anti-mouse-680RD (donkey)	LI-COR Biosciences (Lincoln, USA)	1:10000 (WB)

Commercially available kits

Kit	Supplier
Click-iT EdU Alexa Fluor 488 imaging kit	Thermo Fisher Scientific (Carlsbad, USA)
Direct-zol RNA MiniPrep	Zymo Research (Irvine, USA)
GenElute Plasmid Miniprep Kit	Macherey-Nagel (Düren, Germany)
NEBNext Ultra II DNA Library Prep Kit	New England Biolabs (Ipswich, USA)
NucleoSpin Gel and PCR Clean-up	Macherey-Nagel (Düren, Germany)
NucleoBond Xtra Midi Kit	Macherey-Nagel (Düren, Germany)
Phusion High-Fidelity PCR Kit	Thermo Fisher Scientific (Carlsbad, USA)
QiaPrep Spin Miniprep Kit	Qiagen (Hilden, Germany)

Plasmids

Plasmid	Insert	Source
pX330-hsMYT1L	hsMYT1L guide exon 6	this study
pFLIP-hsMyt1l	hsMyt1l exon 6 and 7 with exon 7 flanked by loxP sites followed by flp flanked PGK NEO cassette and an 3' Myt1l homology arm for targeting	this study

Plasmids

Plasmid	Insert	Source
pSicoR PGK puro	Puromycin	Addgene #12084
pCAGGS-flpE-puro	FlpE recombinase	Addgene #20733
pTet-O-Ngn2-puro	mmNgn2	Addgene #52047
pMDLg/pRRE	Gag and Pol	Addgene #12259
pRSV-Rev	Rev	Addgene #12259
pCMV-VSV-G	VSVG	Addgene #8454
FUW-M2rtTA	reverse tetracycline transactivator	Addgene #20342
FUW-GFP-Cre	Cre recombinase	[155]
FUW-GFP-dCre	truncated Cre recombinase	[155]
tetO-mmMyt1l	mmMyt1l	[116]
tetO-mmMyt1l _{aa99-1187}	mmMyt1l _{aa99-1187}	this study
tetO-GFP	GFP	[116]
FSW-rtTA	rtTA	this study
pSicoR Scn5a	shScn5a	this study
pSicoR SCN5A	shSCN5A	this study

shRNA oligonucleotides

Target	Sequence
control_fw	5' TCGAGAAAAAATCTCGCTTGGGCGAGAGTTCTCTTG AAACTCTCGCCAAGCGAGATA 3'
control_rev	5' TATCTCGCTTGGGCGAGAGTTTCAAGAGAACTCTCGC CCAAGCGAGATTTTTTTC 3'
Scn5a_fw	5' TGGACCAAGGTGAAAGTCAATTCAAGAGATTGACTTTC ACCTTGGTCCTTTTTTC 3'
Scn5a_rev	5' TCGAGAAAAAAGGACCAAGGTGAAAGTCAATCTCTTGA ATTGACTTTCACCTTGGTCCA 3'
SCN5A_fw	5' TGGGAATCCCTGGACCTTTATTCAAGAGATAAAGGTCCA GGGATTCCCTTTTTTC 3'
SCN5A_rev	5' TCGAGAAAAAAGGGAATCCCTGGACCTTTATCTCTTGA TAAAGGTCCAGGGATTCCCA 3'

*the destination vector pSico PGK GFP was kindly supplied by Dr. T. Jacks, Koch Institute for Integrative Cancer Research, MIT, USA

qPCR primers

Target	Sequence
mouse Hes1_fw	5' AAACCAAAGACGGCCTCTGA 3'
mouse Hes1_rev	5' GGAATGCCGGGAGCTATCTTT 3'
mouse Gapdh_fw	5' TATGATGACATCAAGAAGGTGG 3'
mouse Gapdh_rev	5' CATTGTCATACCAGGAAATGAG 3'
mouse Hes1_fw	5' AAACCAAAGACGGCCTCTGA 3'
mouse Hes1_rev	5' GGAATGCCGGGAGCTATCTTT 3'
mouse Gapdh_fw	5' TATGATGACATCAAGAAGGTGG 3'
mouse Gapdh_rev	5' CATTGTCATACCAGGAAATGAG 3'
mouse Myt1l_fw	5' GCACAGAAGCCTCTCTGGAT 3'
mouse Myt1l_rev	5' GAGGCCTGGTTGGATTTGGA 3'
mouse Map2_fw	5' TCACAGAAGGAGTGGGCCTT 3'
mouse Map2_rev	5' CTGAGGAACCTTAATTCTTGCCA 3'
mouse Scn5a_fw	5' AGACTTCCCTCCATCTCCAGATA 3'
mouse Scn5a_rev	5' TGTCACCTCCAGAGCTAGGAAG 3'
mouse Tubb3_fw	5' TTTTCGTCTCTAGCCGCGTG 3'
mouse Tubb3_rev	5' GATGACCTCCAGAACTTGGC 3'
human SCN5A_fw	5' GGAGGAGTCCAGCAAGCAG 3'
human SCN5A_rev	5' AACTGTCCTCTGGGGTCTCA 3'
human MAP2_fw	5' CAGGAGACAGAGATGAGAATTCC 3'
human MAP2_rev	5' CAGGAGTGATGGCAGTAGAC 3'

Genotyping primers

Target	Sequence
mouse Myt1l-WT_fw	5' CTCTGAGGAGAAGCGCCATCGCACC 3'
mouse Myt1l-WT_rev	5' CACTGGTACTCTTCTTCCACGGAAAATTACCC 3'
mouse Myt1l-KO_fw	5' CTGAGGAGAAGCGCCACGGTC 3'
mouse Myt1l-KO_rev	5' GGTGATGGGCCTCTGAGAGAC 3'
human 5' arm_fw	5' TCTACCCCATTATAGAGGACAAGG 3'
human 5' arm_rev	5' AAGGGTGGCATATAACTTCGT 3'

Target	Sequence
human 3' arm_fw	5' GACGTGCTACTTCCATTTGTCAC 3'
human 3' arm_rev	5' GGATTACACGGTGCCGCAG 3'
human loxP/wt_fw	5' GGTATGTCCGCGCTTCCCT 3'
human loxP/wt_rev	5' GCGACCCTCTTCCACAGAA 3'
human flp/wt_fw	5' CCGTGGAAACCAGCCATACAA 3'
human flp/wt_rev	5' TTTACGAGCAAGTCTCGGGG 3'
human neo_fw	5' GACGTGCTACTTCCATTTGTCAC 3'
human neo_rev	5' TTTACGAGCAAGTCTCGGGG 3'

Devices and Consumables

Device	Supplier
BioRad T100 Thermal Cycler	BioRad (Hercules, USA)
Cell Observer	Zeiss (Oberkochen, Germany)
Centrifuge S424	Eppendorf (Hamburg, Germany)
CM3050 S Cryostat	Leica (Oberkochen, Germany)
Countess cell counter	Thermo Fisher Scientific (Carlsbad, USA)
Contrast microscope BX51WI	Olympus-Lifescience (Tokyo, Japan)
DM IL LED Fluorescence Microscope	Leica (Oberkochen, Germany)
EASY-nLC™ 1200 System	Thermo Fisher Scientific (Carlsbad, USA)
EasyPhor gel electrophoresis chamber	Biozym (Hessisch Oldendorf, Germany)
Electrophoresis power supply	BioRad (Hercules, USA)
EPC 10 amplifier	HEKA (Lambrecht, Germany)
Fusion Orbitrap	Thermo Fisher Scientific (Carlsbad, USA)
GelDoc XR+ Molecular Imager	BioRad (Hercules, USA)
HERA cell 240i CO2 incubator	Thermo Fisher Scientific (Carlsbad, USA)
HR2 brain Slicer	Sigmann Elektronik (Hüffenhardt, Germany)
Maestro Pro	Axion Biosystems (Atlanta, USA)
Multiclamp 700B amplifier	Molecular Devices (San Jose, USA)
Mini Gel Tank	Thermo Fisher Scientific (Carlsbad, USA)

Device	Supplier
NanoDrop One	Thermo Fisher Scientific (Carlsbad, USA)
neoBlock 1 heatblock	neoLab (Heidelberg, Germany)
NextSeq 2000	Illumina (San Diego, USA)
NovaSeq 6000	Illumina (San Diego, USA)
ODYSSEY CLx Imaging System	LI-COR Biosciences (Lincoln, USA)
QuantStudio 5	Thermo Fisher Scientific (Carlsbad, USA)
Rotanta 460R centrifuge	Hettich (Kirchlengern, Germany)
TCS SP5 confocal microscope	Leica (Oberkochen, Germany)
Thermomixer compact	Eppendorf (Hamburg, Germany)
Vortexgenie 2	Scientific Industries (Bohemia, USA)

Material	Supplier
6-well tissue culture plates	Thermo Fisher Scientific (Carlsbad, USA)
12-well tissue culture plates	Corning Inc. (Corning, USA)
24-wel tissue culture plates	Corning Inc. (Corning, USA)
48-well tissue culture plates	Thermo Fisher Scientific (Carlsbad, USA)
384-well qPCR plate	Biozym (Hessisch Oldendorf, Germany)
Bacteria culture tubes	VWR International (Radnor, PA, USA)
Blotting (Whatman) paper	neoLab (Heidelberg, Germany)
Cell culture dish (10 cm)	Thermo Fisher Scientific (Carlsbad, USA)
Cell culture dish (15 cm)	Greiner Bio-One (Kremsmünster, Austria)
Cell lifters	Santa Cruz Biotechnology (Dallas, USA)
Conical centrifuge tubes (15 mL, 50 mL)	Corning (Corning, USA)
Countess Cell Counting Chamber Slides	Thermo Fisher Scientific (Carlsbad, USA)
MEA plates (48 wells)	Axion Biosystems (Atlanta, USA)
Microcentrifugation tubes (1.5 mL)	Thermo Fisher Scientific (Carlsbad, USA)
Microcentrifugation tubes (2.0 mL)	Eppendorf (Hamburg, Germany)
Millex syringe filters (45 µm)	Merck (Darmstadt, Germany)
Nitrocellulose membrane	Thermo Fisher Scientific (Carlsbad, USA)

Material	Supplier
NuPAGE 4-12% bis-tris gel	Thermo Fisher Scientific (Carlsbad, USA)
Parafilm	Merck (Darmstadt, Germany)
PCR tubes	Sigma-Aldrich/Merck (Darmstadt, Germany)
Petri dishes	Greiner Bio-One (Kremsmünster, Austria)
Pipette tips (10 μ L, 20 μ L, 200 μ L, 1000 μ L)	Mettler Toledo (Columbus, USA)
Pipette filter tips (10 μ L, 20 μ L, 200 μ L, 1000 μ L)	Starlab (Hamburg, Germany)
qPCR Seal Sheets	Biozym (Hessisch Oldendorf, Germany)
Roti® Liquid barrier marker	Carl Roth (Karlsruhe, Germany)
Serological pipettes (5 mL, 10 mL, 25 mL, 50 mL)	Greiner Bio-One (Kremsmünster, Austria)
Syringe (30 mL)	TH. Gyer (Renningen, Germany)
TissueTek® OCT™	Sakura Finetek (Umkirch, Germany)
X72 Superfrost plus slides	Thermo Fisher Scientific (Carlsbad, USA)

Software

Software	Supplier
Adobe Illustrator CC 2019	Adobe (San José, USA)
Affinity Designer (version 1.10.5)	Serif (West Bridgford, UK)
Avisoft-SASLab Pro	Avisoft Bioacoustics e.K. (Glienicke/Nordbahn, Germany)
AxisNavigator (version 3.5.1)	Axion Biosystems (Atlanta, USA)
Benchling	Benchling Inc. (San Francisco, CA, USA)
Fiji ImageJ (version 1.53t)	National Institutes of Health (Maryland, USA)
GraphPad Prism (version 8+9)	GraphPad Software (San Diego, USA)
IgorPro (version 6.3.7.2)	Wavemetrics (Tigard, USA)
Integrative Genomics Viewer (version 2.8.2)	Broad Institute of MIT and Harvard (Cambridge, USA)
Image Lab (version 5.2.1)	BioRad (Hercules, USA)
Image Studio Lite (version 5.2.5)	LI-COR Biosciences (Lincoln, USA)

Software	Supplier
LABORAS (Release 2.0)	Metris (Hoofddorp, Netherlands)
Leica Application Suite X (version 3.7.1.21655)	Leica (Wetzlar, Germany)
MATLAB	MathWorks (Natick, USA)
Maxquant software 2 (version 1.6.17.0)	Max-Planck Institute for Biochemistry (Martinsried, Germany)
Mendeley	Mendeley Ltd. (London, UK)
Microsoft Office	Microsoft Corporation (Redmond, USA)
Mini Analysis (version 6.0.3)	Synaptosoft (Fort Lee, USA)
Neural Metric Tool (version 2.4.12)	Axion Biosystems (Atlanta, USA)
Patchmaster 10 software	HEKA (Lambrecht, Germany)
QuantStudio-Design and Analysis software (version 1.3.1)	Thermo Fisher Scientific (Carlsbad, USA)
RStudio (version 4.0.2)	RStudio (Boston, USA)
SYGNIS TRACKER (version 4.1.14)	SYGNIS Bioscience (Heidelberg, Germany)
Zen 3.0 Software (black and blue edition)	Carl Zeiss Microscopy GmbH (Oberkochen, Germany)

5.2 Methods

Parts of the text in this Methods section have been taken or adapted from the manuscript entitled "MYT1L haploinsufficiency in human neurons and mice causes autism-associated phenotypes that can be reversed by genetic and pharmacologic intervention", which has been accepted for publication in Molecular Psychiatry and was originally co-written by myself (more details in the Contributions chapter).

5.2.1 Targeting and maintenance of human embryonic stem cells

The stable embryonic stem cell line was established by Moritz Mall prior to this study. H1 (male) human embryonic stem cells (ESCs) were maintained feeder-free in mTeSR Plus medium. To target *MYT1L*, H1 cells were transfected while seeding onto neomycin and puromycin-resistant SNL feeder cells with a plasmid containing CRISPR/Cas9 (pX330-hsMYT1L) and a guide (AGGA-GAAGCGGCATCGCACG) against *MYT1L* (ENSG00000186487) exon 6, together with a *MYT1L*-targeting construct (pFLIP-hsMYT1L) and a puromycin

resistance conferring plasmid (pSico-puro) using FuGENE 6. The *MYT1L*-targeting construct contained *MYT1L* exon 6 and 7 with exon 7 flanked by loxP sites, which resulted in a frameshift and a premature STOP codon upon cre-recombination. Additionally, the targeting construct included a neomycin-resistance gene flanked by *frt* sites and *MYT1L* homology arms to enhance homologous recombination upon CRISPR/Cas9-mediated mutagenesis. Puromycin (2 $\mu\text{g}/\text{mL}$) was added two days after transfection for two days to select transfected cells, followed by neomycin (300 $\mu\text{g}/\text{mL}$) addition for one week to select cells with stable expression of the targeting cassette. Resulting ES cell colonies were individually picked and expanded on feeder cells in human ESC medium. Correctly targeted colonies were confirmed by PCR screening and Sanger sequencing. To excise the integrated neomycin resistance, two clones from independent targeting experiments were selected and transfected while seeding onto puromycin-resistant feeder SNL feeder cells with a plasmid containing flippase (*flp-puro*) using FuGENE 6. Puromycin (2 $\mu\text{g}/\text{mL}$) was added two days after transfection for two days to select flippase-transfected cells, followed by expansion to pick individual subclones on feeder cells in human ES medium containing 10 μM Y-27632. Neomycin-cassette removal in targeted *MYT1L*^{+/*fl*} colonies was confirmed by PCR. Cre-recombination resulted in a 50% reduction in *MYT1L* protein levels in resulting human neurons. Cells were tested negative for mycoplasma contamination. Stem cell work was based on the German Stem Cell Act approved by the Robert Koch-Institute.

5.2.2 Generation of knockout mice

The genetically-engineered mice were generated by Moritz Mall at Stanford University and approved by the Institutional Animal Care and Use Committee prior to this study. To generate *Myt1l*-mutant mice, a guide RNA targeting *Myt1l* (ENSMUSG00000061911) exon 6 was loaded onto Cas9 protein and electroporated into C57BL6/N zygotes following published protocols [201]. Embryos were briefly cultured to confirm viability and then transferred to pseudo-pregnant surrogate mice for gestation. Offspring were screened for frameshift mutations in exon 6 using PCR followed by Sanger sequencing. Founders carrying a 7-bp frameshift mutation in exon 6 were bred with wild type (WT) C57BL/6N mice to confirm germline transmission. The 7-bp mutation in exon 6 of *Myt1l* is predicted to cause a frameshift at Amino acid (aa) 11 that terminates in a premature STOP codon at aa 79 in exon 9, similar to a reported patient case with a premature STOP at aa 75. F1 pups from the founder were genotyped by sequencing as above, then bred to generate experimental animals. Breeding was approved by the Regierungspräsidium in Karlsruhe (G-193/19).

5.2.3 Genotyping

For genotyping of the mice, the tip of the tail or earpunches were used. 50 μL QuickExtract was added to the sample, vortexed for 15 s and incubated for 6 min at 65°C. Subsequently, tubes were vortexed again and incubated for 2 min at 98°C. 1 μL of the extracted DNA was mixed with 3.8 μL nuclease-free water, 5 μL and 0.4 μL 10 μM Wild type (WT) or mutant allele-specific PCR primers. The PCR was performed using the following PCR conditions:

Step	Temperature	Time
1	95°C	5 min
2	95°C	30 s
3	59°C	30 s
4	72°C	20 s
		35 cycles
5	72°C	5 min
Pause	4°C	∞

1.5% agarose gels were prepared in 1x TAE buffer with 1:5,000 Gel Red Stain. After polymerization, samples and 1 kb DNA ladder were loaded and run at 150 V. Gels were imaged with the Geldoc system.

5.2.4 Immunoprecipitation

For each immunoprecipitation one hemisphere of P0 mice was flash-frozen in liquid nitrogen. The frozen tissue was lysed in 1 mL lysis buffer for 15 min at 4 °C. Nuclei were separated from debris by centrifugation at 3,200 rpm, 4 °C for 1 min and resuspended in 1 mL NP-40 lysis buffer. Debris was removed by centrifugation at 14,000 rpm, 4 °C for 10 min. Nuclear lysate was washed two times in 500 μL NP-40 lysis buffer and then pre-cleared by incubation with 15 μL uncoupled protein A beads for 1.5 h at 4°C. After centrifugation at 2000 rpm, 4°C for 1 min, the supernatant was incubated with 15 μL antibody-coupled beads for 1.5 h at 4 °C. After binding, the beads were washed seven times in NP-40 lysis buffer and bound proteins were eluted by incubation at 99°C for 5 min in SDS-PAGE sample buffer.

5.2.5 LC-MS/MS analysis

Peptides were resolved using the Easy NanoLC1200 fitted with a trapping (Acclaim Pepmap C18, 5 μm , 100 Å, 100 μm x 2cm) and an analytical column (nanoEase M/Z Peptide BEH C18 Column, 130Å, 1.7 μm , 75 μm X 250 mm). The outline of the analytical column was coupled directly to a Fusion Orbitrap (Thermo Fisher Scientific) mass spectrometer. Solvent A was 0.1% formic

acid (vol/vol) and solvent B 80% acetonitrile (vol/vol), 0.1% formic acid (vol/vol). The peptides were loaded on the trap column with a constant flow of solvent A at a maximum pressure of 800 bar. Peptides were eluted from the analytical column at a constant flow rate of 300 nl/min and a temperature of 55 °C. During the elution the percentage of solvent B was increased in a linear gradient from 3% to 8% in 4 minutes, then from 8% to 10% in 2 min, then from 10% to 32% for 68 min and then from 32% to 50% for another 12 min. At the end of the gradient solvent B was kept at 100% for 7 min followed by re-equilibration of the analytical column for 10 minutes at 97% solvent A. The peptides were introduced to the mass spectrometer via a Sharp Singularity Emitter 365 μm OD x 20 μm ID, length of 8 cm (Fossiliontech) and a nano-source spray voltage of 2 kV. The ion transfer tube temperature was set to 275 °C. Full scan MS1 spectra were acquired within the range (m/z) of 375-1500 in the Orbitrap detector with a resolution of 120000. The maximum injection time was set to 50 ms and automatic gain control target (AGC) to 1×10^6 ions. The most abundant ions within a 3 sec cycle time window were selected for fragmentation. Ions with unassigned charges and charges of 1 or >5 were excluded. Dynamic exclusion was set to 40 sec with a mass tolerance of ± 10 ppm. For the MS2 scans the quadrupole was used with an isolation window of 1.6 m/z. For peptide fragmentation higher-energy collisional dissociation (HCD) was used at 33%. MS2 scans were acquired in the linear ion trap that was operated in the rapid ion scan rate with an AGC target of 1×10^4 ions or a maximum injection of 50ms. MS2 scans were acquired as centroid data type.

For analysis, raw files were processed using Maxquant software 2 (version 1.6.17.0). The search was performed against the mouse Uniprot canonical database (downloaded 04/2019) containing only reviewed entries. Enzyme digestion in Maxquant settings was set to Trypsin allowing for maximum of up to 3 missed-cleavages. Protein N-term acetylation, methionine oxidation, deamidation (NQ) were set as variable modifications and carbamidomethylation of cysteine as a fixed modification. Minimum unique peptides option was set to 1. Match between runs was enabled by setting the match time window at 0.4 min. Both intensity-based absolute quantification and label free quantification values were calculated. Peptide and protein hits were filtered at a false discovery rate (FDR) of 1% with a minimal peptide length of 7 amino acids. The reversed sequences of the target database were used as a decoy database. Second peptide search for the identification of the chimeric MS2 spectra was enabled. All other Maxquant options were left to their default settings. Maxquant output tables were analysed with Microsoft Excel and R statistical software environment version 4.0.3.

5.2.6 Cloning

Plasmids were designed in Benchling. Vector plasmids were digested with suitable restriction enzymes for 2 h at 37°C and dephosphorylated for 10 min at 37°C using Antarctic Phosphatase before

heat inactivation for 20 min at 65°C. Inserts were amplified by PCR from the respective source plasmids using Phusion polymerase, mixed with 1x Phusion GC buffer, 200 μ Md NTPs, 0.5 μ M forward primer, 0.5 μ M reverse primer, 14% DMSO, 50 ng/ μ L template plasmid and nuclease-free water. The following PCR program was used.

Step	Temperature	Time
1	98°C	30 min
2	95°C	10 s
3	56°C	30 s
4	72°C	30 s per kbp 30 cycles
5	72°C	10 min
Pause	4°C	∞

Purification was performed using the NucleoSpin Gel and PCR Clean-up Kit. The PCR amplicon was digested the same way as the plasmid vector and both were recovered with a 1.5% agarose gel and extracted using the NucleoSpin Gel and PCR Clean-up Kit. For the inserts of the shRNA constructs, oligos were designed using the PSICOLIGOMAKER 1.5 (<http://web.mit.edu/ccr/labs/jacks/>). 10 μ M of the forward and reverse oligo were mixed with 1X T4 ligation buffer and 0.5 μ L T4 PNK and filled up with nuclease-free water to a final volume of 10 μ L. The mix was incubated for 30 min at 37°C (Phosphorylation), 5 min at 95°C and then ramped down to 25°C at 5°C/min (Annealing). Backbone and insert were ligated in a 1:4 molar ratio using the T4 ligase for 20 min at room temperature or overnight at 16°C. For transformation, JM109 competent cells were thawed on ice, 5 μ l of the ligated plasmid was added to 50 μ l of the cells and incubated for 20 min on ice. Heat shock was performed for 30 sec at 42°C followed by a 2-min incubation on ice. Next, 1 mL LB medium was added to the mix under sterile conditions and incubated for 1 h at 37°C (shaking at 750 rpm). Cells were centrifuged for 3 min at 3000 rpm, 900 μ L of the supernatant was removed and the cells were plated on a LB-ampicillin-agar plate for incubation at 37°C overnight. The next day, single colonies were transferred into 2 mL LB media containing ampicillin (100 μ g/ μ L) and incubated for a minimum of 24 h at 37°C. Plasmid DNA was extracted from 1 mL of the bacterial culture using the GenElute Plasmid Miniprep Kit. Isolated constructs were sent for Sanger sequencing (Genewiz). Remaining bacterial cultures correct plasmids were grown in 250 mL LB medium containing ampicillin (100 μ g/ μ l), shaken (250 rpm) overnight at 37°C and purified using the NucleoBond Xtra Midi Kit. Concentrations were determined using a Nanodrop spectrophotometer.

5.2.7 Virus production

Lentivirus was produced by transfection of lentiviral backbones containing the indicated transgenes together with third-generation packaging plasmids into HEK293 cells following the Trono laboratory protocol [202]. Virus was concentrated from culture supernatant by ultra-centrifugation (23000 rpm, 2 h, 4 °C) and either stored at -80° C or used directly for transduction.

5.2.8 Primary tissue dissection and cell culture

Mouse glial cells were isolated from forebrains of WT CD1 mice at P0, maintained in MEF medium and passaged twice before experiments. For primary neuronal cultures, the hippocampus or the cortex of P0 *Myt1l*-mutant or control mice were isolated and incubated in HBBS with 0.1% EDTA and 1.6% papain at 37°C for 20 min. The tissue was then washed twice with MEM, resuspended in the required volume of plating medium and plated on Matrigel-coated coverslips or PEI-Laminin-coated MEA plates. After one day, the plating medium was replaced with growth medium. Three days after plating, the medium was supplemented with 2 μ M Ara-C and half of the medium was changed every two days for the duration of the experiment. All cells were grown at 37 °C and 5% CO₂. For the genetic rescue, the cells were transduced with lentivirus encoding 1) targeting (shScn5a) or non-targeting control (shCtrl) shRNA 2) doxycycline-inducible *mmMyt1l* or *GFP* and *rtTA* under control of the Synapsin promoter on day in vitro 3 (DIV3). Doxycycline was added right before transduction on DIV3 for the MYT1L overexpression experiments.

5.2.9 Generation of human neurons

Human induced neurons (iNs) generation by transcription factor overexpression has been described previously [152]. In brief, on day -1 *MYT1L*^{+/F} human ESCs were treated with Accutase and plated on Matrigel-coated 6-well plates in mTeSR Plus containing 10 μ M Y-27632. While plating, lentivirus-encoding doxycycline-inducible *Ngn2* and either cre-recombinase or an inactive truncated Δ cre-recombinase, both under control of the ubiquitin promoter, were used to transduce the cells. For the genetic rescue, the cells were additionally transduced with lentivirus encoding targeting (shSCN5A) or non-targeting control (shCtrl) shRNA. On day 0, 2 mg/mL Doxycycline was added to induce *Ngn2* expression and retained in the medium until day 14. On day 1, cells were treated with Accutase and plated on Matrigel-coated 6-well plates in N2 medium containing 10 μ M Y-27632 and 2 μ g/mL Puromycin was added for three days to select for transduced cells. On day 4, neuronal cells were treated with Accutase and replated in B27 medium. For day 7 harvest, neuronal cells were seeded on Matrigel-coated 12-well plates without addition of glia cells. WNT and NOTCH inhibition was performed by supplementing the media from day 1 to day 4 with either 10 μ M N-[N-(3,5-difluorophenacetyl)-l-alanyl]-S-phenylglycine t-butyl ester (DAPT), 15 μ M

Tetrahydro-2-[4-(trifluoromethyl)phenyl]-4H-thiopyrano[4,3-d]pyrimidin (XAV939), or both. For functional maturation, neuronal cells were seeded on Matrigel-coated coverslips or PEI-Laminin-coated MEA plates together with primary mouse glia cells with media changes every 2 days. After one week, the medium was gradually exchanged with 2Ara-C medium, with medium changes every 3–4 days for the duration of the experiment. All cells were grown at 37 °C and 5% CO₂.

5.2.10 Immunocytochemistry

Cells were washed once with PBS and fixed using 4% PFA in PBS for 10 min. Cells were then permeabilised in 0.25% Triton X-100 in PBS for 10 min, blocked in a solution of PBS containing 5% normal goat serum for 1 h, followed by incubation with primary antibody diluted in PBS containing 2.5% normal goat serum overnight at 4 °C. Cells were washed three times in PBS containing 2.5% normal goat serum prior to incubation for 1 h at RT with secondary antibodies. Next, cells were washed 3 times in PBS containing 2.5% normal goat serum and incubated for 5 min with 100 ng/mL DAPI. Finally, cells were washed with deionised water and coverslips were mounted using S3023 Fluorescence Mounting Medium. Imaging of cells was performed using Zeiss Cell Observer equipped with a 20X / NA 0.8 Plan-Apo DIC II objective and the CCD camera AxioCam and the Zen 3.0 Software (blue edition; Zeiss). Quantification of nuclear FLAG signal was performed using Fiji. Neuronal nuclei were selected as ROI, the mean FLAG intensity of all neuronal nuclei was measured and background subtraction was performed.

5.2.11 Immunohistochemistry

Mouse brains were dissected, fixed in 4% PFA for 24 h and cryoprotected in 30% sucrose in PBS for 48 h. Brains were placed in OCT compound, frozen using dry ice and sectioned at 20 μ m (embryonic) or 50 μ m (P0) on a cryostat. Antigen retrieval of slide-mounted cryosections was performed using Antigen Retrieval Citra Plus Solution according to manufacturer's protocol. Sections were then permeabilised and blocked in 5% normal donkey serum in 0.2% Triton X-100 in PBS for 1 h and incubated with primary antibody diluted in blocking solution at 4 °C overnight. The next day, sections were washed 3 times in PBS and incubated in secondary antibody diluted 1:400 in blocking solution for 1 h. Next, sections were washed 3 times in PBS, incubated in 100 ng/mL DAPI for 10 min and mounted using S3023 Fluorescence Mounting Medium. Images were acquired using Leica TCS SP5 confocal microscope equipped with a 40X / NA 1.3 HCX PL APO oil objective and LAS AF software. The number of TBR2+ and SOX2+ cells was determined in mid-cortical 265- μ m-wide segments using an in-house developed Fiji macro. All quantifications were carried out at equivalent anteroposterior positions between genotypes.

5.2.12 Brain morphology analysis

For analysis of cortical length, P0 mice were decapitated, the brains were removed from the skull and weighed before they were placed in 4% PFA. After 24 h fixation, the brains were placed next to a ruler and photographed. The maximal cortical anteroposterior length was measured using Adobe Illustrator and normalised to the respective brain weight. For analysis of cortical thickness, the fixated brains were cryoprotected in 30% sucrose in PBS for 3 days and then frozen on dry ice. Frozen brains were cut coronally in 50- μ m sections on a cryostat. Sections were stained with indicated antibodies and mounted with Vectashield mounting medium following the above immunohistochemistry protocol (no antigen retrieval). Sections were aligned across genotypes using subcortical anatomical landmarks for orientation (hippocampal length, thalamic size), and images at different positions throughout the brain were acquired using the 4 \times objective of the DMIL LED microscope with the DFC 300G camera and the LAS X software or the 10 \times / 0.3 Plan-NEO Ph1 DICIII objective of the Cell Observer with the CCD camera AxioCam and the ZEN 3.0 (blue edition) software. Cortical thickness was measured at a 45° angle from the dorsal midline using Adobe Illustrator. For each section the mean of both hemispheres was used.

5.2.13 EdU labelling and embryonic sections

Timed-pregnant females were intraperitoneally injected at E14.5 with EdU (30 mg/kg body weight). After 20 h, embryonic brains were dissected, fixed in 4% PFA in PBS overnight following 48 h incubation in 30% sucrose in PBS. The brains were placed in OCT compound, frozen using dry ice and sectioned at 20 μ m on a cryostat. EdU detection was performed with the Click-iT EdU Alexa Fluor 488 imaging kit protocol according to the manufacturer's instructions. Immunostaining was carried out on slide-mounted cryosections following the above-described protocol and images were acquired using a Zeiss LSM700 confocal microscope equipped with a 10X / NA 0.3 air objective and using Zen 3.0 Software (black edition). Q-fraction analysis followed previously established practices [203]. In brief, mid-cortical 200- μ m-wide segments were imaged and EdU+Ki67- cells positioned basal to the SVZ counted, followed by the count of all EdU+ cells. The ratio of the two counts represented the Q-fraction. All quantifications were carried out at equivalent anteroposterior positions between genotypes.

5.2.14 Behaviour experiments

The mice were housed in a temperature-controlled vivarium maintained on a 12-h light–dark cycle and tests were conducted during the light cycle. All procedures were performed at the Interdisciplinary Neurobehavioural Core of Heidelberg University and approved by the Regierungspräsidium in Karlsruhe. Distress and number of animals was minimised. No previous analyses were performed

on animals used for behavioural testing. We used mixed genotype home cages with 2 - 4 animals per cage and performed the testing on three independent cohorts of *Myt1l*^{+/-} mice (first cohort: 5 males, 2 females; second cohort: 12 males, 13 females; third cohort: 3 males, 8 females) and *Myt1l*^{+/+} littermates (first cohort: 1 male, 3 females; second cohort: 2 males, 2 females; third cohort: 11 males, 7 females). The rescue experiments were performed on three independent cohorts of *Myt1l*^{+/-} mice (first cohort: 6 males, 12 females; second cohort: 10 males, 18 females; third cohort: 1 male, 5 females) and *Myt1l*^{+/+} littermates (first cohort: 9 males, 7 females; second cohort: 16 males, 4 females; third cohort: 3 male, 3 females). The mice were injected intraperitoneally with the drug (20 mg/kg lamotrigine) or vehicle (5% PEG 400 in NaCl) 60 min before each behaviour test. At P4, animals were marked by foot tattoo with non-toxic animal tattoo ink. The SHIRPA procedure was performed on all animals to exclude motor or sensory defects of mutant mice.

Ultrasonic vocalisation (USV)

P5 and P8 pups were isolated from the mother and placed in an empty glass container (6 cm × 9.5 cm × 7.5 cm). USV was recorded for 5 min using an UltraSoundGate condenser microphone (CM16/CMPA) placed 30 cm above the testing arena. The microphone was connected to a computer via an Avisoft UltraSoundGate USG416H audio device. The MATLAB package DeepSqueak was used for counting and categorisation of the calls. Categorisation was performed by Bhuvaneshwari Nagarajan.

Elevated plus maze (EPM)

The EPM is a cross-shaped platform (grey opaque plastic material) with equally sized arms (6 cm × 35 cm) and a central intersection (6 cm × 6 cm), allowing animals to move freely into each zone of the maze. Two of the arms (opposing each other) are flanked by 17 cm opaque walls; the remaining two arms are without walls. The EPM is elevated 70 cm above the floor. At P22, animals were placed in the central intersection and allowed to explore the maze for 10 min. Movements were recorded with a top-mounted video camera and analysed using the tracking software SYGNIS TRACKER.

Open field(OF)

The OF is a test for motor activity and anxiety-like behaviour in mice and was performed on P23. In this test, mice were placed in the middle of a white wooden box (60 cm × 60 cm × 30 cm) with an illumination of about 80 lux for 10 min. Movements were recorded with a top-mounted video camera and analysed using the tracking software SYGNIS TRACKER. For the drug treatment, the mice were injected intraperitoneal with 20 mg/kg lamotrigine or vehicle (PEG) in NaCl 1h

before measurement.

Social chamber test (SCT)

The SCT was designed to assess social interaction of the test mouse with a familiar littermate and an unfamiliar mouse and was performed with one- and three-month-old mice. The apparatus is composed of a transparent plexiglass box (20 cm × 61 cm × 40 cm) with three compartments including openings between the compartments. A wire mesh cylinder was placed in the left and right compartment. The test was subdivided into habituation time and two trials, 5 minutes each. In the habituation time, the test mouse was introduced into the apparatus with free access to all compartments. In trial 1 (social recognition), a littermate mouse of the same sex (isolated 12 h before the trial) was placed into the right wire mesh cylinder and the subject mouse was allowed to explore all compartments. In trial 2 (social discrimination), an unfamiliar mouse of the same sex from a different strain (NMRI) was placed into the left mesh wire cylinder and the subject mouse was again allowed to freely explore all compartments. Movements were recorded with a top-mounted video camera and analysed using the tracking software SYGNIS TRACKER.

Marble Burying

Two-months-old animals were habituated in a standard cage (29 cm × 22 cm × 14 cm) for 5 min. Afterwards, 9 standard glass toy marbles (assorted styles and colours, 15 mm diameter, 5.2 g in weight) were put on the surface of the bedding in 3 rows of 3 marbles. The digging behaviour of the animal was monitored for 5 min with a video camera. Individual burying events, time spent burying and the number of buried marbles were manually analysed.

LABORAS

The LABORAS home cage observation is a system that uses a carbon fibre platform to detect behaviour-specific vibration patterns produced by the animal. A home cage is placed on top of the platform, and the specific software processes the produced vibrations into various behavioural parameters. We monitored two-months-old animals over 5 h. Animals were placed individually in the calibrated cage under standard housing condition with free access to food and water. For the drug treatment, the mice were injected i.p. with 20 mg/kg lamotrigine or vehicle before being placed in the cage.

5.2.15 Transcriptome analysis using RNA-sequencing

To collect primary mouse brain samples, the cortex of E18.5 or the prefrontal cortex of P0, P22, and 3 months-old mice was dissected and placed into TRIzol. Human neurons were harvested

from pure cultures at day 7 or upon co-culture with primary mouse glia at day 43 by addition of TRIzol to the cultures. RNA harvested in TRIzol was isolated using the Zymo Research RNA Miniprep kit following the manufacturer’s instructions. For RNA-sequencing, libraries were prepared following the dUTP protocol [204] and paired-end sequencing reads (100bp) were generated on NovaSeq 6000 platforms (Illumina). Bioinformatic analyses were supported by Bryce Lim, Manu Saraswat, Eric Poisel, Christian Arnold and Ignacio L. Ibarra. Raw reads were mapped to the reference genomes hg38 or mm10 using STAR [205] and differential expression determined using DESeq2 [206] (R package version 1.28.1) with size factor normalisation and Wald significance tests. For bulk mouse data, we used genetic sex as a covariate. For the **iNs!** (**iNs!**), we used sample ID as a covariate and computationally removed mouse reads for the 6-weeks samples. Raw p-value histograms were used to verify that the assumptions of the Wald test were satisfied (here: $N(0, 1)$ null distribution for gene dispersions) before continuing. If this was not the case, we estimated the variance of the null-model from the test statistics using the package `fdrtool` [207] (version 1.2.15) using the Wald statistics as input (empirical null modelling). The p-values were then recalibrated based on the empirically-estimated null variance. `EnhancedVolcano` (version 1.8.0) (<https://github.com/kevinblighe/EnhancedVolcano>) was used to make volcano plots, and `pheatmap` (version 1.0.12) (<http://CRAN.R-project.org/package=pheatmap>) was used to generate heatmaps. Tissue gene expression data were obtained from the Genotype-Tissue Expression (GTEx) portal (<https://gtexportal.org>) [159]. Gene Set Enrichment Analysis (GSEA) was performed using signatures for specific cell types derived either from tabula muris using the top 500 most highly-expressed unique genes within each cell type, or Lander and PanglaoDB-derived signatures including the top 500 genes from each list [208–211]. Significance for GSEA profiles were determined by an $FDR < 0.25$ as described [212]. Pathway enrichment analysis was performed using Ingenuity Pathway Analysis (IPA) [213] and significantly enriched pathways were identified with the criterion $p\text{-value} < 0.1$ using Fisher’s exact test. For functional enrichment analysis significantly deregulated genes ($p\text{-adj} < 0.1$) were analysed using `g:Profiler` [214]. Odds ratio and gene overlap analysis was performed using the `GeneOverlap` R package (version 1.26.0) [215]. Overlap of deregulated genes with disease risk genes was manually determined and tested for significance using the Fisher’s exact test in R. Motif enrichment analysis at upregulated genes was performed using `Enrichr` and volcano plots were generated using `Appyter` [216, 217]. For single cell RNA-Seq experiments, prefrontal cortices from P0 mice were extracted and dissociated into single cells following the protocol for primary cultures, washed in HBSS + 0.04% BSA, fixed in ice-cold 80% methanol and stored at -20°C . Barcoding oligonucleotides were designed following the ECCITE-Seq [218] scheme with an amine group at the 5’ end, which were used to chemically label the fixed cells following a previously published protocol [219]. We pooled 20,000 cells from two *Myt1l*^{+/+}, *Myt1l*^{+/-} and *Myt1l*^{-/-} mice, respectively. Each pool was loaded into an individual

lane of the Chromium Controller (10x Genomics). The Chromium Single Cell 5' v1 reagent kit was employed to process the samples according to the manufacturer's instructions, with modifications in the cDNA and library preparation steps suggested by the ECCITE-Seq protocol to generate the barcoded oligonucleotide libraries in parallel. Expression and barcode libraries were then diluted to equimolar amounts, pooled in a 9 to 1 ratio and sequenced using a NovaSeq 6000 (Illumina). Single cell RNA-Seq data was analysed using 10x Genomics Cell Ranger (version 4.0.0) [220], Seurat (version 4.0) [221], and Scanpy (version 1.6.0) [222]. Cells containing fewer than 200 or greater than 4000 features, or with mitochondrial genes making up over 15% of genes, were discarded. We used scArches (v0.3.5) [223] with the scANVI model [224] to calculate latent space of dimension ten, and to assign cell type annotations by mapping our data onto reference data [147] using default parameters. Assignments were verified by marker expression. Leiden clustering was performed on latent space (default parameters, $k = 15$). Two clusters with average annotation probability scores $< 80\%$ were annotated based on marker gene expression; microglia with *Tmem119* and *Aif1*, and blood cells with *Hba-a1* and *Hbb-bs*. These were removed for downstream analysis. Subpopulations of each cell type most affected by *Myt1l* mutation were identified using MELD (version 1.0) [148] with parameters $\text{Beta}=31$ and $\text{KNN}=5$ which were determined using grid search. Differential expression was performed on these subpopulations using MAST (version 1.16.0) [225] within Seurat's FindMarkers function ($\text{logfc.threshold} = 0$, $\text{min.pct} = 0.05$, all other parameters default). GSEA was performed as described above. Sequencing reads are available on NCBI GEO GSE171327.

5.2.16 Chromatin binding using CUT&RUN

The prefrontal cortex of E18.5, P0 and 3-months mice was prepped, and single cells were prepared following the protocol for primary culture preparation. 300,000 cells per animal were washed twice with wash buffer, then resuspended in wash buffer and added to concanavalin-A beads pre-activated with cold binding buffer. The bead-cell suspension was rotated at Room temperature (RT) for 10 minutes and then split into two vials. Supernatant was removed on a magnet and the beads resuspended in antibody buffer. Primary antibody (rabbit anti-MYT1L) or control (rabbit IgG) was added at 1:100 final concentration, and the cells were incubated on a shaker at 4°C for 2 h. Beads were washed twice with digitonin-wash buffer, resuspended in 700 ng/mL pAG-MNase in digitonin-wash buffer, and rotated at 4°C for 1 hour. Beads were washed twice with digitonin-wash buffer followed by resuspension in digitonin-wash buffer and then placed on ice. 1 μL of 100 mM CaCl_2 was added to initiate chromatin digestion, and the mixture was incubated on ice for 30 min. 50 μL of 2x stop buffer was added, and the bead suspension was incubated at 37°C for 10 min to release fragments from cells. The supernatant was subjected to phenol-chloroform extraction, and purified DNA fragments were used for library preparation and sequencing. Li-

libraries were prepared based on the library preparation manual of NEBNext DNA Library Prep Kit for Illumina (NEB E7645), with specific modifications to make libraries from small DNA fragments ([dx.doi.org/10.17504/protocols.io.wvgfe3w](https://doi.org/10.17504/protocols.io.wvgfe3w)) and paired-end sequencing reads (40bp) were generated on NextSeq 2000 platforms (Illumina). CUT&RUN data was analysed using the `nf-core/cutandrun` pipeline v1.0 (10.5281/zenodo.5653535). The Venn diagram tool from Bioinformatics Evolutionary Genomics in Gent was used (<http://bioinformatics.psb.ugent.be/webtools/Venn/>). Homer `findMotifsGenome.pl` was run on the peak files with the parameters `-size -75,75 -mask -mknown` and the MYT1L motif AAAGTTW (<http://homer.ucsd.edu/homer/>).

5.2.17 Brain slice preparation and electrophysiology

The mice (4–6 weeks post-natal) were deeply anaesthetised with the volatile anaesthetic isoflurane and transcardially perfused with 30 mL NMDG aCSF containing the following (in mM) 92 NMDG, 2.5 KCl, 1.25 NaH₂PO₄, 30 NaHCO₃, 20 HEPES, 25 glucose, 2 thiourea, 5 Na-ascorbate, 3 Na-pyruvate, 0.5 CaCl₂ and 10 MgCl₂, oxygenated with carbogen gas (95% O₂ and 5% CO₂, pH 7.3–7.4). Mice were decapitated and brains were removed. Transverse hippocampal slices of 400 μ m thickness from both hemispheres were cut on a slicer (HR2; Sigmund Elektronik, Germany) in oxygenated NMDG aCSF. Slices were initially recovered in oxygenated NMDG aCSF at 34 \pm 1 $^{\circ}$ C for 11 min followed by incubation in HEPES holding aCSF containing the following (in mM) 92 NaCl, 2.5 KCl, 1.25 NaH₂PO₄, 30 NaHCO₃, 20 HEPES, 25 glucose, 2 thiourea, 5 Na-ascorbate, 3 Na-pyruvate, 2 CaCl₂ and 2 MgCl₂, oxygenated at 23 \pm 1 $^{\circ}$ C until used. During experiments, slices were placed in a recording chamber and superfused with oxygenated aCSF containing (in mM): 125 NaCl, 25 NaHCO₃, 1.25 NaH₂PO₄, 2.5 KCl, 25 glucose, 2 CaCl₂ and 1 MgCl₂ at 31 \pm 1 $^{\circ}$ C. CA1 pyramidal cells were identified by large somata in the stratum pyramidale with accommodating firing pattern under infrared and differential interference contrast microscope (Olympus BX51WI). The patch electrodes (3–6 M) were pulled from borosilicate glasses with a filament (O.D. 1.5 mm, I.D. 0.86 mm; Science Products, Germany). For spontaneous EPSCs measurements, pyramidal cells were voltage-clamped at -70 mV with a K⁺-based internal solution containing the following (in mM): 130 K-gluconate, 10 Na-gluconate, 10 HEPES, 10 phosphocreatine, 4 NaCl, 4 MgATP, 0.3 GTP and 0.5% biocytin. For spontaneous IPSCs measurements, putative pyramidal cells were voltage-clamped at 0 mV with a Cs⁺-based internal solution containing the following (in mM): 126 Cs-gluconate, 4 Cs-Cl, 10 HEPES, 10 phosphocreatine, 4 MgATP, 0.3 GTP and 2.5 QX-314 in the presence of CNQX (10 μ M) and D-APV (50 μ M). All slice recordings were performed using an EPC 10 amplifier (HEKA, Germany) and data were acquired by using Patchmaster software (HEKA, Germany). Pipette capacitance was maximally compensated. Series resistance (\leq 30 M) was partially compensated in voltage-clamp mode (correction 70–80% with a 10- μ s lag) and fully compensated in current-clamp mode (correction 100% with a 10- μ s lag). Data

were excluded if the series resistance changed more than 20%. Liquid junction potentials were not corrected. Signals were filtered at 3 kHz and sampled at 20 kHz. Recordings of excitatory synaptic currents in primary hippocampal cultures at DIV11 were performed in voltage-clamp mode at -70 mV holding potential, with an internal solution containing (in mM): 130 Cs-Gluconate, 5 TEA-Chloride, 0.2 EGTA, 4 Mg-ATP, 0.3 Na-GTP, 12 Na-Phosphocreatin, and 10 HEPES-NaOH (pH adjusted to 7.4, 315 mOsm) in the presence or absence of 0.5 μ M tetrodotoxin (TTX). The following extracellular solution was used (in mM): 125 NaCl, 2.5 KCl, 25 NaHCO₃, 0.4 Ascorbic acid, 3 Myo-inositol, 2 Sodium Pyruvate, 1.25 NaH₂PO₄·2H₂O, 2 CaCl₂, 1 MgCl₂, 25 D(+)-glucose (pH 7.4, 315 mOsm). Culture recordings were performed using a Multiclamp 700B amplifier (Molecular Devices) controlled with Clampex 10.4 or a dual-channel HEKA amplifier controlled by Patchmaster 10 software. Culture data were analysed offline using Clampfit 10.4 and custom-written macros in IgorPro (Wavemetric). Slice EPSCs were firstly automatically detected by Mini Analysis (Synaptosoft) and then inspected manually. All recordings were performed blinded with cultures and animals originating of the same litter analysed in parallel.

5.2.18 Multi-electrode array (MEA)

MEA measurements were performed using the Maestro Pro multi-well device with the Axis Navigator software and 48-well plates containing 16 electrodes per well. The data was acquired using a sampling rate of 12.5 kHz and filtered using a 200–3000 Hz Butterworth bandpass filter. The detection threshold was set to 6 \times standard deviation of the baseline electrode noise. After equilibration for 20 min, spontaneous activity was recorded for 10 min at the indicated days. For acute treatments of human induced or mouse hippocampal neurons, indicated concentrations of drugs were added, and the plate was measured before and 2 h after the treatment. The spike raster plots were produced using the Neural Metric Tool. The spike list files were used to analyse the data in R Studio with the MEA analysis package mearTools for interpretation of neuronal activity patterns [226]. Wells, in which fewer than 4 electrodes were active (>1 spike / min) were considered inactive and removed from analyses. Bursts were detected with the maximum interval algorithm (min number of spikes: 5, max inter-spike interval: 100 ms). If neurons on ≥ 3 electrodes fired in a time window of ≤ 10 ms, it was considered a network spike.

5.2.19 Quantitative real time polymerase chain reaction (qRT-PCR)

Samples were harvested in TRIzol and RNA was isolated using the Zymo Research RNA Miniprep kit following the manufacturer's instructions. Extracted RNA samples were stored at -80°C until use. cDNA synthesis was performed with the LunaScript RT Super Mix Kit according to the manufacturer's guidelines. Quantitative assessment of gene expression was analysed by qPCR, which was performed in 384-well format with the QuantStudio5 Real Time PCR system. Per

reaction, 5 μ L Power SYBR Green PCR Master Mix were mixed with 2.1 μ L nuclease-free water, 0.4 μ L 10 μ M primer mix, containing 5 μ M forward and 5 μ M reverse primer and 2.5 μ L cDNA. The following PCR conditions were used:

Step	Temperature	Time
1	50°C	2 min
2	95°C	10 min
3	95°C	15 s
4	60°C	1 min
		40 cycles

Data processing and visualisation were performed with QuantStudio, MS Excel and GraphPad Prism.

5.2.20 SDS-PAGE and Western blot

iNs were washed once in PBS and scraped in 1X SDS buffer containing benzonase (1:100). Brain samples were harvested in RIPA buffer with 1:100 PI, sonicated and concentrations were determined using a BSA standard and a BCA protein assay. Samples were separated using the NuPAGE 4-12% Bis-Tris gels and running them at 100 – 150 V in MOPS buffer. Proteins were transferred onto a nitrocellulose membrane overnight at 75 mA in transfer buffer using a wet transfer system. Total protein stain was performed with Revert-700 total protein stain according to manufacturer's protocol and imaged using ODYSSEY CLx Imaging System (LI-COR). Total protein staining was removed by incubating the membrane in total protein stain reversal buffer for 5 min. Subsequently, the membrane was blocked in 2% BSA in PBS-T for 1-2 h at RT and incubated with primary antibody diluted in 2% BSA in PBS-T overnight at 4 °C on a shaking platform, followed by three 15 min washes in PBS-T. The membrane was then incubated with secondary antibody diluted in 2% BSA in PBS-T for 1-2 h slowly shaking at RT, washed three times for 15 min in PBS-T and imaged using ODYSSEY CLx Imaging System (LI-COR). Protein expression was normalised to total protein stain using Image Studio Lite software.

5.2.21 Statistical analysis

Statistical analyses were performed with R Studio and GraphPad Prism. The distribution of the data was determined using Shapiro-Wilk test and based on the results, statistical analysis was performed using t-test, Mann-Whitney test or analysis of variance (ANOVA) test with Dunn's correction for multiple testing. No statistical methods were used to predetermine sample size. The type of statistical test used for each data set and the number of biological and technical replicates

is indicated in the figure or the corresponding figure legend. Data are presented as means \pm SEM unless stated otherwise.

REFERENCES

1. Bianconi, E. *et al.* An estimation of the number of cells in the human body. *Annals of human biology* **40**, 463–471 (Nov. 2013).
2. Hashimoto, M. & Sasaki, H. Epiblast Formation by TEAD-YAP-Dependent Expression of Pluripotency Factors and Competitive Elimination of Unspecified Cells. *Developmental Cell* **50**, 139–154 (July 2019).
3. Nichols, J. & Smith, A. Naive and Primed Pluripotent States. *Cell Stem Cell* **4**, 487–492 (June 2009).
4. Kiecker, C., Bates, T. & Bell, E. Molecular specification of germ layers in vertebrate embryos. *Cellular and Molecular Life Sciences* **73**, 923 (Mar. 2016).
5. Muhr, J. & Ackerman, K. M. Embryology, Gastrulation. *StatPearls* (Apr. 2022).
6. Argelaguet, R. *et al.* Multi-omics profiling of mouse gastrulation at single-cell resolution. *Nature 2019 576:7787* **576**, 487–491 (Dec. 2019).
7. Waddington, C. H. The strategy of the genes: A discussion of some aspects of theoretical biology. *The Strategy of the Genes: A Discussion of Some Aspects of Theoretical Biology*, 1–262 (Jan. 1957).
8. Goldberg, A. D., Allis, C. D. & Bernstein, E. Epigenetics: a landscape takes shape. *Cell* **128**, 635–638 (Feb. 2007).
9. Tsankov, A. M. *et al.* Transcription factor binding dynamics during human ES cell differentiation. *Nature 2015 518:7539* **518**, 344–349 (Feb. 2015).
10. Gabrielsen, O. S. & Sentenac, A. RNA polymerase III (C) and its transcription factors. *Trends in biochemical sciences* **16**, 412–416 (1991).

11. Matsui, T., Segall, J., Weil, P. A. & Roeder, R. G. Multiple factors required for accurate initiation of transcription by purified RNA polymerase II. *Journal of Biological Chemistry* **255**, 11992–11996 (Dec. 1980).
12. Mermelstein, F. H., Flores, O. & Reinberg, D. Initiation of transcription by RNA polymerase II. *Biochimica et biophysica acta* **1009**, 1–10 (Sept. 1989).
13. Andersson, R. & Sandelin, A. Determinants of enhancer and promoter activities of regulatory elements. *Nature Reviews Genetics* 2019 *21:2* **21**, 71–87 (Oct. 2019).
14. Wolffe, A. P., Wong, J. & Pruss, D. Activators and repressors: making use of chromatin to regulate transcription. *Genes to cells : devoted to molecular & cellular mechanisms* **2**, 291–302 (1997).
15. Holmberg, J. & Perlmann, T. Maintaining differentiated cellular identity. *Nature Reviews Genetics* 2012 *13:6* **13**, 429–439 (May 2012).
16. Mann, R. S. & Carroll, S. B. Molecular mechanisms of selector gene function and evolution. *Current Opinion in Genetics and Development* **12**, 592–600 (Oct. 2002).
17. Zaret, K. S. & Mango, S. E. Pioneer transcription factors, chromatin dynamics, and cell fate control. *Current opinion in genetics & development* **37**, 76–81 (Apr. 2016).
18. Bang, A. G. & Goulding, M. D. Regulation of vertebrate neural cell fate by transcription factors. *Current opinion in neurobiology* **6**, 25–32 (1996).
19. Raposo, A. A. *et al.* Ascl1 Coordinately Regulates Gene Expression and the Chromatin Landscape during Neurogenesis. *Cell reports* **10**, 1544–1556 (Mar. 2015).
20. Smith, D. K., Yang, J., Liu, M. L. & Zhang, C. L. Small Molecules Modulate Chromatin Accessibility to Promote NEUROG2-Mediated Fibroblast-to-Neuron Reprogramming. *Stem Cell Reports* **7**, 955–969 (Nov. 2016).
21. Aydin, B. *et al.* Proneural factors Ascl1 and Neurog2 contribute to neuronal subtype identities by establishing distinct chromatin landscapes. *Nature neuroscience* **22**, 897 (June 2019).
22. Wapinski, O. L. *et al.* Hierarchical mechanisms for direct reprogramming of fibroblasts to neurons. *Cell* **155**, 621 (Oct. 2013).

23. Li, L. M. & Arnosti, D. N. Long- and short-range transcriptional repressors induce distinct chromatin states on repressed genes. *Current biology : CB* **21**, 406 (Mar. 2011).
24. Mori, N., Schoenherr, C., Vandenberg, D. J. & Anderson, D. J. A common silencer element in the SCG10 and type II Na⁺ channel genes binds a factor present in nonneuronal cells but not in neuronal cells. *Neuron* **9**, 45–54 (July 1992).
25. Chong, J. A. *et al.* REST: A Mammalian Silencer Protein That Restricts Sodium Channel Gene Expression to Neurons. *Cell* **80**, 949–957 (1995).
26. Kraner, S. D., Chong, J. A., Tsay, H. J. & Mandel, G. Silencing the type II sodium channel gene: A model for neural-specific gene regulation. *Neuron* **9**, 37–44 (July 1992).
27. GURDON, J. B. The Developmental Capacity of Nuclei taken from Intestinal Epithelium Cells of Feeding Tadpoles. *Development* **10**, 622–640 (Dec. 1962).
28. Wilmut, I., Schnieke, A. E., McWhir, J., Kind, A. J. & Campbell, K. H. Viable offspring derived from fetal and adult mammalian cells. *Nature* **385**, 810–813 (Feb. 1997).
29. Takahashi, K. & Yamanaka, S. Induction of pluripotent stem cells from mouse embryonic and adult fibroblast cultures by defined factors. *Cell* **126**, 663–676 (Aug. 2006).
30. Hobert, O. Regulatory logic of neuronal diversity: terminal selector genes and selector motifs. *Proceedings of the National Academy of Sciences of the United States of America* **105**, 20067–20071 (Dec. 2008).
31. Collins, P. & Billett, F. S. The terminology of early development: History, concepts, and current usage. *Clinical Anatomy* **8**, 418–425 (Jan. 1995).
32. Wilson, S. W. & Houart, C. Early Steps in the Development of the Forebrain. *Developmental cell* **6**, 167 (Feb. 2004).
33. Rubenstein, J. L. & Beachy, P. A. Patterning of the embryonic forebrain. *Current opinion in neurobiology* **8**, 18–26 (1998).
34. Rubenstein, J. L., Shimamura, K., Martinez, S. & Puelles, L. Regionalization of the prosencephalic neural plate. *Annual review of neuroscience* **21**, 445–477 (1998).

35. Huttner, W. B. & Brand, M. Asymmetric division and polarity of neuroepithelial cells. *Current opinion in neurobiology* **7**, 29–39 (1997).
36. Wodarz, A. & Huttner, W. B. Asymmetric cell division during neurogenesis in Drosophila and vertebrates. *Mechanisms of Development* **120**, 1297–1309 (2003).
37. Florio, M. & Huttner, W. B. Neural progenitors, neurogenesis and the evolution of the neocortex. *Development (Cambridge, England)* **141**, 2182–2194 (2014).
38. Rakic, P. A small step for the cell, a giant leap for mankind: a hypothesis of neocortical expansion during evolution. *Trends in Neurosciences* **18**, 383–388 (Sept. 1995).
39. Sauer, M. E. & Walker, B. E. Radioautographic study of interkinetic nuclear migration in the neural tube. *Proceedings of the Society for Experimental Biology and Medicine. Society for Experimental Biology and Medicine (New York, N.Y.)* **101**, 557–560 (1959).
40. Taverna, E. & Huttner, W. B. Neural progenitor nuclei IN motion. *Neuron* **67**, 906–914 (Sept. 2010).
41. Götz, M. & Huttner, W. B. The cell biology of neurogenesis. *Nature reviews. Molecular cell biology* **6**, 777–788 (Nov. 2005).
42. Campbell, K. & Götz, M. Radial glia: Multi-purpose cells for vertebrate brain development. *Trends in Neurosciences* **25**, 235–238 (May 2002).
43. Asami, M. *et al.* The role of Pax6 in regulating the orientation and mode of cell division of progenitors in the mouse cerebral cortex. *Development (Cambridge, England)* **138**, 5067–5078 (Dec. 2011).
44. Osumi, N., Shinohara, H., Numayama-Tsuruta, K. & Maekawa, M. Concise Review: Pax6 Transcription Factor Contributes to both Embryonic and Adult Neurogenesis as a Multifunctional Regulator. *Stem Cells* **26**, 1663–1672 (July 2008).
45. Malatesta, P., Hartfuss, E. & Götz, M. Isolation of radial glial cells by fluorescent-activated cell sorting reveals a neuronal lineage. *Development* **127**, 5253–5263 (Dec. 2000).

46. Anthony, T. E., Klein, C., Fishell, G. & Heintz, N. Radial Glia Serve as Neuronal Progenitors in All Regions of the Central Nervous System. *Neuron* **41**, 881–890 (Mar. 2004).
47. Englund, C. *et al.* Pax6, Tbr2, and Tbr1 are expressed sequentially by radial glia, intermediate progenitor cells, and postmitotic neurons in developing neocortex. *The Journal of neuroscience : the official journal of the Society for Neuroscience* **25**, 247–251 (Jan. 2005).
48. Kriegstein, A., Noctor, S. & Martínez-Cerdeño, V. Patterns of neural stem and progenitor cell division may underlie evolutionary cortical expansion. *Nature reviews. Neuroscience* **7**, 883–890 (Nov. 2006).
49. Noctor, S. C., Martínez-Cerdeño, V., Ivic, L. & Kriegstein, A. R. Cortical neurons arise in symmetric and asymmetric division zones and migrate through specific phases. *Nature neuroscience* **7**, 136–144 (Feb. 2004).
50. Rakic, P. Mode of cell migration to the superficial layers of fetal monkey neocortex. *The Journal of comparative neurology* **145**, 61–83 (1972).
51. Agirman, G., Broix, L. & Nguyen, L. Cerebral cortex development: an outside-in perspective. *FEBS letters* **591**, 3978–3992 (Dec. 2017).
52. Lim, L., Mi, D., Llorca, A. & Marín, O. Development and functional diversification of cortical interneurons. *Neuron* **100**, 294 (Oct. 2018).
53. Desai, A. R. & McConnell, S. K. Progressive restriction in fate potential by neural progenitors during cerebral cortical development. *Development (Cambridge, England)* **127**, 2863–2872 (July 2000).
54. Paridaen, J. T. & Huttner, W. B. Neurogenesis during development of the vertebrate central nervous system. *EMBO Reports* **15**, 351 (2014).
55. Lathia, J. D., Mattson, M. P. & Cheng, A. Notch: From Neural Development to Neurological Disorders. *Journal of neurochemistry* **107**, 1471 (Dec. 2008).
56. Hatakeyama, J. *et al.* Hes genes regulate size, shape and histogenesis of the nervous system by control of the timing of neural stem cell differentiation. *Development (Cambridge, England)* **131**, 5539–5550 (Nov. 2004).

57. Dong, Z., Yang, N., Yeo, S. Y., Chitnis, A. & Guo, S. Intralineaage directional Notch signaling regulates self-renewal and differentiation of asymmetrically dividing radial glia. *Neuron* **74**, 65–78 (Apr. 2012).
58. Formosa-Jordan, P. A., Ibañes, M., Ares, S. & Frade, J. M. Lateral inhibition and neurogenesis: novel aspects in motion. *The International journal of developmental biology* **57**, 341–350 (2013).
59. Tiberi, L. *et al.* BCL6 controls neurogenesis through Sirt1-dependent epigenetic repression of selective Notch targets. *Nature Neuroscience* 2012 15:12 **15**, 1627–1635 (Nov. 2012).
60. Sloan, S. A. & Barres, B. A. Mechanisms of astrocyte development and their contributions to neurodevelopmental disorders. *Current opinion in neurobiology* **27**, 75 (2014).
61. Kumar, V. *et al.* The Role of Notch, Hedgehog, and Wnt Signaling Pathways in the Resistance of Tumors to Anticancer Therapies. *Frontiers in Cell and Developmental Biology* **9**, 857 (Apr. 2021).
62. Okerlund, N. D. & Cheyette, B. N. Synaptic Wnt signaling—a contributor to major psychiatric disorders? *Journal of Neurodevelopmental Disorders* **3**, 162–174 (Apr. 2011).
63. Chenn, A. & Walsh, C. A. Increased Neuronal Production, Enlarged Forebrains and Cytoarchitectural Distortions in β -Catenin Overexpressing Transgenic Mice. *Cerebral Cortex* **13**, 599–606 (June 2003).
64. Wrobel, C. N., Mutch, C. A., Swaminathan, S., Taketo, M. M. & Chenn, A. Persistent expression of stabilized beta-catenin delays maturation of radial glial cells into intermediate progenitors. *Developmental biology* **309**, 285–297 (Sept. 2007).
65. Hirsch, C., Campano, L. M., Wöhrle, S. & Hecht, A. Canonical Wnt signaling transiently stimulates proliferation and enhances neurogenesis in neonatal neural progenitor cultures. *Experimental cell research* **313**, 572–587 (Feb. 2007).
66. Hirabayashi, Y. & Gotoh, Y. Stage-dependent fate determination of neural precursor cells in mouse forebrain. *Neuroscience research* **51**, 331–336 (2005).

67. Munji, R. N., Choe, Y., Li, G., Siegenthaler, J. A. & Pleasure, S. J. Wnt Signaling Regulates Neuronal Differentiation of Cortical Intermediate Progenitors. *Journal of Neuroscience* **31**, 1676–1687 (Feb. 2011).
68. Carballo, G. B., Honorato, J. R., De Lopes, G. P. F. & Spohr, T. C. L. D. S. E. A highlight on Sonic hedgehog pathway. *Cell Communication and Signaling 2018 16:1* **16**, 1–15 (Mar. 2018).
69. Wang, L., Hou, S. & Han, Y. G. Hedgehog signaling promotes basal progenitor expansion and the growth and folding of the neocortex. *Nature neuroscience* **19**, 888 (July 2016).
70. Han, Y. G. Sonic hedgehog signaling: A conserved mechanism for the expansion of outer radial glia and intermediate progenitor cells and for the growth and folding of the neocortex. *Neurogenesis* **3** (2016).
71. Shikata, Y. *et al.* Ptch1-mediated dosage-dependent action of Shh signaling regulates neural progenitor development at late gestational stages. *Developmental biology* **349**, 147–159 (Jan. 2011).
72. Winkler, C. C. *et al.* The Dorsal Wave of Neocortical Oligodendrogenesis Begins Embryonically and Requires Multiple Sources of Sonic Hedgehog. *Journal of Neuroscience* **38**, 5237–5250 (May 2018).
73. Dave, R. K. *et al.* Sonic Hedgehog and Notch Signaling Can Cooperate to Regulate Neurogenic Divisions of Neocortical Progenitors. *PLOS ONE* **6**, e14680 (2011).
74. Rash, B. G., David Lim, H., Breunig, J. J. & Vaccarino, F. M. FGF Signaling Expands Embryonic Cortical Surface Area by Regulating Notch-Dependent Neurogenesis. *The Journal of Neuroscience* **31**, 15604 (Oct. 2011).
75. Morris-Rosendahl, D. J. & Crocq, M. A. Neurodevelopmental disorders—the history and future of a diagnostic concept. <https://doi.org/10.31887/DCNS.2020.22.1/macrocq> **22**, 65–72 (Mar. 2022).
76. Tărlungeanu, D. C. & Novarino, G. Genomics in neurodevelopmental disorders: an avenue to personalized medicine. *Experimental & Molecular Medicine 2018 50:8* **50**, 1–7 (Aug. 2018).

77. Van Bokhoven, H. Genetic and Epigenetic Networks in Intellectual Disabilities. <https://doi.org/10.1146/annurev-genet-110410-132512> **45**, 81–104 (Nov. 2011).
78. An, J. Y. & Claudianos, C. Genetic heterogeneity in autism: From single gene to a pathway perspective. *Neuroscience and biobehavioral reviews* **68**, 442–453 (Sept. 2016).
79. Casanova, E. L., Gerstner, Z., Sharp, J. L., Casanova, M. F. & Feltus, F. A. Widespread Genotype-Phenotype Correlations in Intellectual Disability. *Frontiers in Psychiatry* **9**, 535 (Oct. 2018).
80. Li, Y. *et al.* Genotype and phenotype correlations for SHANK3 de novo mutations in neurodevelopmental disorders. *American journal of medical genetics. Part A* **176**, 2668–2676 (Dec. 2018).
81. Lee, S. H. *et al.* Genetic relationship between five psychiatric disorders estimated from genome-wide SNPs. *Nature Genetics* 2013 45:9 **45**, 984–994 (Aug. 2013).
82. Satterstrom, F. K. *et al.* Large-Scale Exome Sequencing Study Implicates Both Developmental and Functional Changes in the Neurobiology of Autism. *Cell* **180**, 568–584 (Feb. 2020).
83. Coe, B. P. *et al.* Neurodevelopmental disease genes implicated by de novo mutation and copy number variation morbidity. *Nature Genetics* 2018 51:1 **51**, 106–116 (Dec. 2018).
84. Turner, D., Briken, P. & Schöttle, D. Sexual Dysfunctions and Their Association with the Dual Control Model of Sexual Response in Men and Women with High-Functioning Autism. *Journal of Clinical Medicine* 2019, Vol. 8, Page 425 **8**, 425 (Mar. 2019).
85. Kaplanis, J. *et al.* Integrating healthcare and research genetic data empowers the discovery of 28 novel developmental disorders. *bioRxiv*, 797787 (Apr. 2020).
86. Yuen, R. K. *et al.* Whole genome sequencing resource identifies 18 new candidate genes for autism spectrum disorder. *Nature Neuroscience* 2017 20:4 **20**, 602–611 (Mar. 2017).
87. Ruzzo, E. K. *et al.* Inherited and De Novo Genetic Risk for Autism Impacts Shared Networks. *Cell* **178**, 850–866 (Aug. 2019).

88. Brandler, W. M. *et al.* Paternally inherited cis-regulatory structural variants are associated with autism. *Science* **360**, 327–331 (Apr. 2018).
89. Zoghbi, H. Y. & Bear, M. F. Synaptic Dysfunction in Neurodevelopmental Disorders Associated with Autism and Intellectual Disabilities. *Cold Spring Harbor Perspectives in Biology* **4** (Mar. 2012).
90. Bourgeron, T. *From the genetic architecture to synaptic plasticity in autism spectrum disorder* Aug. 2015.
91. Van den Berg, D. L., Heng, J. I. T., Sessa, A. & Dias, C. Editorial: Transcription and chromatin regulators in neurodevelopmental disorders. *Frontiers in Neuroscience* **16** (Sept. 2022).
92. Katayama, Y. *et al.* CHD8 haploinsufficiency results in autistic-like phenotypes in mice. *Nature* 2016 537:7622 **537**, 675–679 (Sept. 2016).
93. Araujo, D. J. *et al.* Foxp1 in Forebrain Pyramidal Neurons Controls Gene Expression Required for Spatial Learning and Synaptic Plasticity. *The Journal of neuroscience : the official journal of the Society for Neuroscience* **37**, 10917–10931 (Nov. 2017).
94. Gordon, A. & Geschwind, D. H. Human in vitro models for understanding mechanisms of autism spectrum disorder. *Molecular Autism* 2020 11:1 **11**, 1–18 (Apr. 2020).
95. Forsingdal, A. *et al.* Can Animal Models of Copy Number Variants That Predispose to Schizophrenia Elucidate Underlying Biology? *Biological psychiatry* **85**, 13–24 (Jan. 2019).
96. Zhao, X. & Bhattacharyya, A. Human Models Are Needed for Studying Human Neurodevelopmental Disorders. *American Journal of Human Genetics* **103**, 829 (Dec. 2018).
97. Kazdoba, T. M., Leach, P. T. & Crawley, J. N. Behavioral phenotypes of genetic mouse models of autism. *Genes, brain, and behavior* **15**, 7 (Jan. 2016).
98. Kroon, T., Sierksma, M. C. & Meredith, R. M. Investigating mechanisms underlying neurodevelopmental phenotypes of autistic and intellectual disability disorders: a perspective. *Frontiers in Systems Neuroscience* **7** (Oct. 2013).

99. Gigeek, C. O. *et al.* A molecular model for neurodevelopmental disorders. *Translational psychiatry* **5** (May 2015).
100. Chen, E. S. *et al.* Molecular Convergence of Neurodevelopmental Disorders. *American Journal of Human Genetics* **95**, 490 (Nov. 2014).
101. Cotney, J. *et al.* The autism-associated chromatin modifier CHD8 regulates other autism risk genes during human neurodevelopment. *Nature Communications* *2015 6:1* **6**, 1–11 (Mar. 2015).
102. Sidorov, M. S., Auerbach, B. D. & Bear, M. F. Fragile X mental retardation protein and synaptic plasticity. *Molecular Brain* **6**, 1–11 (Apr. 2013).
103. Jung, E. M. *et al.* Arid1b haploinsufficiency disrupts cortical interneuron development and mouse behavior. *Nature Neuroscience* *2017 20:12* **20**, 1694–1707 (Nov. 2017).
104. Deneault, E. *et al.* Complete Disruption of Autism-Susceptibility Genes by Gene Editing Predominantly Reduces Functional Connectivity of Isogenic Human Neurons. *Stem cell reports* **11**, 1211–1225 (Nov. 2018).
105. Deneault, E. *et al.* CNTN5 $-/+$ or EHMT2 $-/+$ human iPSC-derived neurons from individuals with autism develop hyperactive neuronal networks. *eLife* **8** (Feb. 2019).
106. Qin, L. *et al.* Social deficits in Shank3-deficient mouse models of autism are rescued by histone deacetylase (HDAC) inhibition. *Nature Neuroscience* *2018 21:4* **21**, 564–575 (Mar. 2018).
107. Mansfield, P., Constantino, J. N. & Baldridge, D. MYT1L: A systematic review of genetic variation encompassing schizophrenia and autism. *American Journal of Medical Genetics, Part B: Neuropsychiatric Genetics* **183**, 227–233 (June 2020).
108. Coursimault, J. *et al.* MYT1L-associated neurodevelopmental disorder: description of 40 new cases and literature review of clinical and molecular aspects. *Human Genetics* **141**, 65–80 (Jan. 2022).
109. Weiner, J. A. & Chun, J. Png-1, a nervous system-specific zinc finger gene, identifies regions containing postmitotic neurons during mammalian embryonic development. *The Journal of Comparative Neurology* **381**, 130–142 (May 1997).

110. Matsushita, F., Kameyama, T., Kadokawa, Y. & Marunouchi, T. Spatiotemporal expression pattern of Myt/NZF family zinc finger transcription factors during mouse nervous system development. *Developmental dynamics : an official publication of the American Association of Anatomists* **243**, 588–600 (2014).
111. Cardoso-Moreira, M. *et al.* Gene expression across mammalian organ development. *Nature* **571**, 505–509 (July 2019).
112. Kim, J. G. *et al.* Myelin transcription factor 1 (Myt1) of the oligodendrocyte lineage, along with a closely related CCHC zinc finger, is expressed in developing neurons in the mammalian central nervous system. *Journal of Neuroscience Research* **50**, 272–290 (Oct. 1997).
113. Vierbuchen, T. *et al.* Direct conversion of fibroblasts to functional neurons by defined factors. *Nature* *2010 463:7284* **463**, 1035–1041 (Jan. 2010).
114. Pang, Z. P. *et al.* Induction of human neuronal cells by defined transcription factors. *Nature* *2011 476:7359* **476**, 220–223 (May 2011).
115. Chanda, S. *et al.* Generation of Induced Neuronal Cells by the Single Reprogramming Factor ASCL1. *Stem Cell Reports* **3**, 282–296 (Aug. 2014).
116. Mall, M. *et al.* Myt1l safeguards neuronal identity by actively repressing many non-neuronal fates. *Nature* **544**, 245–249 (Apr. 2017).
117. Manukyan, A., Kowalczyk, I., Melhuish, T. A., Lemiesz, A. & Wotton, D. Analysis of transcriptional activity by the Myt1 and Myt1l transcription factors. *Journal of cellular biochemistry* **119**, 4644–4655 (June 2018).
118. Romm, E., Nielsen, J. A., Kim, J. G. & Hudson, L. D. Myt1 family recruits histone deacetylase to regulate neural transcription. *Journal of Neurochemistry* **93**, 1444–1453 (June 2005).
119. Berger, S. L. Histone modifications in transcriptional regulation. *Current Opinion in Genetics and Development* **12**, 142–148 (Apr. 2002).
120. Kepa, A. *et al.* Associations of the Intellectual Disability Gene MYT1L with Helix–Loop–Helix Gene Expression, Hippocampus Volume and Hippocampus Activation During Memory Retrieval. *Neuropsychopharmacology* *2017 42:13* **42**, 2516–2526 (May 2017).

121. Chen, J. *et al.* A MYT1L syndrome mouse model recapitulates patient phenotypes and reveals altered brain development due to disrupted neuronal maturation. *Neuron* **109**, 3775–3792 (Dec. 2021).
122. Jiang, Y. *et al.* A novel family of Cys-Cys, His-Cys zinc finger transcription factors expressed in developing nervous system and pituitary gland. *The Journal of biological chemistry* **271**, 10723–10730 (1996).
123. Chen, J., Yen, A., Florian, C. P. & Dougherty, J. D. MYT1L in the making: emerging insights on functions of a neurodevelopmental disorder gene. *Translational Psychiatry* **12** (Dec. 2022).
124. Blanchet, P. *et al.* MYT1L mutations cause intellectual disability and variable obesity by dysregulating gene expression and development of the neuroendocrine hypothalamus. *PLoS genetics* **13** (Aug. 2017).
125. Al Tuwaijri, A. & Alfadhel, M. MYT1L mutation in a patient causes intellectual disability and early onset of obesity: a case report and review of the literature. *Journal of pediatric endocrinology & metabolism : JPEM* **32**, 409–413 (Apr. 2019).
126. Meyer, K. J., Axelsen, M. S., Sheffield, V. C., Patil, S. R. & Wassink, T. H. Germline mosaic transmission of a novel duplication of PXDN and MYT1L to two male half-siblings with autism. *Psychiatric genetics* **22**, 137–140 (June 2012).
127. Stevens, S. J. *et al.* MYT1L is a candidate gene for intellectual disability in patients with 2p25.3 (2pter) deletions. *American journal of medical genetics. Part A* **155A**, 2739–2745 (Nov. 2011).
128. Windheuser, I. C. *et al.* Nine newly identified individuals refine the phenotype associated with MYT1L mutations. English. *American journal of medical genetics. Part A*, 61515–11 (2020).
129. Vlaskamp, D. R. *et al.* Copy number variation in a hospital-based cohort of children with epilepsy. *Epilepsia open* **2**, 244–254 (June 2017).
130. Wang, T. *et al.* De novo genic mutations among a Chinese autism spectrum disorder cohort. *Nature Communications 2016 7:1* **7**, 1–10 (Nov. 2016).

131. Bonaglia, M. C., Giorda, R. & Zanini, S. A new patient with a terminal de novo 2p25.3 deletion of 1.9 Mb associated with early-onset of obesity, intellectual disabilities and hyperkinetic disorder. *Molecular Cytogenetics* **7**, 53 (Aug. 2014).
132. Carvalho, L. M. *et al.* A novel MYT1L mutation in a boy with syndromic obesity: Case report and literature review. *Obesity research & clinical practice* **15**, 124–132 (Mar. 2021).
133. De Ligt, J. *et al.* Diagnostic exome sequencing in persons with severe intellectual disability. *The New England journal of medicine* **367**, 1921–1929 (Nov. 2012).
134. De Rocker, N. *et al.* Refinement of the critical 2p25.3 deletion region: the role of MYT1L in intellectual disability and obesity. *Genetics in medicine : official journal of the American College of Medical Genetics* **17**, 460–466 (June 2015).
135. De Rubeis, S. *et al.* Synaptic, transcriptional, and chromatin genes disrupted in autism. *Nature* **515**, 209 (Nov. 2014).
136. Loid, P. *et al.* A novel MYT1L mutation in a patient with severe early-onset obesity and intellectual disability. *American Journal of Medical Genetics, Part A* **176**, 1972–1975 (Sept. 2018).
137. Mayo, S. *et al.* Haploinsufficiency of the MYT1L gene causes intellectual disability frequently associated with behavioral disorder. *Genetics in Medicine 2015 17:8* **17**, 683–684 (Aug. 2015).
138. Kim, S. *et al.* Postnatal age-differential ASD-like transcriptomic, synaptic, and behavioral deficits in Myt1l-mutant mice. *Cell Reports* **40**, 111398 (Sept. 2022).
139. Wöhr, M. *et al.* Myt1l haploinsufficiency leads to obesity and multifaceted behavioral alterations in mice. *Molecular Autism* **13**, 1–28 (Dec. 2022).
140. Kang, H. J. *et al.* Spatio-temporal transcriptome of the human brain. *Nature 2011 478:7370* **478**, 483–489 (Oct. 2011).
141. Voineagu, I. *et al.* Transcriptomic analysis of autistic brain reveals convergent molecular pathology. *Nature* **474**, 380–386 (June 2011).
142. Ran, X. *et al.* EpilepsyGene: a genetic resource for genes and mutations related to epilepsy. *Nucleic Acids Research* **43**, D893–D899 (Jan. 2015).

143. Hormozdiari, F., Penn, O., Borenstein, E. & Eichler, E. E. The discovery of integrated gene networks for autism and related disorders. *Genome Research* **25**, 142–154 (Jan. 2015).
144. *Human Gene Module - SFARI Gene* tech. rep. ().
145. Treutlein, B. *et al.* Dissecting direct reprogramming from fibroblast to neuron using single-cell RNA-seq. *Nature* *2016 534:7607* **534**, 391–395 (June 2016).
146. Lee, Q. Y. *et al.* Pro-neuronal activity of Myod1 due to promiscuous binding to neuronal genes. *Nature Cell Biology* *2020 22:4* **22**, 401–411 (Mar. 2020).
147. Loo, L. *et al.* Single-cell transcriptomic analysis of mouse neocortical development. *Nature Communications* **10**, 1–11 (Dec. 2019).
148. Burkhardt, D. B. *et al.* Quantifying the effect of experimental perturbations at single-cell resolution. *Nature Biotechnology* **39**, 619–629 (May 2021).
149. Skene, P. J., Henikoff, J. G. & Henikoff, S. Targeted in situ genome-wide profiling with high efficiency for low cell numbers. *Nature Protocols* *2018 13:5* **13**, 1006–1019 (Apr. 2018).
150. Samaco, R. C. *et al.* A partial loss of function allele of Methyl-CpG-binding protein 2 predicts a human neurodevelopmental syndrome. *Human Molecular Genetics* **17**, 1718 (June 2008).
151. Eadie, B. D. *et al.* Fmr1 knockout mice show reduced anxiety and alterations in neurogenesis that are specific to the ventral dentate gyrus. *Neurobiology of Disease* **36**, 361–373 (Nov. 2009).
152. Zhang, Y. *et al.* Rapid single-step induction of functional neurons from human pluripotent stem cells. *Neuron* **78**, 785–798 (June 2013).
153. Yi, F. *et al.* Autism-associated SHANK3 haploinsufficiency causes Ih channelopathy in human neurons. *Science (New York, N.Y.)* **352** (May 2016).
154. Chanda, S. *et al.* Direct Reprogramming of Human Neurons Identifies MARCKSL1 as a Pathogenic Mediator of Valproic Acid-Induced Teratogenicity. *Cell stem cell* **25**, 103–119 (July 2019).

155. Pak, C. H. *et al.* Human Neuropsychiatric Disease Modeling using Conditional Deletion Reveals Synaptic Transmission Defects Caused by Heterozygous Mutations in NRXN1. *Cell stem cell* **17**, 316–328 (Sept. 2015).
156. Lin, H. C. *et al.* NGN2 induces diverse neuron types from human pluripotency. *Stem cell reports* **16**, 2118–2127 (Sept. 2021).
157. Thomas, C. A., Springer, P. A., Loeb, G. E., Berwald-Netter, Y. & Okun, L. M. A miniature microelectrode array to monitor the bioelectric activity of cultured cells. *Experimental cell research* **74**, 61–66 (1972).
158. McConnell, E. R., McClain, M. A., Ross, J., LeFew, W. R. & Shafer, T. J. Evaluation of multi-well microelectrode arrays for neurotoxicity screening using a chemical training set. *Neurotoxicology* **33**, 1048–1057 (Oct. 2012).
159. Aguet, F. *et al.* The GTEx Consortium atlas of genetic regulatory effects across human tissues. *Science* **369**, 1318–1330 (Sept. 2020).
160. Rogawski, M. A. & Löscher, W. The neurobiology of antiepileptic drugs. *Nature Reviews Neuroscience* *2004* 5:7 **5**, 553–564 (2004).
161. Pedrosa, E. *et al.* Development of patient-specific neurons in schizophrenia using induced pluripotent stem cells. *Journal of neurogenetics* **25**, 88–103 (Oct. 2011).
162. Shahsavani, M. *et al.* An in vitro model of lissencephaly: expanding the role of DCX during neurogenesis. *Molecular psychiatry* **23**, 1674–1684 (July 2018).
163. Ohtsuka, T. & Kageyama, R. Hes1 overexpression leads to expansion of embryonic neural stem cell pool and stem cell reservoir in the postnatal brain. *Development (Cambridge)* **148** (Feb. 2021).
164. Caldwell, A. B. *et al.* Dedifferentiation and neuronal repression define familial Alzheimer’s disease. *Science Advances* **6**, 5933–5946 (Nov. 2020).
165. Mertens, J. *et al.* Age-dependent instability of mature neuronal fate in induced neurons from Alzheimer’s patients. *Cell Stem Cell* **28**, 1533 (Sept. 2021).
166. Whitehouse, C. M. & Lewis, M. H. Repetitive Behavior in Neurodevelopmental Disorders: Clinical and Translational Findings. *The Behavior Analyst* **38**, 163 (Oct. 2015).

167. Liu, H. *et al.* Dissection of the relationship between anxiety and stereotyped self-grooming using the Shank3B mutant autistic model, acute stress model and chronic pain model. *Neurobiology of Stress* **15**, 100417 (Nov. 2021).
168. De Brouwer, G., Fick, A., Harvey, B. H. & Wolmarans, D. W. A critical inquiry into marble-burying as a preclinical screening paradigm of relevance for anxiety and obsessive-compulsive disorder: Mapping the way forward. *Cognitive, Affective, & Behavioral Neuroscience* 2018 19:1 **19**, 1–39 (Oct. 2018).
169. Kim, Y. S. *et al.* Prevalence of autism spectrum disorders in a total population sample. *The American journal of psychiatry* **168**, 904–912 (Sept. 2011).
170. Schwartz, J. J. *et al.* Maternal immune activation and strain specific interactions in the development of autism-like behaviors in mice. *Translational psychiatry* **3** (2013).
171. Angelakos, C. C. *et al.* Hyperactivity and male-specific sleep deficits in the 16p11.2 deletion mouse model of autism. *Autism research : official journal of the International Society for Autism Research* **10**, 572–584 (Apr. 2017).
172. Jung, H. *et al.* Sexually dimorphic behavior, neuronal activity, and gene expression in Chd8-mutant mice. *Nature neuroscience* **21**, 1218–1228 (Sept. 2018).
173. Kim, K. C. *et al.* Sex Differences in Autism-Like Behavioral Phenotypes and Postsynaptic Receptors Expression in the Prefrontal Cortex of TERT Transgenic Mice. *Biomolecules & Therapeutics* **25**, 374 (2017).
174. Napolitano, A. *et al.* Sex Differences in Autism Spectrum Disorder: Diagnostic, Neurobiological, and Behavioral Features. *Frontiers in Psychiatry* **13**, 969 (May 2022).
175. Baron-Cohen, S. The extreme male brain theory of autism. *Trends in Cognitive Sciences* **6**, 248–254 (June 2002).
176. Werling, D. M. The role of sex-differential biology in risk for autism spectrum disorder. *Biology of sex differences* **7** (Nov. 2016).
177. Bargiela, S., Steward, R. & Mandy, W. The Experiences of Late-diagnosed Women with Autism Spectrum Conditions: An Investigation of the Female Autism Phenotype. *Journal of Autism and Developmental Disorders* **46**, 3281–3294 (Oct. 2016).

178. Chen, J., Fuhler, N., Noguchi, K. & Dougherty, J. D. MYT1L is required for suppressing earlier neuronal development programs in the adult mouse brain. *bioRxiv*, 2022.10.17.512591 (Oct. 2022).
179. Moore, S. M. *et al.* Setd5 haploinsufficiency alters neuronal network connectivity and leads to autistic-like behaviors in mice. *Translational Psychiatry* 2019 9:1 **9**, 1–12 (Jan. 2019).
180. Flaherty, E. *et al.* Patient-derived hiPSC neurons with heterozygous CNTNAP2 deletions display altered neuronal gene expression and network activity. *npj Schizophrenia* 2017 3:1 **3**, 1–4 (Oct. 2017).
181. Nageshappa, S. *et al.* Altered neuronal network and rescue in a human MECP2 duplication model. *Molecular Psychiatry* 2016 21:2 **21**, 178–188 (Sept. 2015).
182. Alsaqati, M., Heine, V. M. & Harwood, A. J. Pharmacological intervention to restore connectivity deficits of neuronal networks derived from ASD patient iPSC with a TSC2 mutation. *Molecular Autism* **11**, 1–13 (Dec. 2020).
183. Liu, X. S. *et al.* Rescue of Fragile X syndrome neurons by DNA methylation editing of the FMR1 gene. *Cell* **172**, 979 (Feb. 2018).
184. Ghatak, S. *et al.* NitroSynapsin ameliorates hypersynchronous neural network activity in Alzheimer hiPSC models. *Molecular psychiatry* **26**, 5751–5765 (Oct. 2021).
185. Rubenstein, J. L. & Merzenich, M. M. Model of autism: increased ratio of excitation/inhibition in key neural systems. *Genes, brain, and behavior* **2**, 255–267 (Oct. 2003).
186. Dotti, C. G., Sullivan, C. A. & Banker, G. A. The Establishment of Polarity by Hippocampal Neurons in Culture. *The Journal of Neuroscience* **8**, 1454–488 (1988).
187. Veerman, C. C., Wilde, A. A. & Lodder, E. M. The cardiac sodium channel gene SCN5A and its gene product NaV1.5: Role in physiology and pathophysiology. *Gene* **573**, 177–187 (Dec. 2015).
188. Gellens, M. E. *et al.* Primary structure and functional expression of the human cardiac tetrodotoxin-insensitive voltage-dependent sodium channel. *Proceedings of the National Academy of Sciences of the United States of America* **89**, 554–558 (1992).

189. Benito, B. *et al.* A mutation in the sodium channel is responsible for the association of long QT syndrome and familial atrial fibrillation. *Heart rhythm* **5**, 1434–1440 (Oct. 2008).
190. Zeng, Z. *et al.* Electrophysiological characteristics of a SCN5A voltage sensors mutation R1629Q associated with Brugada syndrome. *PloS one* **8** (Oct. 2013).
191. Wang, J. *et al.* Multiple Nav1.5 isoforms are functionally expressed in the brain and present distinct expression patterns compared with cardiac Nav1.5. *Molecular Medicine Reports* **16**, 719–729 (July 2017).
192. Frenz, C. T. *et al.* Nav1.5 sodium channel window currents contribute to spontaneous firing in olfactory sensory neurons. *Journal of Neurophysiology* **112**, 1091 (Sept. 2014).
193. Hartmann, H. A., Colom, L. V., Sutherland, M. L. & Noebels, J. L. Selective localization of cardiac SCN5A sodium channels in limbic regions of rat brain. *Nature neuroscience* **2**, 593–595 (July 1999).
194. Donahue, L. M. *et al.* The cardiac sodium channel mRNA is expressed in the developing and adult rat and human brain. *Brain research* **887**, 335–343 (Dec. 2000).
195. Chioni, A. M. *et al.* A novel polyclonal antibody specific for the Na(v)1.5 voltage-gated Na(+) channel 'neonatal' splice form. *Journal of neuroscience methods* **147**, 88–98 (Sept. 2005).
196. Wang, J. *et al.* New variants of Nav1.5/SCN5A encode Na⁺ channels in the brain. *Journal of neurogenetics* **22**, 57–75 (2008).
197. Wu, L., Nishiyama, K., Hollyfield, J. G. & Wang, Q. Localization of Nav1.5 sodium channel protein in the mouse brain. *Neuroreport* **13**, 2547–2551 (Dec. 2002).
198. Ren, C. T. *et al.* Cloning and expression of the two new variants of Nav1.5/SCN5A in rat brain. *Molecular and cellular biochemistry* **365**, 139–148 (June 2012).
199. Malik, S., Arif, H. & Hirsch, L. J. Lamotrigine and its applications in the treatment of epilepsy and other neurological and psychiatric disorders. *Expert review of neurotherapeutics* **6**, 1609–1627 (Nov. 2006).

200. Mossink, B., Negwer, M., Schubert, D. & Nadif Kasri, N. The emerging role of chromatin remodelers in neurodevelopmental disorders: a developmental perspective. *Cellular and Molecular Life Sciences* **78**, 2517–2563 (Mar. 2021).
201. Chen, S., Lee, B., Lee, A. Y. F., Modzelewski, A. J. & He, L. Highly efficient mouse genome editing by CRISPR ribonucleoprotein electroporation of zygotes. *Journal of Biological Chemistry* **291**, 14457–14467 (July 2016).
202. Dull, T. *et al.* A Third-Generation Lentivirus Vector with a Conditional Packaging System. *Journal of Virology* **72**, 8463–8471 (Nov. 1998).
203. Gompers, A. L. *et al.* Germline Chd8 haploinsufficiency alters brain development in mouse. *Nature Neuroscience* **20**, 1062–1073 (Aug. 2017).
204. Levin, J. Z. *et al.* Comprehensive comparative analysis of strand-specific RNA sequencing methods. *Nature Methods* **7**, 709–715 (Sept. 2010).
205. Dobin, A. *et al.* STAR: Ultrafast universal RNA-seq aligner. *Bioinformatics* **29**, 15–21 (Jan. 2013).
206. Love, M. I., Huber, W. & Anders, S. Moderated estimation of fold change and dispersion for RNA-seq data with DESeq2. *Genome Biology* **15**, 550 (Dec. 2014).
207. Strimmer, K. A unified approach to false discovery rate estimation. *BMC Bioinformatics* **9**, 1–14 (July 2008).
208. Franzén, O., Gan, L. M. & Björkegren, J. L. PanglaoDB: A web server for exploration of mouse and human single-cell RNA sequencing data. *Database* **2019**, 46 (Jan. 2019).
209. Schaum, N. *et al.* Single-cell transcriptomics of 20 mouse organs creates a Tabula Muris. *Nature* **562**, 367–372 (Oct. 2018).
210. Schiebinger, G. *et al.* Optimal-Transport Analysis of Single-Cell Gene Expression Identifies Developmental Trajectories in Reprogramming. *Cell* **176**, 928–943 (Feb. 2019).
211. Trapnell, C. *et al.* Transcript assembly and quantification by RNA-Seq reveals unannotated transcripts and isoform switching during cell differentiation. *Nature Biotechnology* **28**, 511–515 (May 2010).

212. Subramanian, A. *et al.* Gene set enrichment analysis: A knowledge-based approach for interpreting genome-wide expression profiles. *Proceedings of the National Academy of Sciences of the United States of America* **102**, 15545–15550 (Oct. 2005).
213. Krämer, A., Green, J., Pollard, J. & Tugendreich, S. Causal analysis approaches in ingenuity pathway analysis. *Bioinformatics* **30**, 523–530 (Feb. 2014).
214. Raudvere, U. *et al.* G:Profiler: A web server for functional enrichment analysis and conversions of gene lists (2019 update). *Nucleic Acids Research* **47**, W191–W198 (July 2019).
215. Shen, L. *GeneOverlap: An R package to test and visualize gene overlaps* tech. rep. (2016).
216. Kuleshov, M. V. *et al.* Enrichr: a comprehensive gene set enrichment analysis web server 2016 update. *Nucleic Acids Research* **44**, W90–W97 (July 2016).
217. Chen, E. Y. *et al.* Enrichr: Interactive and collaborative HTML5 gene list enrichment analysis tool. *BMC Bioinformatics* **14**, 1–14 (Apr. 2013).
218. Mimitou, E. P. *et al.* Multiplexed detection of proteins, transcriptomes, clonotypes and CRISPR perturbations in single cells. *Nature Methods* **16**, 409–412 (May 2019).
219. Gehring, J., Hwee Park, J., Chen, S., Thomson, M. & Pachter, L. Highly multiplexed single-cell RNA-seq by DNA oligonucleotide tagging of cellular proteins. *Nature Biotechnology* **38**, 35–38 (Jan. 2020).
220. Zheng, G. X. *et al.* Massively parallel digital transcriptional profiling of single cells. *Nature Communications* **8**, 1–12 (Jan. 2017).
221. Hao, Y. *et al.* Integrated analysis of multimodal single-cell data. *bioRxiv*, 2020.10.12.335331 (Oct. 2020).
222. Wolf, F. A., Angerer, P. & Theis, F. J. SCANPY: Large-scale single-cell gene expression data analysis. *Genome Biology* **19**, 15 (Feb. 2018).
223. Lotfollahi, M. *et al.* Query to reference single-cell integration with transfer learning. *bioRxiv*, 2020.07.16.205997 (July 2020).
224. Xu, C. *et al.* Probabilistic harmonization and annotation of single[U+2010]cell transcriptomics data with deep generative models. *Molecular Systems Biology* **17** (Jan. 2021).

-
225. Finak, G. *et al.* MAST: A flexible statistical framework for assessing transcriptional changes and characterizing heterogeneity in single-cell RNA sequencing data. *Genome Biology* **16**, 1–13 (Dec. 2015).
226. Gelfman, S. *et al.* meaRtools: An R package for the analysis of neuronal networks recorded on microelectrode arrays. *PLoS Computational Biology* **14**, e1006506 (Oct. 2018).

SUPPLEMENTARY FIGURES

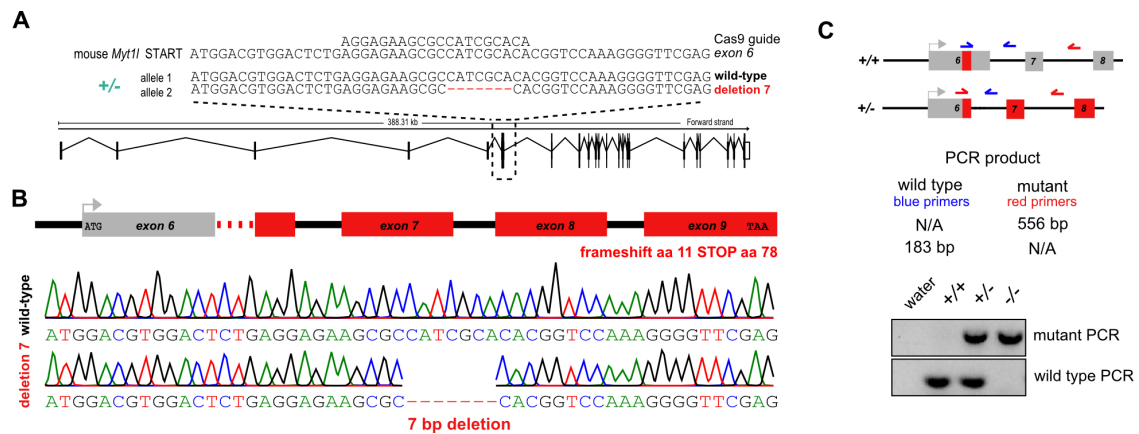


Figure S1: Generation of *Myt1l*-mutant mice. (A) Exon structure of mouse *Myt1l* on Chromosome 12: 29,578,383-29,973,212 (ENSMUSG0000061911). Exon 6 containing the ATG START codon is highlighted and the DNA sequence is displayed together with the CRISPR/Cas9 guide RNA sequence used to induce mutagenesis. (B) Schematic of CRISPR/Cas9-induced 7 bp deletion (dotted red line) in exon 6 inducing a frameshift (red) at amino acid (aa) 11 and terminating in a premature STOP codon at aa 78 in exon 9 (p.R11GfsX68). Mutant mice were identified by Sanger sequencing, which confirmed a 7-bp deletion in exon 6 of mouse *Myt1l*. (C) PCR with primer pairs P1 (wild type, blue) and P2 (mutant, red) were used to genotype *Myt1l*^{+/+}, *Myt1l*^{+/-}, and *Myt1l*^{-/-} mice.

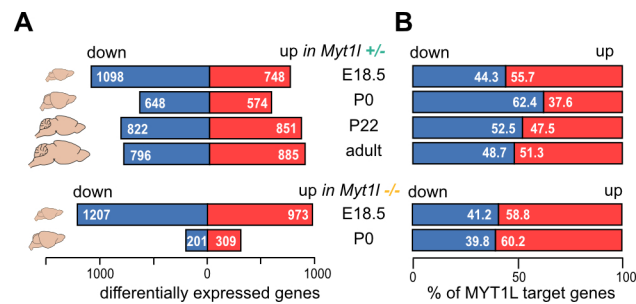


Figure S2: Bulk gene expression changes in *Myt1l*-mutant mice. **(A)** Number of deregulated genes upon *Myt1l* mutation across development. Shown are genes that were down- (blue) or upregulated (red) upon MYT1L deficiency with absolute log₂ fold change > 1E-05 and p-adj < 0.1. **(B)** Percentage of up- and downregulated genes shown in panel A, which are MYT1L target genes (± 5 kb from transcription start site) based on CUT&RUN experiments for the corresponding time points, except all targets pooled for P22. $n \geq 5$ E18.5, $n \geq 4$ P0 for *Myt1l*^{+/+}, *Myt1l*^{+/-} and *Myt1l*^{-/-} respectively; $n = 6$ P22, $n \geq 3$ adult for *Myt1l*^{+/+} and *Myt1l*^{+/-} respectively.

Figure S3 (*Figure on next page*): Engineered human embryonic stem cells with a heterozygous conditional knockout allele of MYT1L. **(A)** Exon structure of human *MYT1L* on chromosome 2: 1,789,113-2,331,664 (ENSG00000186487). Exon 6 containing the ATG START codon is highlighted and the DNA sequence is displayed together with the CRISPR/Cas9 guide RNA sequence used to induce mutagenesis. **(B)** Schematic of targeting construct used for homologous recombination in male H1 ES cells with neomycin (neo) selection cassette, cre (loxP) and flp (FRT) recombinase-specific recognition sequences, respectively. Flp-induced recombination removed neomycin selection cassette and cre-mediated recombination deleted exon 7, resulting in a frameshift (red) starting in exon 8 at amino acid (aa) 19 and terminating in a premature STOP codon at aa 69 in exon 9 (p.V19AfsX51). **(C)** Genotyping PCR with primer pairs P1 (left arm) and P2 (right arm) were used to identify successfully targeted clones. Clone C and H, subsequently referred to as clone 1 and clone 2, resulted from two independent targeting experiments and were used for this study. **(D)** Genotyping PCR with primer pairs P3 (loxP/wt), P4 (flp/wt), and P5 (neo) were used to verify successful heterozygous targeting and neomycin cassette removal upon flp-mediated recombination in clone 1 and clone 2. **(E)** Heterozygous targeting was confirmed by Sanger sequencing that showed insertion of loxP sites within one allele and insertion of silent G > A mutation (red box) to remove the PAM site (yellow box) in both alleles of human MYT1L clone 1 and clone 2.

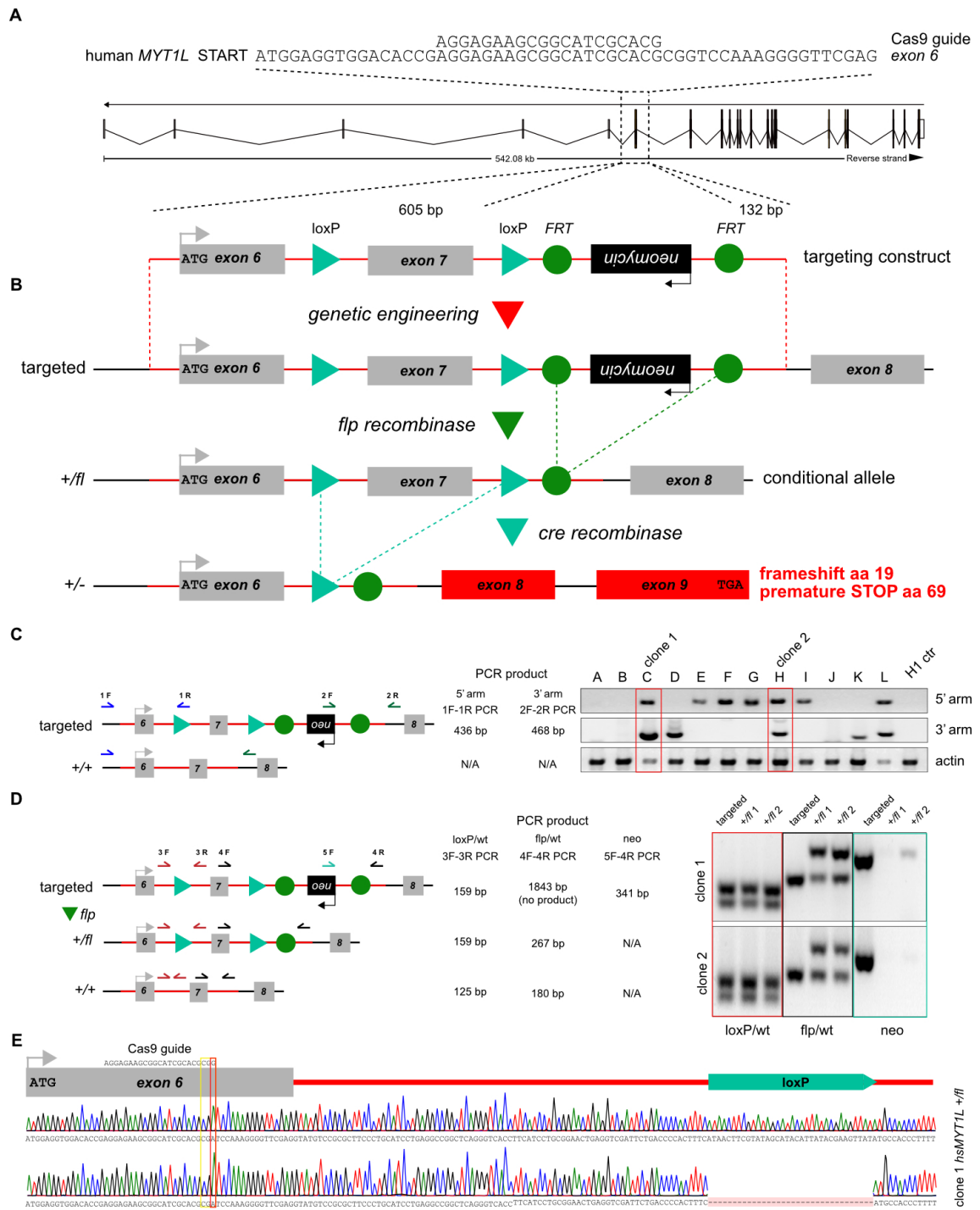


Figure S3: Engineered human embryonic stem cells with a heterozygous conditional knock-out allele of *MYT1L* (Legend on previous page)

LIST OF FIGURES

1.1	Waddington's epigenetic landscape	2
1.2	Schematic figure of the primary and secondary brain vesicles	3
1.3	Schematic presentation of the steps of cortical neurogenesis in the mouse	4
1.4	Schematic representation of key signalling pathways involved in neurogenesis	6
1.5	Expression of the transcription factor MYT1L	9
2.1	Full-length MYT1L protein is crucial for survival	13
2.2	N-terminally-truncated MYT1L protein in <i>Myt1l</i> -mutant mice	14
2.3	MYT1L depletion impairs neurogenesis in mice	16
2.4	<i>Myt1l</i> -deficient mice have thinner cortices	17
2.5	<i>Myt1l</i> -deficient mice show gene deregulation associated with neurodevelopmental disorders	18
2.6	Upregulation of non-neuronal signatures in <i>Myt1l</i> -deficient mice	19
2.7	No new cell clusters in <i>Myt1l</i> -depleted mouse prefrontal cortex	20
2.8	Expression changes of MYT1L target genes	22
2.9	MYT1L depletion results in behavioural phenotypes in mice	24
2.10	Male-specific social deficits in <i>Myt1l</i> -deficient mice	25
2.11	Engineered human embryonic stem cells can be used to model <i>MYT1L</i> deficiency in a human system	26
2.12	Predominant up-regulation of genes in <i>MYT1L</i> -deficient human induced neurons	27
2.13	Upregulation of non-neuronal signatures upon MYT1L depletion in human induced neurons	28
2.14	Gene upregulation and delayed neurogenesis in MYT1L-depleted human induced neurons	29
2.15	Partial rescue of transcriptional changes caused upon MYT1L depletion in human induced neurons by chemical inhibition of the WNT and NOTCH signalling pathway	30

2.16	Electrophysiological network hyperactivity of MYT1L-deficient human induced neurons	32
2.17	Electrophysiological network hyperactivity of MYT1L-depleted mouse primary cultures	34
2.18	The N-terminally-truncated MYT1L protein does not have a dominant negative functional effect	35
2.19	Increased synaptic activity of MYT1L-depleted primary hippocampal cultures . . .	36
2.20	Increased synaptic activity in brain slices from <i>Myt1l</i> -deficient mice	37
2.21	Post-mitotic MYT1L overexpression in <i>Myt1l</i> -depleted primary mouse cultures rescues electrophysiological hyperactivity	39
2.22	Up-regulated non-neuronal MYT1L target genes in human and mouse cultures include the main cardiac sodium channel SCN5A	40
2.23	<i>SCN5A</i> knockdown rescues the hyperactivity phenotype in MYT1L-deficient mouse and human cultures	41
2.24	Application of the sodium channel blocker lamotrigine normalises electrophysiological activity of mouse and human neurons <i>in vitro</i> as well as mouse behaviour phenotypes <i>in vivo</i>	43
4.1	Graphical abstract	54
S1	Generation of <i>Myt1l</i> -mutant mice	106
S2	Bulk gene expression changes in <i>Myt1l</i> -mutant mice	107
S3	Engineered human embryonic stem cells with a heterozygous conditional knockout allele of <i>MYT1L</i>	108

DECLARATION

I hereby declare that I have prepared the dissertation “The role of MYT1L in the aetiology of neurodevelopmental disorders” myself and in this process have not use any other sources than those expressly indicated.

I have not applied to be examined at any other institution, nor have I used the dissertation in this or any other form at any other institution as an examination paper, nor submitted it to any other faculty as a dissertation.

Heidelberg, 20.01.2023

Bettina Weigel

CONTRIBUTIONS

The work presented in this thesis would not have been possible without the contribution from several people:

Dr. Moritz Mall and **Jana F. Tegethoff** were instrumental for planning, implementing and compiling this project.

Dr. Moritz Mall created the *Myt1l*-mutant mouse line and, together with **Sarah D. Grieder** engineered the conditional *MYT1L*-mutant embryonic stem cells, which have been used in this study.

Induced neurons were generated by **Sarah D. Grieder** and **Jana F. Tegethoff**. Both also provided help with some primary cultures.

I had huge support with all bioinformatic analyses from **Bryce Lim**, **Manu Saraswat**, **Dr. Christian Arnold**, **Dr. Ignacio L. Ibarra**, **Dr. Juan M. Adrian-Segarra**, **Eric Poisel**, **Berit Brinkmann** and **Dr. Judith Zaugg**.

Patch clamp recordings were performed by **Dr. Claudio Acuna**, **Joaquin Campos** and **Dr. Yu-Chao Liu**.

I was supported with the behaviour experiments by **Jana F. Tegethoff**, **Janina Kaspar** and **Dr. Bhuvaneswari Nagarajan**.

Dr. Juan M. Adrian-Segarra established the scRNA-Seq protocol and he and **Bryce Lim** supported the experiments.

The mass spectrometry analysis was performed by **Dr. Jeroen Krijgsveld** and **Dr. Dimitris Papageorgiou**.

I had great help with the harvest, slicing, staining and quantification of brain sections from **Laura K. Schmidt**, **Janina Kaspar** and **Jana F. Tegethoff**

ACKNOWLEDGEMENTS

I have been waiting for a long time for this moment to write the last words of my PhD thesis and thank everyone who has supported me throughout my journey.

First of all, I want to acknowledge all the mice that have contributed to this study. Their death helped us to advance scientific knowledge and I hold them in high regard.

I am very grateful to Moritz Mall who gave me the opportunity to perform my PhD thesis in his lab. Thank you for believing in me (often more than I did myself) and for all the professional and personal support that has helped to shape me as a scientist and person.

It is hard for me to put into words how much I would like to thank all present and past members of the Mall lab: Elisa, Jana, Bryce, Manu, Taishi, Jule, Laura, Laura K., Sarah, Tim, Maria-Luisa, Elias, Manja, Katharina, Mona, Heather, Marleen, Janina, Juan, Eric, Bhuvi, Felix, Lea and Katalin. You guys are awesome and I could not have hoped for better colleagues. Thank you - especially our PhD crew - very much for your outstanding support inside and outside the lab, all the good memories, the funny PhD meetings and for listening to all my complaints.

I was very lucky to have great help with the preparation of my manuscript. Names of all contributors are mentioned in the Contribution chapter but I wanted to thank everybody here again for your great support in getting the story published. I also want to thank the members of the DKFZ Genomics and Proteomics Core Facility, the scOpenLab, and the Light Microscopy facility for all the help. A special thanks goes to the animal caretakers of the Center for Preclinical Research and the Interdisciplinary Neurobehavioural Core of Heidelberg University. Your support was outstanding.

I would like to thank my examiners and members of my Thesis Advisory Committee: Ana Martin-Villalba, Michael Milsom, Judith Zaugg, Christian Schaaf and Moritz Mall. I highly appreciate all your valuable input and that you took the time to review my thesis.

Vielen Dank an Peter Winterstein, dass Sie meine wöchentliche Konstante waren.

Ein großes Dankeschön geht an alle meine Freunde, die mich seit Jahrzehnten (Ich bin über 30, da kann ich so etwas sagen) auf meinem Lebensweg unterstützen, mich zum Lachen bringen, mit mir weinen, gute Gespräche führen und einfach tolle Freunde sind!

Namentlich erwähnen möchte ich meine beiden ältesten Freunde Lisa und Alena. Auch wenn wir uns aufgrund der Entfernung nicht immer regelmäßig sehen weiß ich, dass ich mich immer an euch wenden kann und es sich dann einfach so anfühlt als würden wir wieder gemeinsam zur Schule laufen oder in der Uni sitzen und es wäre keine Zeit vergangen.

Vielen Dank an Laura K., dass ich bei dir immer das Wort Pineapple benutzen darf. Ich hoffe du weißt, dass du mich gerettet hast.

Danke an Peter und Jana für eure grenzenlose Unterstützung und Gastfreundschaft und danke Peter, dass du mir immer den Dezember versüßt hast.

Für meine zwei besten Freunde hier in Heidelberg, Beri und Markus, bin ich unglaublich dankbar. Ich will mir gar nicht vorstellen wie mein Leben hier ausgesehen hätte, wenn ich nicht bei dem PhD Interview mit Beri in ein Zimmer gesteckt worden wäre oder Markus bei der Happy Hour getroffen hätte. Ihr seid wirklich großartig und ich hoffe, dass sich nie etwas an unserer Freundschaft ändert.

Das größte Dankeschön möchte ich an meine Familie richten. Vielen Dank, besonders an Mama, Papa, Johannes und Alexander für eure unglaubliche Unterstützung in allen möglichen Bereichen. Eine Familie zu haben, auf die man sich immer verlassen kann und zu der man gerne nach Hause kommt, ist das Wichtigste auf der Welt! Vielen Dank auch an meinen Ruhepol Mischa. Dich in meinem Leben zu haben hat es definitiv besser gemacht und ich freue mich mit dir gemeinsam das nächste Kapitel zu starten.

I had an urge to put a smiley behind every sentence but since that would have been a smiley overload, here is one for all of you and it comes from the heart:

